Development of a distributed sediment routing model for extreme rainfall-runoff events

Luis Enrique CHERO VALENCIA

2021

KYOTO UNIVERSITY

Development of a distributed sediment routing model for extreme rainfall-runoff events

極端な降雨流出事象を対象とする分布型土砂追跡モデルの開発

by

Luis Enrique CHERO VALENCIA

A dissertation in partial fulfillment of the requirement for the degree of Doctor of Philosophy

in the

Department of Civil and Earth Resources Engineering,

Graduate School of Engineering, Kyoto University

Declaration of Authorship

I, Luis Chero, declare that this thesis and the work presented throughout are my own and have been generated by myself as the result of my own original research with the exception of any work of others which has all been appropriate referenced. It has not been submitted, either in part or whole, for a degree at this or any other university.

Luis Enrique CHERO VALENCIA

Abstract

Predictions of the rainfall-runoff and sediment transport are crucial in land development under climate change. Data on topography, rainfall patterns, land use, and river management policies are continuously updated to include information on sediment disasters; however, the interaction among these factors is not fully understood. Predictions of the rainfall-runoff and sediment in ungauged basins are reportedly limited, with significant gaps in the collected information; additionally, in certain cases, it is assumed that a selected hydrological model can be used to achieve satisfactory results by forcing specific parameters and theoretical assumptions.

For the reasons presented above, this thesis focuses on the interaction between extreme rainfall and the steep topography of basins when simulating runoff and sediment routing conditions. Events such as the El Nino Southern Oscillation (ENSO) on the Peruvian North Pacific coast and the East Asian Monsoon in Kyushu, Japan reportedly lead to the occurrence of substantial rainfall. In Chapters 2 and 3, the use of kinematic wave equations for the development of a sequential algorithm, followed by consequent extension of the routing model to include data on the processing and transfer of eroded material as suspended sediment flow (Q_S), is explained, with the routing process beginning on the slope section of the basin continuing as Q_S in accordance with the sediment continuity relationships and the digital drainage direction (DIR).

The model was developed and validated by considering an extreme event that occurred in Japan during the Monsoon season in July 2018. The rainfall distribution information was obtained using XRAIN, and high-resolution (10 m and 100 m) DEM were provided from MLIT. The simulations of the Akatani River in Japan were satisfactory in terms of hydrological features, with the obtainment of a peak discharge of 520 $m^3 s^{-1}$ that was close to the MLIT estimations; moreover, the results for sediment transport balance were also proven accurate, with 60 000 m^3 of sediments deposited in the lower Akatani basin and an estimated 680 000 m^3 of sediment eroded and flushed into the Chikugo river. Furthermore, the application of information on sediment deposition relationships to plot the river profile after aggradation/erosion over the lower river section that led to the outlet was possible. The results have been discussed and comparison has been presented against reports published by the Kyushu Regional Development Bureau in Chapter 4 regarding the volume of sediment and discharge analysis after occurrence of the extreme event.

The next objective of this study entailed application of the model to study the transport of sediment and the occurrence of erosion on the Peruvian Coast in Chapter 5. The Tumbes River basin was selected as it is generally affected by recurrent extreme rainfall events as a result of the ENSO. The acceleration of high concentrations of sediment and the occurrence of flooding downstream leads to disruption in the surface transport and in the incurment of economic losses. Another factor that aided the selection of Tumbes River was the availability of updated field data collected by the Peruvian Meteorological Institute (SENAMHI) and the Peruvian Geophysical Institute (IGP). The GSMAP rainfall information was bias-corrected and distributed according to the gauged data collected over recent years, while isohyets were used to describe historical events in 1983 and 1998 and to apply data on spatial distribution. Parameter sensitivity was determined to reduce the uncertainty associated with the assignment of sediment parameters. To establish the optimum spatial resolution, resolutions of 1 km and 500 m were considered as input and the threshold values for sediment parameters were determined along with the formulation of a decision on the factors that were deemed critical for application to larger scale basins.

The application of the simulation to Tumbes River helped establish and test a hypothesis formulated on the mechanisms by which ENSO affected the rainfall-runoff process and accelerated the transport of sediments. The sediment concentration and sediment transport in multiple representative years under ENSO and non-ENSO conditions have been compared and presented in Chapter 6; we inferred that it was possible to characterize and determine the intensity of past and establish future extreme events according to the spatial distribution and persistence of rainfall via generation of rating curves. A second analysis was performed to obtain insights into the relationship between the daily average sediment transport and daily average discharge (which has been widely discussed in scientific journals). The plot depicted in Chapter 6 shows hysteresis behavior that changes from a clockwise orientation to other orientations according to the intensity of ENSO events.

The two assessment methods for Peru (hysteresis loops and sediment rating curves) are in agreement with previously reported methods and estimations performed using data historical data in Tumbes River and neighbor coastal basins. In Chapter 7, this model was used to estimate the change in the bed profile of the area surrounding the outlet, the result of which was an acceptable bed aggradation of approximately 3 m in the most critical period of the rainy season. It was also possible to identify the sub basins that were likely to produce higher concentrations of the sediment, information on which could be used to assess river protection approaches and sediment traps in the foreseeable future.

In terms of conclusions and improvements, emphasis was placed on the necessity of determining the basin response cycle and alert system to avoid material and human losses through the detection of critical erosional areas in which sediment deposition was likely to occur. The sediment routing results indicate the establishment of a satisfactory simulation tool for identification of areas that should be evacuated or should be subjected to infrastructure upgradation before the occurrence of extreme events. Hence, integrated flood management also requires the use of appropriate gauging tools, laboratory software and hardware, and approaches that can be used to include information on the effects of climate change.

Doctor of Philosophy

by Luis Enrique CHERO VALENCIA

Keywords:

Sediment transport model; distributed model; high-resolution topography; hillslope erosion, ENSO assessment

Acknowledgements

This thesis work is the result of research completed in the Hydrology and Water Resources Research Laboratory at Kyoto University. First of all, I would like to acknowledge the harmony in the workplace and support from all the staff throughout these years.

I would like to express my sincere gratitude to Professor Dr. Yasuto Tachikawa for his continuous dedication and support to discuss and share knowledge about the modeling aspects through his vast expertise. Also, for his continuous advice about dealing with academic and everyday life in Japan.

Thanks to Dr. Tomohiro Tanaka for the support in the development stages of the C++ coding process as well as modeling the hydrological process and how to include mathematical relationships, for the interesting seminar academic discussions and sharing good moments in the meetings.

Thanks to Dr. Yutaka Ichikawa for the important discussion about the hydrological process during the academic seminars, consultations at the office and advice before conference and classes.

Thanks to Dr. Sunmin Kim for his role as supervisor and guidance throughout the discussion sessions and the great opportunities to comment about this research and other academic subjects.

Thanks to Dr. Kazuaki Yorozu for his kind support in academic matters, laboratory duties and suggestions to improve my research.

I would like to thank the Peruvian Geophysical Institute (IGP), Binational Project Tumbes Puyango (PBNTP) and Peruvian Service of Hydrology and Meteorology (SENAMHI) for kindly accepting my queries in their office and for the provided information and access to literature in their digital library.

I would like to thank and M.Sc. Lidio Matos from SENAMHI for solving many queries about the behavior of the Tumbes River and sedimentation studies in Peru.

Special recognition goes to the Ministry of Education, Culture, Sport, Science and Technology (MEXT, Japan), for the financial support given to me under "Monbukagakusho" scholarship throughout my research at Kyoto University.

A special thanks to my family Ines, Emilio, my father Emilio and my fiancée Ana for their emotional support during my stay in Kyoto.

This work is dedicated to the memory of my mother, Ana Valencia.

Luis Enrique CHERO VALENCIA

Kyoto, Japan, 2021

Table of contents

Declaration of Authorship i

Abstract iii

Acknowledgements vii

List of Figures xiii

List of Tables xix

Abbreviations xxi

Chapter 1. Introduction 1

1.1 Background 1

1.1.1 Rainfall-runoff models and the relationship with sediment transport 1

1.1.2 Rainfall-runoff models in Japan and Peru 2

1.1.3 ENSO and the generation of sediment 3

1.1.4 The context of an integrated sediment model for river management 5

1.1.5 Rating curves (adjustment after events, forecast, improvements) 5

1.2 Objectives 5

1.3 Outline of the thesis 6

Chapter 2. Construction of a rainfall-runoff model for sediment routing 9

2.1 Introduction 9

2.2 Distributed model 1K-DHM 9

2.3 Generation of spatial distributed rainfall 12

2.4 Estimation of evapotranspiration at the Tumbes River basin 12

2.5 Topographical features and basin processing 12

2.6 Calibration of the 1K-DHM 15

Chapter 3. Development of a sediment routing model coupled with a distributed rainfall-runoff model 17

3.1 Introduction 17

3.2 Methodology: sediment process-based component 18
3.3 Sediment erosion-deposition model 19
3.4 Sediment transport governing equation 20
3.5 Governing differential equations for erosion and deposition 21
3.5.1 Sediment generation as a result of flow detachment (DF) 22
3.5.2 Sediment generation as a result of raindrop impact (DR) 23
3.5.3 River bed profile evolution 26
3.6 Solution algorithm 26
3.7 Chapter conclusion 28
Chapter 4. Application of the sediment routing model to a mountainous basin in Japan and analysis of sediment transport and topographic change 29
4.1 Introduction 29
4.2 Akatani River input data 29
4.3 Calibration for the Akatani River simulations 32
4.4 Application of the sediment routing model to the Akatani River basin 33
4.5 Sediment transport results 34
4.6 Chapter conclusion 37
Chapter 5. Application of the sediment routing model to a mountainous basin in Peru and analysis of the interaction between rainfall-runoff and sediment transport 41
5.1 Introduction 41
5.2 Application of sediment routing model in Tumbes River basin in Peru 42
5.3 Description of the model for application in Tumbes River 43
5.3.1 Distributed rainfall and topography data 43
5.3.2 Sediment generation modeling for Tumbes River 44
5.4 Rainfall-runoff and sediment simulation results 46
5.4.1 Rainfall-runoff simulation results 46
5.4.2 Sediment simulation results 48

5.5 Sensitivity analysis of model resolution using an integrated model 50

5.6 Chapter conclusion 53

Chapter 6. Generation of sediment rating curves for a mountainous basin in Peru and consideration of the effect exerted by ENSO on the characteristics of the rating curves 55

6.1 Introduction 55

6.2 ENSO effects exerted on the Tumbes River basin 56

6.3 Data sources and quality analysis 58

6.4 Rainfall-runoff and sediment simulation results 59

6.4.1 Identification of the hydrological and sediment model parameters 59

6.4.2 Sediment model validation 60

6.5 The effect of ENSO on sediment generation 64

6.5.1 The effect of the ENSO on sediment rating curve 64

6.5.2 ENSO effects exerted on seasonal sediment transport 70

6.6 Chapter conclusions 72

Chapter 7. Discussion on ENSO effects exerted on the sediment dynamics of the Tumbes River basin in Peru 75

7.1 Introduction 75

7.2 Analysis method of determining ENSO effects exerted on sediment routing ... 75

7.3 Description of ENSO-specific conditions in the Peruvian Coast 76

7.3.1 Normal conditions 76

7.3.2 El Nino Conditions 76

7.3.3 Generation of rainfall data for past El Nino conditions 80

7.3.4 Sediment concentration maps according to ENSO events 82

7.3.5 Sediment accumulation in the channel sections of the Tumbes River 85

7.4 Chapter conclusion 87

Chapter 8. Concluding remarks and future directions in the field 89

8.1 Concluding remarks 89

8.2 Future lines of research 92

Bibliography 93

A) Appendix 99

List of Figures

Figure 1-1 El Nino conditions (Based on NOAA, 2021). 4
Figure 1-2 Thesis framework. 8
Figure 2-1 Water flow in a rectangular slope. 11
Figure 2-2 Schematic representation of a DEM and DIR application to determine the location of the outlet. 13
Figure 2-3 Representation of flow drainage direction (DIR) (Taken for Kagetsu River). 14
Figure 2-4 Schematic representation of drainage and flow accumulation. (Taken from Akatani River basin). 14
Figure 2-5 Schematic representation of the drainage path (DIR) in a digital elevation scheme and the flow direction and the graphic presentation of a slope unit element. 15
Figure 3-1 Methodology applied to validate the results and model application in Japan and Peru. 19
Figure 3-2 Differential sediment control volume, similar fluxes in *y* and *z* axis were considered. 20
Figure 3-3 Schematic representation of the physical sediment transport process. The hillslope process is dominant at upstream cells (green shade zones), before reaching accumulation threshold. Afterwards, the conditional statement assigns the following elements to river process where water flow also produces erosion (blue shaded zone)... 22
Figure 3-4 Four-point solution model scheme for the parallel sediment concentration calculations. 24
Figure 3-5 Sediment concentration storage for sediment routing process. 25
Figure 3-6 Model processes flowchart. The output from the kinematic wave equations being current discharge $Q_{C[i]}$ and next time step discharge $Q_{n[i]}$ are stored in a temporal memory. The subscript [i] denotes the current spatial division, whilst the initial simulation loop $i = 0$ considers the initial surface water depth by using initial runoff height (mm h^{-1}). Alongside other inputs at the upper box, the sediment model calculates the concentration CS_c and sediment flow Q_C ending the first iteration.. 27
Figure 4-1 Akatani River location. 30

Figure 4-2 Flow drainage model (DIR). Every element was assigned with a flow direction number that will determine the drainage direction in the simulation (DEM data source: MLIT, 2018). 31
Figure 4-3 Flow accumulation number (flowacc). The number of elements connected from upstream according to the drainage direction DIR. The element with the highest accumulation number was assigned as the basin outlet. The cells with an accumulation number higher than 12,000 were defined as river cells, and the section between P1 and P3 is our sedimentation study area. 31
Figure 4-4 River flow hydrographs simulations for the outlet (P1) of the Akatani River basin (at 10 m and 100 m spatial resolutions) compared to the synthesized rational method estimated by RSRTC (July 5th, 2017). 34
Figure 4-5 Simulation results from Figure 4-3 analysis points: outlet (P1), critical point for maximum concentration (P2), and the junction point where the upper tributaries merge with the main river (P3). (a) Sediment concentration results. (b) Bed elevation change for the first 40 hours. The high-resolution DEM river model and sediment discharge allows for the one-dimensional simulation of the riverbed elevation over time (July 5th to 6th, 2017). 35
Figure 4-6 River Bed profile comparison River bed profile elevation comparison (m a.s.l.). Results presented here belong to the 48th hour of simulations. The expected result, according to the RSRTC survey, is a net river aggradation. 36
Figure 4-7 Sub basin identification and location of flat land (Source: RSRTC 2018 Report). 38
Figure 4-8 Sediment transport calculations after the event for 10 m and 100 m resolutions. 39
Figure 5-1 Tumbes River Location and elevation range. 42
Figure 5-2 DEM and the *flow accumulation number* cells that outlines the reach of the river process. The location of the three rain gauges and the discharge station in the study area are displayed. 44
Figure 5-3 Hydrological model DEM grid slope unit representation. The erosion process at slopes includes DR and DF, whereas river process is controlled by DF. 45
Figure 5-4 2016 rainy season hydrological simulations by 500 m and 1,000 m model. .. 47
Figure 5-5 Log-log correlation between monthly mean discharge ($m^3.s^{-1}$) and monthly mean suspended sediment ($mg.L^{-1}$). The 1,000 m resolution 1KDHM monthly average

simulation results are overlayed in the green diamond markers and well fit to the observed data from processed by Morera (2014) and published by the IGP in the white circle markers. 49
Figure 5-6 Sediment concentration (mg.L^{-1}) at 500 m and 1,000 m resolution model baseline. The sediment samples were taken at the same location as the discharge gauging station... 49
Figure 5-7 Suspended sediment yield (t.km^{-2}.y^{-1}) at the northern coast of Peru from long-term series. For Tumbes River (Basin B) the expected sediment yield after a rainy season is in the range of 341 to 556 t.km^{-2}.y^{-1}. Suspended sediment yield estimations were published by Morera (2014). 51
Figure 5-8 SSY results comparison at 500 m and 1,000 m resolutions for each parameter range. The yellow bar represents satisfactory range for SSY results (341 to 556 t.km^{-2}.y^{-1}). 52
Figure 6-1 Tumbes River basin DEM and river delimitation at 1 km resolution............ 57
Figure 6-2 Location of El Nino regions. For our research Region 3.4 and 1+2 interaction is for particular interest.. 58
Figure 6-3 Historical gauging rainfall intensity P recorded at the Peruvian gauging station. The presence of ENSO is called in the white boxes. The orange shaded area belongs to the period in which sediment sampling was carried out.. 59
Figure 6-4 Sediment concentration and river flow simulation results for strong ENSO presence. 62
Figure 6-5 Simulated sediment concentration. 63
Figure 6-6 Tumbes River discharge-sediment concentration relationship. The monthly average simulation for non-ENSO years is displayed in the green diamond markers. The historical average for non-ENSO years is displayed in the background (2004 to 2014 samples originally taken by Morera (2014)). 64
Figure 6-7 Sediment samples and simulations for rainy season in 2012. Simulation results for year 2012 are plotted over sampling data according to Quincho (2015). 66
Figure 6-8 Sediment samples and simulations for rainy season in 2014. Simulation results for year 2014 are plotted over sampling data according to Quincho (2015). 66
Figure 6-9 Sediment samples and simulations for rainy season in 2016. Simulations results for year 2016 are plotted over sampling data according to Goyburo (2017).................... 66

Figure 6-10 Tumbes River rating curves based on simulations for relevant years regarding ENSO presence. The black bold rating curve is the power regression for the 2012 to 2016 complete set of simulations. 67
Figure 6-11 Difference of rating curves according to range of the exponent *b* (a), and according to range of the coefficient *a* (b).......... 68
Figure 6-12 Hysteresis loop after Strong ENSO years 1983(a) and 1998(b) using simulated results (Historical non-ENSO background data in white circle markers is based from IGP and (Morera, Condom, Crave, Steer, & Guyot, 2017)). 72
Figure 7-1 Anomaly of ENSO in the transverse Andes at latitude 5°S. Based on Barry (2008).......... 77
Figure 7-2 Historical monthly average observed discharge at Gauging Station, it includes the monthly average simulations for relevant ENSO events. 78
Figure 7-3 Historical daily average observed discharge at Gauging Station, according to the degree of ENSO. 79
Figure 7-4 Anomalies in rainfall intensity in reference the ENSO presence (This is in reference the months of January to April, based on the isohyet formats published by the SENMHI (2021) and INGEMMET (2006)). 80
Figure 7-5 Total rainfall for year 1983, this is a schematic representation of the spatial distribution at 1 km resolution according to 1K-DHM point2dist. 81
Figure 7-6 Daily average sediment concentration simulations for strong ENSO events (years 1983 and 1998), weak ENSO 2016, and 2012 defined as a regular year. 82
Figure 7-7 Cumulative sediment transport volume simulations (millions of tones after the outlet) for strong ENSO events (years 1983 and 1998), weak ENSO 2016, and 2012 defined as a regular year. 82
Figure 7-8 Year 1983 estimated sediment concentration (C_S) by 1KDHM simulation under the higher rainfall peak (1-hour intervals). 83
Figure 7-9 Year 1998, estimated sediment concentration (C_S) by 1KDHM simulation under the higher rainfall peak (1-hour intervals). 84
Figure 7-10 Year 2012, estimated sediment concentration (C_S) by 1KDHM simulation under the higher rainfall peak (1-hour intervals). 84
Figure 7-11 Year 2016, estimated sediment concentration (C_S) by 1KDHM simulation under the higher rainfall peak (1-hour intervals). 85

Figure 7-12 Year 1983, estimated sediment accumulation by 1KDHM in terms of bed elevation difference after the last day of the month of May. 86
Figure 7-13 Year 1998, estimated sediment accumulation by 1KDHM in terms of bed elevation difference after the last day of the month of May 86
Figure 7-14 Year 2012, estimated sediment accumulation by 1KDHM in terms of bed elevation difference after the last day of the month of May. 87
Figure 7-15 Year 2016, estimated sediment accumulation by 1KDHM in terms of bed elevation difference after the last day of the month of May. 87

List of Tables

Table 4-1. Hydrological model parameters including Manning coefficients, and depth of soil layers for groundwater simulations. Time step and spatial division account for convergence in simulations.. 32

Table 4-2. Sediment model parameters. Particle size, settling velocity, and conductivity are based on average values for mountain regions in Fukuoka. Detachability and stream power are based on empirical values according to Morgan et al. (1998). 33

Table 4-3. Sediment transport comparison between RSRTC and simulations at 10 m and 100 m resolutions.. 37

Table 5-1 Hydrological parameters for each resolution. 47

Table 5-2 Sediment model parameter baseline for each resolution................................... 48

Table 6-1 Hydrological parameters during important years for the analysis. 61

Table 6-2 Sediment simulations parameters... 61

Table 6-3 Sediment rating curve for the representative simulation years. 67

Table A-1 2011-2012 gauging station recorded discharge (m^3 s^{-1})................................. 99

Table A-2 2012-2013 gauging station recorded discharge (m^3 s^{-1})................................. 99

Table A-3 2013-2014 gauging station recorded discharge (m^3 s^{-1})............................... 100

Table A-4 2014-2015 gauging station recorded discharge (m3 s^{-1}) 101

Table A-5 2015-2016 gauging station recorded discharge (m^3 s^{-1})............................... 101

Table A-6 List of gauging stations in study areas in Peru, operation by SENAMHI..... 102

Table A-7 List of gauging stations in study areas in Peru, Ecuador, operation by INAMHI 102

Table A-8 The soil parameters for Tumbes River basin in Chapter 5 were calibrated according to a range of characteristics extracted from test pits, we referred to those results to establish initial parameter values (Original source: (ANA, 2014), Table G6 and pp. 58-61).. 102

Abbreviations

JSCE	Japan Society of Civil Engineering
XRAIN	eXtended Radar Information Network
JAXA	Japan Aerospace Exploration Agency
GSMAP	Global Satellite Mapping of Precipitation, JAXA
HWRL	Hydrology and Water Resources Research Laboratory (Kyoto University)
USGS	United States Geophysical Service
INGEMMET	Instituto Geologico Minero y Metalurgico (Mining and Metallurgic Geological Institute, Peru)
SENAMHI	Servicio Nacional de Meteorologia e Hidrologia (National Hydrology and Meteorology Service, Peru)
INAMHI	Instituto Nacional de Meteorologia e Hidrologia (National Institute of Meteorology and Hydrology, Ecuador)
ANA	Autoridad Nacional del Agua (National Water Management Authority, Peru)
IGP	Instituto Geofísico Del Peru (Peruvian Geophysical Institute)
PEBPT	Proyecto Especial Binacional Puyango Tumbes (Binational Project for the Tumbes-Puyango River Management)
NOAA	National Oceanic and Atmospheric Administration (United States of America)
SOI	Southern Oscillation Index
SST	Sea Surface Temperature
UTM	Universal Transverse Mercator
DEM	Digital elevation model

DIR	Digital drainage direction
ENSO	El Nino Southern Oscillation
SEN	Strong El Nino (ENSO)
WEN	Weak El Nino (ENSO)
SSC	Soil sediment Concentration
TR	Transport by raindrop impact

Chapter 1. Introduction

1.1 Background

This study contains information obtained as a result of research conducted in both Peru and Japan and includes an overview of the issues encountered throughout the doctoral program. The study focuses on the investigation of extreme rainfall events and the consequences of floods (in terms of economic issues and the negative effects on human life exerted via flooding). Research suggests that flooding is the result of a series of basin alterations. The present study is based on the numerical simulation of extreme events that trigger erosion, which concurrently trigger the transport of sediments, causing inundation by floods in the lower basin. The background information presented below summarizes the direction and rationale of this doctoral research:

1.1.1 Rainfall-runoff models and the relationship with sediment transport

A hydrological model that be used by incorporating the topographical features of a target basin is a critical tool using which aspects of rainfall runoff and sediment predictions can be studied. Kirby published a series of *Landscape Systems* articles in the 1970s, which was a compilation of the current works describing the characteristics of hillslope hydrology at the time. The publications focused on the implications of sedimentary transport (Kirby, 1978, pp. 338-344) and the importance of rainsplash in the washing process (for sediment flow).

The development of lumped models occurred in the late 1970s, along with the establishment of the Universal Soil Loss Equation (USLE) (Wischmeier & Smith, 1978), the Revised Universal Soil Loss Equation (RUSLE) (Renard, Foster, Weesies, McCool, & Yoder, 1997) and the Modified Universal Soil Loss Equation (MUSLE) in the field of agricultural science. The aforementioned models were developed and successfully applied to agricultural processes; however, application was limited to small and middle-sized basins (usually less than 10 km^2).

Research efforts and discussions on physical-based sediment routing were initiated after the development of distributed models that could be applied to larger basins. In Japan, a country known for its steep topographical features and significant erosion processes, the modeling approach consists of connecting several slope units; several published studies (Takahashi, Inoue, Nakagawa, & Satofuka, 2000) highlighted methods that were based on the Kinematic wave equations proposed by (Egashira S. , 1998), that focused on a larger scale and included aspects of drainage dimensions and sedimentary transport.

Based on a review of the relevant previously reported literature, the purpose of this study was the development of a distributed hydrological model for which the governing equations were suited to the hillslopes surrounding steep basins. Elements such as the impact of raindrops and sedimentary transport have been included, and the kinematic wave equations have been considered with the expectation of achieving satisfactory results in the context of Japanese hydrology. The approach of using kinematic wave modeling to integrate rainfall-runoff data with sediment transport models has been discussed, and the assumptions used to study sedimentary transport in Peru have been stated.

1.1.2 Rainfall-runoff models in Japan and Peru

After application in Japan, other studies related to the assessment of sediment disaster field and flooding have been addressed. The Tumbes River basin, which is located on the Peruvian Northern Coast, was selected after the conduction of a careful literature review and feasibility analysis in accordance with data availability.

Lumped models were most commonly applied to describe the Peruvian coast in the 1970s, 1980s, and the first half of the 1990s, which relied on the consideration of appropriate parameters, digital topography, and calibration techniques. As new monitoring and *in-situ* survey instruments became available, lumped models were found unsuitable to fully reproduce the instant response to extreme events that occurred in middle and lower basins (MEF, 1999). The ENSO event in 1998 rendered it necessary to improve simulations and to reduce the uncertainties inherent in basin management such that future scenarios could be accurately established. Additionally, a report detailing the study of sediment transport and sediment dynamics after the 1990s in this basin (Nuñes & Zegarra, 2006) revealed the presence of high concentration fluxes, with the observation of hyperconcentrated fluxes at certain locations (known a “huaycos” in Spanish).

The modeling approach based on the division of hillslope hydrology into slope units is similar to the approach that has been used to describe neighboring basins in the Peruvian Andes with basin outlets located on the Pacific Coast, as well as basins in Colombia. A particular tendency for sedimentary transport after the occurrence of ENSO events has been reported in this area (Kettner, Restrepo, & Syvitsky, 2010).

1.1.3 ENSO and the generation of sediment

The data that were used to define the ENSO were obtained from the National Oceanic and Atmospheric Administration`s Physical Sciences Laboratory (NOAA), which described interactions between the ocean and the atmosphere.

Under normal conditions, the trade winds blow in a westerly direction towards Australia-Asia, where the sea surface temperature (SST) is 8 °C warmer than the eastern Pacific.

Under El Nino conditions, the wind trade is weak. The literature (NOAA, 2021) refers to this situation as a depression in the thermocline **Figure 1-1** in the Eastern Pacific with an increase in the Western Pacific (the study area). The overall result is an increase in the SST of the Eastern Pacific that leads to the development of a stationary cumulus system.

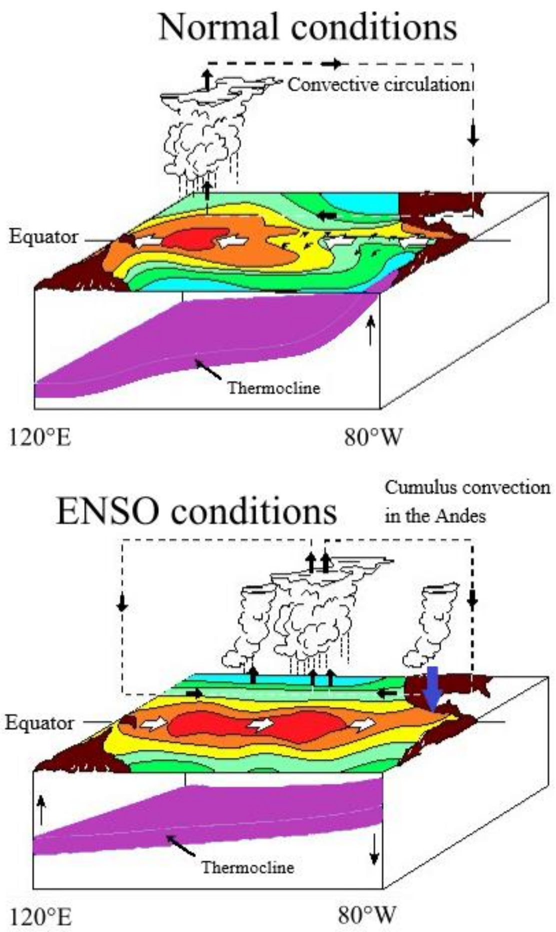

Figure 1-1 El Nino conditions (Based on NOAA, 2021).

These conditions were relevant to this study because of the strong ENSO event that occurred in the area in 1983, when a major sediment disaster was reported (Mirjam, Ros-Tonen, & van Boxel, 1999).

For this study, an understanding of historical ENSO events is important for the validation of the model parameters and for the consideration of these parameters to operate the model with less uncertainties associated with inputs on rainfall. Hence, in **Section 6.5,** the effects of ENSO on the production of sediment and the sensitivity of the produced model to the range of soil parameters used have been discussed.

Subsequent chapters in this thesis have focused on the anomalies in sediment transport that are observed under the effects of the ENSO phenomenon, based on which a hypothesis has been formulated to both describe the effects of hydrology and to understand the manner in which hydrology affects the transport of sediments.

1.1.4 The context of an integrated sediment model for river management

Strong El Nino events exert negative effects on the regional economy and often result in intense flooding that leads to isolation of the affected cities (Tumbes and Piura). The return period of a strong ENSO phenomenon cannot be estimated with the short simulations considered in current climate models; however, ENSO was observed in 1983, 1997, and most recently in 2017 (under special patterns that the Peruvian scientific community denoted ENSO of the Coast, or “El Nino Costero” in Spanish), suggesting a quasi-periodic return period of 7 years.

The special Project Tumbes-Puyango is a collaborative project that is being conducted by the governments of Peru and Ecuador to establish measurement systems, river management strategies, and prediction tools to formulate emergency measures that can be used to confer protection to cities that are under the threat of flooding.

This collaborative effort has allowed access to important records detailing the gauged discharge and rainfall in both countries.

1.1.5 Rating curves (adjustment after events, forecast, improvements)

The rating curves produced in latest publications is one of the most accepted methods by the scientific community to describe and make forecast about the effects of ENSO.

1.2 Objectives

Considering the points mentioned in the background, the objectives of this study are as follows:

1. to develop an integrated rainfall-runoff and sediment routing model that can be used to simulate the dynamics of erosive basins;
2. to understand and describe the sediment routing mechanics involved during ENSO events through mathematical relationships;
3. to reduce prediction uncertainties by identifying the sensitive model parameters and the effects of extreme events in steep basins in terms of sediment routing; and

4. to generate sediment rating curves (that describe the relationship between river flow rate and sediment concentration) that are applicable for forecasting future ENSO events and for analyzing the behavior of the sediments during extreme floods.

1.3 Outline of the thesis

In this study, a distributed rainfall-runoff and sediment routing model was developed based on one-dimensional kinematic wave equations with an aim to reproduce the hydrological and sediment transport processes that were inherent in basins prone to erosive process. In **Chapter 2**, a method to solve and apply the physically-based rainfall-runoff and erosion-sediment processes has been described and presented. The components were coded to present a sequential solving algorithm for each spatial grid, and the spatially distributed grids were connected to each other to facilitate the spatial and temporal movements of the water and sediment.

In **Chapter 3**, the methodology to integrate the rainfall-runoff model and sediment routing model is described. The first part of the chapter introduces the background regarding hydrological models suited for steep basins and the modelling idealizations incorporated as mathematical relationships. The second part explains the sediment transport governing equations and the method to slit the process (channel or slope), explaining the pertinent inclusion of the detachment by flow and/or detachment by raindrop impact. Finally, the method to process bed elevation change is described.

In **Chapter 4**, the application of the sediment routing model to the Akatani River basin (21 km^2) of the Chikugo River in Kyushu, Japan, has been discussed. Using a 10-m high-resolution digital elevation model (DEM) shared by the MLIT, followed by a discussion on the data acquired from the eXtended RAdar Information Network (XRAIN) to describe the time-and-space distributed rainfall input of the northern Kyushu heavy rainfall event in July 2017. This application was performed based on the data available for input rainfall, the high-resolution topography before and after the event, and the discharge gauged data describing the surrounding river basins. The sediment transport estimations for the tributaries have been compared to relevant published reports as a reference for sediment budget balance.

In **Chapter 5**, application of the model to the Tumbes River basin (5400 km^2) on the Peruvian coast has been discussed. The objective was to verify the algorithm and the feasibility of reproducing sediment dynamics and to conduct comparisons with the data collected by the Peruvian Meteorological Institute (SENAMHI). It was found that sediment transport results showed sensitivity to the spatial resolution of the model used (the model was run at both 500-m and 1-km resolutions).

In **Chapter 6**, results have been presented and indicated that the rainfall-runoff hydrograph and the sediment flow results were in agreement with the collected field data, and that the conditions describing an elevation of the riverbed after occurrence of the disaster were successfully reproduced by applying a sediment theory to estimate the variation in the riverbed. Preliminary analysis of the sediment ratings curves showed positive findings and the log-log relationship between daily average sediment transport and discharge could be considered a reliable assessment method. This model is intended for use with basins that feature steep slopes and are prone to erosion and reduction in shear strength after the occurrence of heavy rainfall events. Hence, this model can be applied to provide early warnings via identification of critical areas that are prone to erosion during heavy rainfall events that are forecasted.

In **Chapter 7,** the effects of the ENSO phenomenon based on the literature review have been summarized and contrasted with the results of this study. The interaction with the hydrological processes that were recorded over the period 2012 to 2016 has been highlighted. In this section, the notion that the ENSO phenomenon will increase the rate and intensity of sedimentary transport along the Peruvian Northern coast is described based on the sediment rating curves derived and presented in Chapter 6.

Chapter 8 includes the concluding remarks and information on the possible future research, comments on the future benefits of applying computer models, and highlights a means of extending the algorithm.

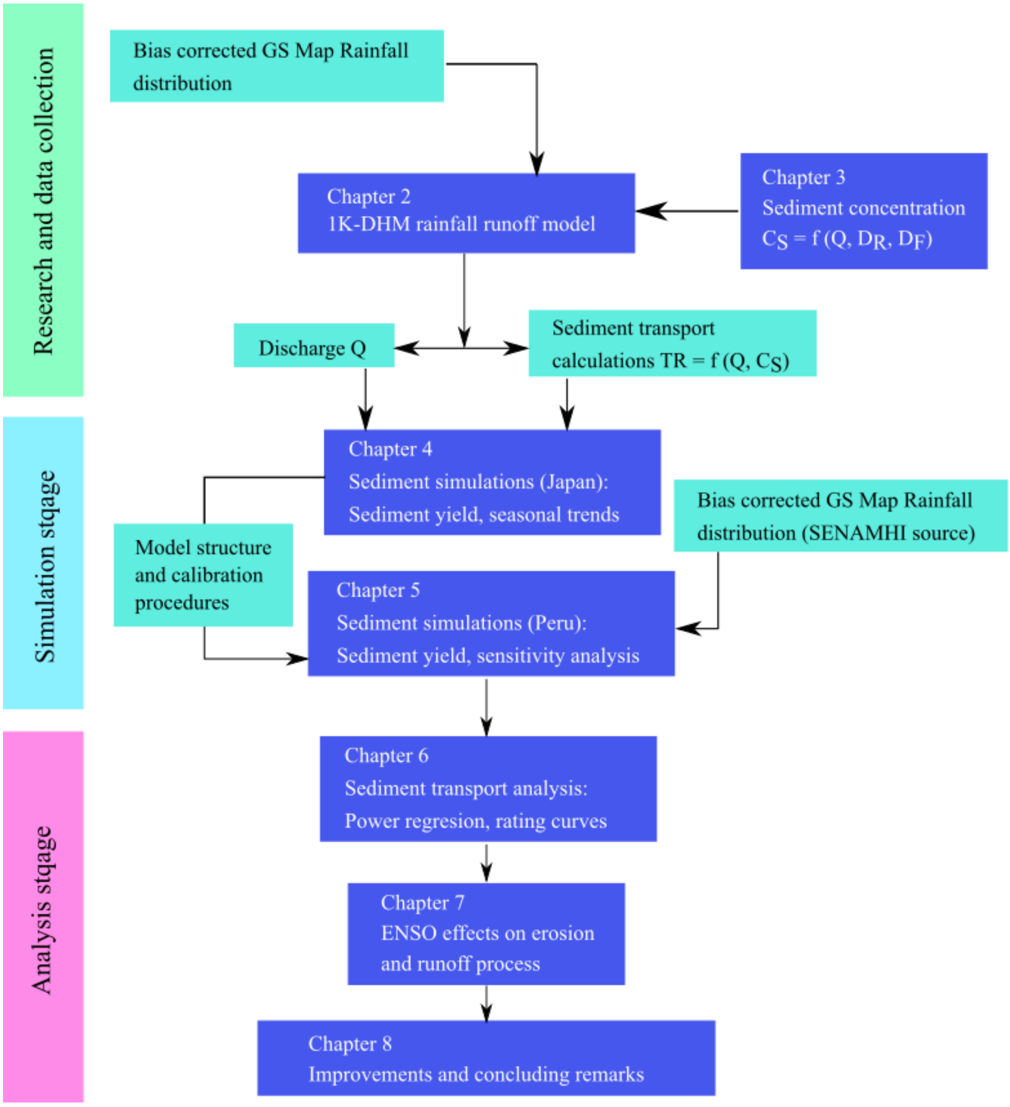

Figure 1-2 Thesis framework.

Chapter 2. Construction of a rainfall-runoff model for sediment routing

2.1 Introduction

The use of kinematic wave equations is an appropriate approach which can be considered for modeling the physical hydrological processes of basins that feature steep topography (the Andes in subsequent chapters). The distributed hydrological model that was used in this study comprised rectangular slopes that were connected to each other. The steep slopes on the upper and middle catchments are represented using a DEM with a 10-m resolution to describe the Akatani River basin in Japan (Chero, Tachikawa, Yorozu, & Ichikawa, 2020) and DEMs with resolutions of 500 m and 1 000 m for describing the Tumbes River basin in Peru (Chero et al., 2020b). By setting an appropriate range of model parameters, models with higher resolutions may provide reasonable simulation accuracy in every grid cell.

The concept and basic equations used in the distributed hydrologic model 1K-DHM are introduced in Section 2.2. The input data used in 1K-DHM are explained in Section 2.3. The topographic data processing is shown in Section 2.4. Finally, the calibration method that was used to identify the model parameters has been described in Section 2.5.

2.2 Distributed model 1K-DHM

The basic concepts and the basin features that are suitable for application in the 1K-DHM (1 km Distributed Hydrological Model) developed at the Hydrology and Water Resources Laboratory in the Civil and Earth Resources Laboratory of Kyoto University, (Kyoto University, 2021) are described below.

Figure 2-1 depicts a schematic drawing of the water flow as represented by using 1K-DHM. Each grid consists of a slope element and a river element. Slopes are assumed to be located on both sides of the river element and the slope flow and river flow are described using the kinematic wave flow approximation.

The kinematic wave theory was applied for overland flow by categorizing the flow process into two: the rainfall-runoff on hillslopes, and the routed flow that occurs in the channel sections.

The kinematic wave equation consists of the continuity equation Eq. 2.1 and the momentum equation Eq. 2.2 expressed in terms of storage and flow. The solution of these equations was obtained in accordance with methods described in a previous publication by Beven (2012).

The equations governing flow for each rectangular slope are based on the kinematic wave equations (Tanaka & Tachikawa, 2015). The one-dimensional mass balance continuity equation for each river cell is expressed as:

$$\frac{\partial A}{\partial t} + \frac{\partial Q}{\partial x} = q_L \tag{2.1}$$

where A represents the cross-sectional area of flow, Q represents discharge, and q_L represents lateral inflow per unit width.

The momentum equation used for the kinematic wave equation is expressed as:

$$\frac{1}{g}\frac{\partial u}{\partial t} + \frac{u}{g}\frac{\partial u}{\partial x} + \frac{\partial h}{\partial x} = I_0 - I_f - \frac{u q_L}{gA} \tag{2.2}$$

where h represents the water depth, g represents gravitational acceleration, u (=Q/A) represents the mean flow velocity, I_0 represents the bed slope, and I_f represents the friction slope.

The momentum equation can be solved using the Manning equation for a rectangular cross-section expressed below:

$$Q = \alpha A^m, \alpha = \frac{\sqrt{I_0}}{n}\left(\frac{1}{B}\right)^{m-1}, m = \frac{5}{3} \tag{2.3}$$

where B represents the width of the flow section, and n represents the Manning roughness coefficient.

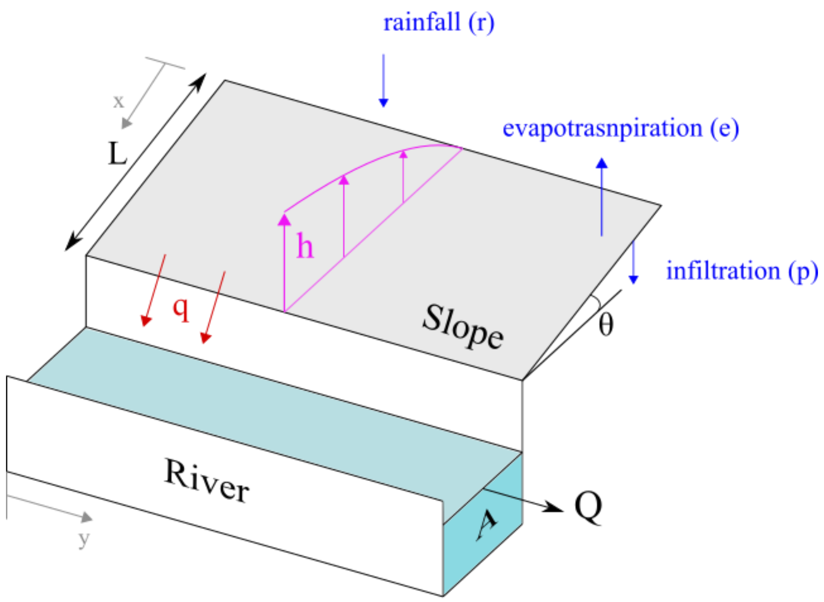

Figure 2-1 Water flow in a rectangular slope.

The discharge-depth relationship for hillslope flow is extended to integrate information on the overland flow with a subsurface flow simulation according to the saturation level and the thickness of the layer. Hence, the mathematical relations for slope and subsurface flow are as follows:

$$q = \begin{cases} d_c k_c \left(\dfrac{h}{d_c} \right)^{\beta} i & (0 \le h \le d_c) \\ d_c k_c i + (h - d_c) k_a i & (d_c \le h \le d_a) \\ \dfrac{\sqrt{i}}{n_s} (h - d_a)^m + (h - d_c) k_a i + d_c k_c i & (d_a \le h) \end{cases} \tag{2.4}$$

where h represents the water depth equivalent to the water content with the effective porosity, d_a represents water depth equivalent to the maximum water content with the effective porosity, d_c represents the water depth equivalent to the maximum water content in the capillary pores, k_c exhibits relation to the hydraulic conductivity when the capillary pore is saturated, β represents an exponential parameter that describes the relationship between hydraulic conductivity and saturation, k_a refers to the saturated hydraulic conductivity, and $k_a = \beta k_c$, according to the continuity of the relationship shown in Eq (2.4). Furthermore, n_s represents the Manning's roughness coefficient for overland flow in the slope runoff cells, and *i* represents slope gradient. Considering that the subsurface soil layer at hillslopes has high conductivity, it has been assumed that the surface soil layer is unsaturated prior to the occurrence of the rainfall event.

2.3 Generation of spatial distributed rainfall

Information on precipitation was used as an input according to the reports obtained from the nearby station and was processed as a preliminary step to generate the input rainfall file for 1K-DHM. A programming tool in C++ language under the name “point2dist” was used to generate data on the spatial distribution of rainfall based on the gauged rainfall data.

Evapotranspiration (ET) is not considered for the relatively small timeframe (48 h) associated with the data obtained for Akatani River in Japan. The rainfall data were extracted from those available at the JMA weather monitoring website and the Extreme Rainfall Report for Chikugo River in 2018.

2.4 Estimation of evapotranspiration at the Tumbes River basin

ET was included for the Tumbes River Basin in Peru, using data obtained from the SENMHI reports. A detailed description of the Tumbes River Basin is provided in **Section 6.3.** ET assessment is more relevant when extended periods for the basin are observed wherein rainfall is absent and dry conditions prevail.

2.5 Topographical features and basin processing

1K-DHM is used to incorporate data on important features that are derived from both DEM and DIR. First, to process data on the size of the basin and to establish the flow routing path, the code is used to read the values obtained via application of the digital drainage model (DIR) and is used to calculate the number of cells that will flow into the downslope cells (referred to as the “Flow accumulation number”). The performance of iterations continues until the flow that has accumulated in a cell cannot be transferred to any other cell. It is possible to have more than one river in reach of the DEM input; hence, it is recommended that a basin is clipped from the DEM once the target basin has been located to save memory space.

Next, the program is used to assign the cell that demonstrates the highest flow accumulation value as the outlet. This is presented schematically in **Figure 2-2.**

Additionally, to determine the river path gradient and slope gradient for momentum equations, the model is used to process the data input according to the elevation data in the DEM from cell to cell. To understand these features, the DIR plotted in **Figure 2-3** includes the flow accumulation number illustrated in **Figure 2-4;** for this purpose, data have been extracted based on investigation of Kagetsu River, which were used in the model development and debug stage.

Finally, the schematic description of the computed routing process is derived from the DEM, DIR, and the "Flow accumulation", as represented in **Figure 2-5.**

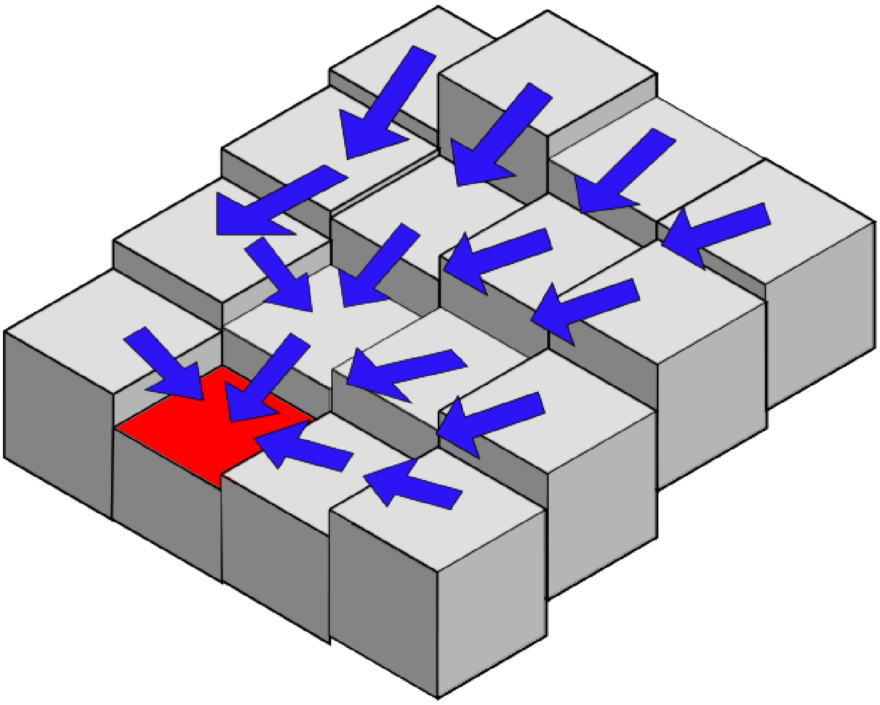

Figure 2-2 Schematic representation of a DEM and DIR application to determine the location of the outlet.

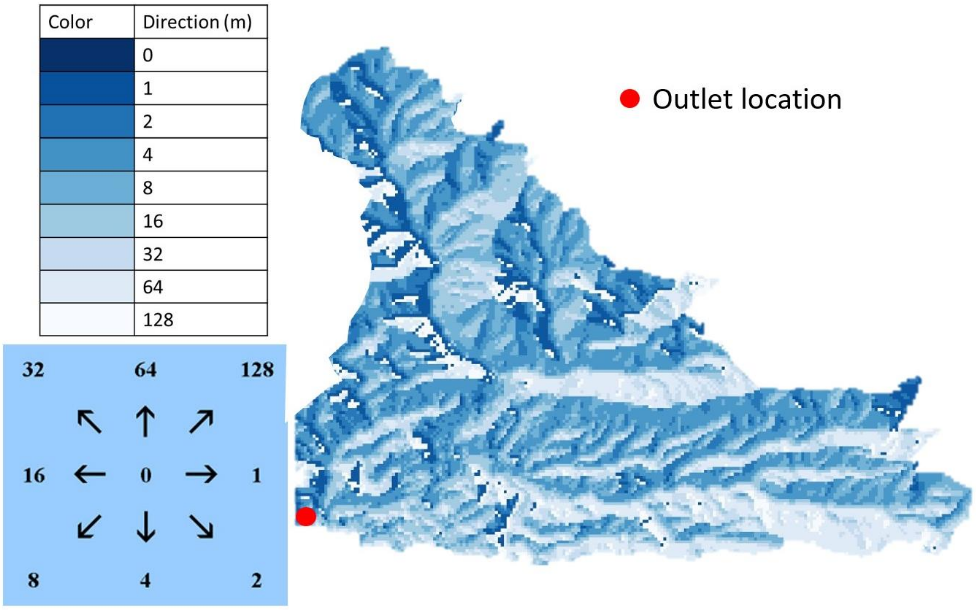

Figure 2-3 Representation of flow drainage direction (DIR) (Taken for Kagetsu River).

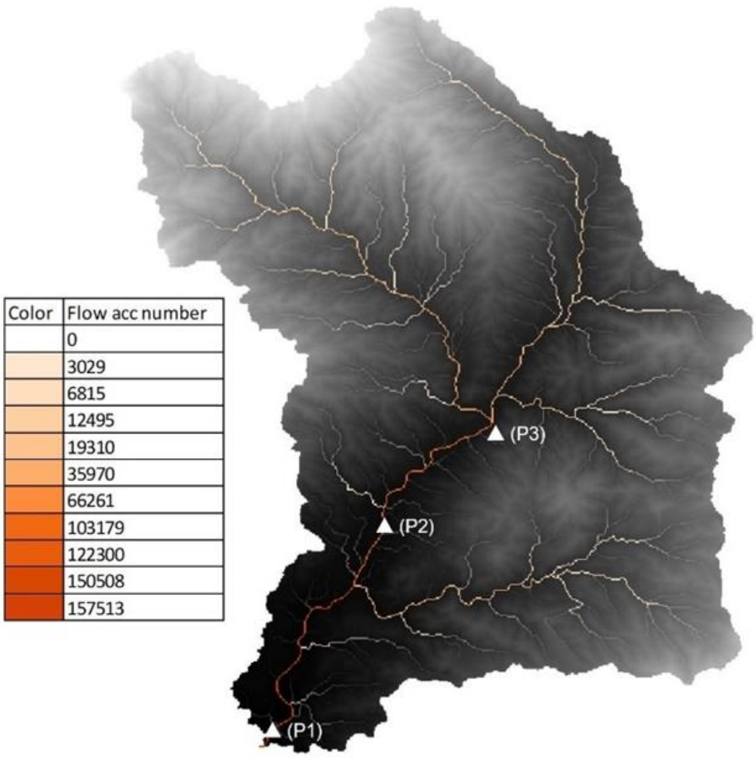

Figure 2-4 Schematic representation of drainage and flow accumulation. (Taken from Akatani River basin).

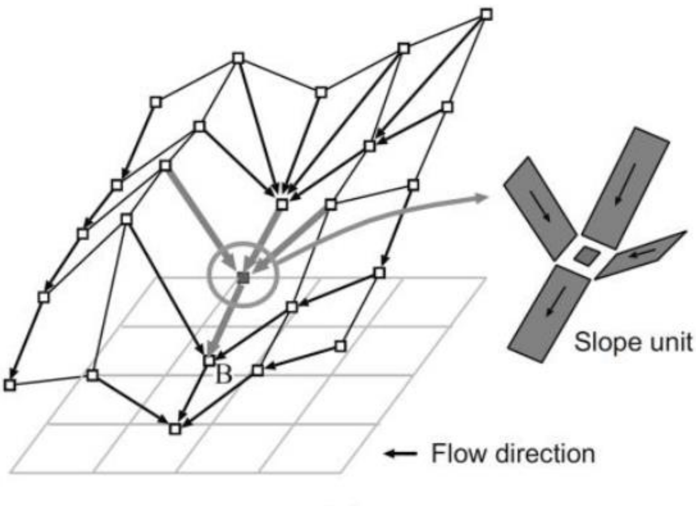

Figure 2-5 Schematic representation of the drainage path (DIR) in a digital elevation scheme and the flow direction and the graphic presentation of a slope unit element.

2.6 Calibration of the 1K-DHM

The parameter calibration was performed using the Shuffle Complex Evolution - University of Arizona (SCE-UA) algorithm (Seong, Her, & Benham, 2015).

Hydrographs derived from the rational method applied to the Akatani River data were used as reference. Further details on this process are described in Section 4.3 (source Kyushu Regional Bureau, MLIT). For the illustration of sediment graphs for Akatani River, estimations were conducted using reports obtained from the Kyushu Regional Bureau to generate a reference for the volume of sediment transported in the sub basin.

Historical discharge data obtained from the Peruvian Meteorological Service were considered to perform calibration of the Tumbes River hydrological model parameters and have been presented in Chapter 5.4. Meanwhile, data provided by the Peruvian Geophysical Institute were used to perform calibration of the sediment transport and have been presented in Section 6.5; additionally, sensitivity analysis was performed by considering the scaling factor from 500-m to 1-km resolution in terms of topography.

(This page intentionally left blank)

Chapter 3. Development of a sediment routing model coupled with a distributed rainfall-runoff model

3.1 Introduction

Extreme rainfall events occurring during the rainy season and typhoon in Japan have often resulted in flash floods and sediment-related disasters. The extreme rainfall event in Kyushu in July 2017 captured the attention of both the local authorities and the scientific community due to the extreme nature of the sediment disaster. A report on the flooding and the sediment-related effects was published following the Kyushu event; an assessment was performed by the River and Sabo Restoration Technology Review Committee and entailed sedimentation analysis based on the data acquired using a laser profiler and aerial photographs obtained before and after the event for the right bank of the Chikugo River (RSRTC, 2018). The published report included a thorough geophysical assessment of the considerable volume of sediment that was transported during the event and led to an increase in the elevation of the riverbed.

Numerical simulation in most hydrological models relies on the provision of accurate data on rainfall, topography, and soil mapping information. For accurate flood simulations, the volume of transported and deposited sediment in a riverbed should also be considered a critical factor (Kawaike, Yamada, & Nakagawa, 2018). Although currently available hydrological models that were developed in the last 10 years, such as the Soil & Water Assessment Tool (SWAT) (Arnold, et al., 2012), the TOPography-based hydrological model (TOPMODEL) (Beven & Freer, 2001), and the Water Erosion Prediction Project (WEPP) model (Laflen, Lane, & Foster, 1991), have been used to obtain satisfactory results, there have been concerns regarding the physical assumptions and parameter calibration processes used in these models (Hajigholizadeh, Melesse, & Fuentes, 2018). The conceptual models listed above are used to simulate sediment routing via application of the physical processes; nevertheless, the transport mechanism for highly erosive and steep rivers requires the consideration of a specific model-based approach. Egashira & Matsuki (2000) proposed a method to resolve sediment transport for a complex channel network into a single channel unit with two inflow points and one outflow point, which has been considered relevant given the satisfactory results obtained thus far when using this technique in hydrological and sediment predictions. Thus, a fully distributed model that included water flow and sediment transport with an extremely high-resolution DEM was designed. Furthermore, an extended algorithm was used to establish connections between every differential element according to the DIR and has been discussed in the subsequent section.

This study explored the applicability of the aforementioned distributed hydrological model to study the 2017 Northern Kyushu extreme rainfall event that occurred in the Akatani River basin (21 km^2) with reference to the results of the RSRTC assessment (RSRTC, 2018). This chapter describes a new approach in the development of a spatially distributed model that considers both hillslope rainfall-runoff erosional processes and the routing and transport processes involved in a river channel system. This approach considered findings of a previous study conducted by Ferro and Porto (2000), who emphasized the relevance of modeling hillslope and channel erosion as two processes with two different governing equations, namely Eq. 3.7 (for channel processes) and Eq. 3.8 (for hillslope processes). An estimation of the soil erosion rate, sediment transport, and deposition at the allocated critical spots is conducted for this purpose.

The theory and methodology used in developing the sediment routing model is introduced in Sections 3.2 and 3.3. The governing equations for the distributed rainfall and sediment runoff model are described in Sections 3.4 and 3.5. The interaction between the erosion process with the rainfall-runoff model is a key component of the modeling, and it is numerically solved using a finite element method (FEM) presented in Section 3.6.

3.2 Methodology: sediment process-based component

The process used to operate the model and to determine the most representative parameters for the target basin is summarized in **Figure 3-1** in the following manner:

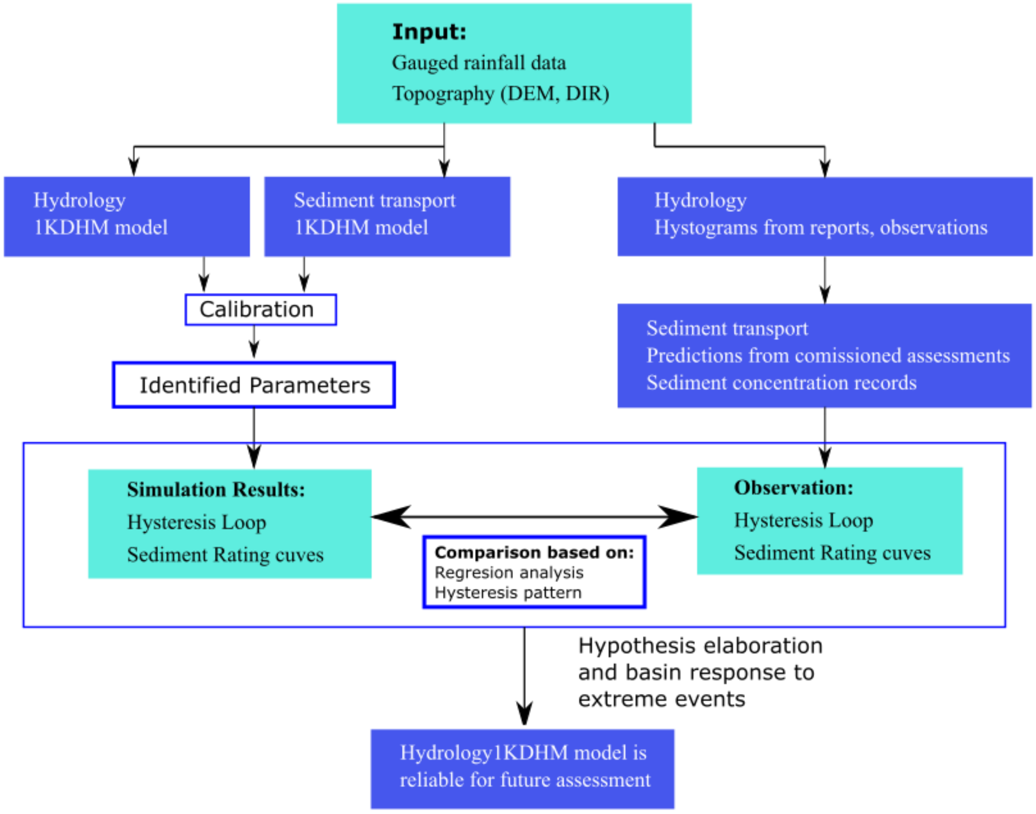

Figure 3-1 Methodology applied to validate the results and model application in Japan and Peru.

3.3 Sediment erosion-deposition model

The hillslope erosion process was modeled by considering both the impact of raindrops and the surface flow as the driving mechanisms responsible for the production of the sediment. The concept of stream power (Govers, 1990) was adopted for the erosion processes that were associated with surface flow, with the occurrence of soil detachment at the juncture when the stream power exceeded the critical stream velocity.

For the river routing processes, information on the sediment generated in upstream cells was incorporated into the river system. The distributed model comprises grid cells in which either hillslope erosion or river processes are dominant. The grid cells are classified as hillslope-related or river-related grid cells according to the flow accumulation number that is compared to a threshold value. Both the direction of flow and the information concerning the accumulation of sediments from the DEM were used as the governing parameters that could be used to control the modeling of sediment generation, transport, and deposition (see **Figure 3-3** for a graphical description of these two processes).

3.4 Sediment transport governing equation

The governing equation describes the conservation of sedimentary mass. This section is based on the findings reported by Julien (2018), and the mathematical assumptions and derivation used to solve the differential equation are based on the conservation of mass on 3 axes expressed as:

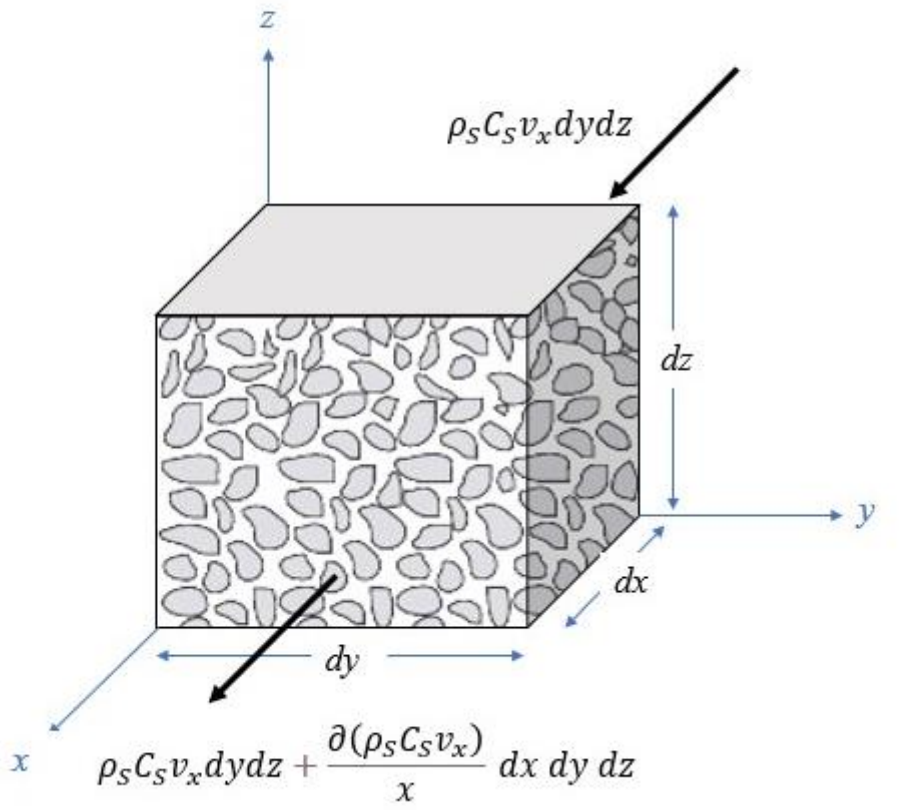

Figure 3-2 Differential sediment control volume, similar fluxes in *y* and *z* axis were considered.

The mass flux is considered to enter the x axis using the advective fluxes $\rho_S C_S v_x\ d_y d_z$, and the mass flux leaving the sediment control in the *x* direction is expressed as ($\rho_S C_S v_x dydz + \partial(\rho_S C_S v_x) d_x d_y d_z / x$).

$$\dot{m} = \frac{\partial}{\partial t}(\rho_S C_S)dxdydz$$
$$- \rho_S C_S v_x dydz + \left[\rho_S C_S v_x + \frac{\partial}{\partial x}(\rho_S C_S v_x)dx\right] dydz$$
$$- \rho_S C_S v_y dxdz + \left[\rho_S C_S v_y + \frac{\partial}{\partial y}(\rho_S C_S v_y)dy\right] dxdz$$
$$- \rho_S C_S v_z dxdy + \left[\rho_S C_S v_z + \frac{\partial}{\partial z}(\rho_S C_S v_z)dz\right] dxdy$$

$$\frac{\partial}{\partial t}(\rho_S C_S) + \frac{\delta}{\delta x}(\rho_S C_S v_x) + \frac{\delta}{\delta y}(\rho_S C_S v_y) + \frac{\delta}{\delta z}(\rho_S C_S v_z) = \frac{\dot{m}}{dx\,dy\,dz} \quad (3.1)$$

If constant soil density is considered, the expression can be reduced to the following:

$$\frac{\delta C_S}{\delta t} + \frac{\delta(C_S v_x)}{\delta x} + \frac{\delta(C_S v_y)}{\delta y} + \frac{\delta(C_S v_z)}{\delta z} = \dot{C}_S \quad (3.2)$$

where C_S represents the volumetric source per unit of time.

3.5 Governing differential equations for erosion and deposition

Governing equations: sediment conservation equations 2D to 1D. Solutions to differential equations.

The conservation of sediment mass is considered the basic governing equation that is used to perform modeling of soil dynamics (Morgan, et al., 1998). This equation is applied to every grid cell in the developed model as follows:

$$\frac{\partial(A \cdot C_S)}{\partial t} + \frac{\partial(Q \cdot C_S)}{\partial x} - e(x,t) = q_S(x,t) \quad (3.3)$$

Here, C_S represents the sediment volumetric concentration ($m^3\ m^{-3}$), A represents the cross-sectional channel area (m^2), and Q represents the flow discharge ($m^3\ s^{-1}$). The expression $q_S(x, t)$ represents the rate of external input or extraction in each grid cell as explained in the next sub-section. The net erosion rate $e(x, t)$ in the left-hand side of the equation represents the sum of detachment from surface flow *DF* and the rain drop impact *DR* according to the following equation:

$$e(x,t) = DF + DR \quad (3.4)$$

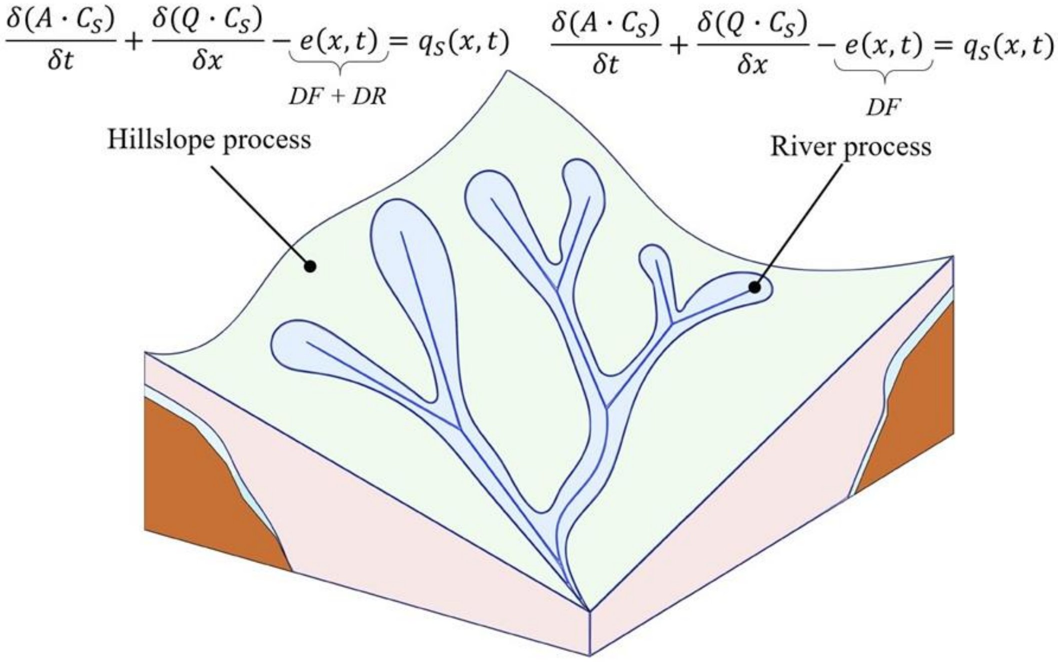

Figure 3-3 Schematic representation of the physical sediment transport process. The hillslope process is dominant at upstream cells (green shade zones), before reaching accumulation threshold. Afterwards, the conditional statement assigns the following elements to river process where water flow also produces erosion (blue shaded zone).

3.5.1 Sediment generation as a result of flow detachment (DF)

The soil detachment that results from flow *DF* is calculated using the sediment erosion-deposition theory. This aspect considers the dependence of *DF* on the difference between the current sediment concentration C_S (m^3 m^{-3}) and the transport capacity T_C (m^3 m^{-3}), which is the maximum concentration that the surface flow can harbor. According to the findings reported by Govers (1990), the expression for *DF* is provided as follows:

$$DF = \beta_S w v_S (T_C - C_S) \tag{3.5}$$

where β_s represents the flow detachment efficiency coefficient with a normal range from 0.4 to 1.0 according to the soil cohesion, *w* represents the surface flow velocity (m s^{-1}), and v_S represents particle settling velocity (m s^{-1}).

According to Eq. (3.5), it can be implied that the detachment by surface flow will decrease proportionally with an increase in the concentration of sediment. Detachment by flow does not occur when the concentration reaches the transport capacity.

3.5.2 Sediment generation as a result of raindrop impact (DR)

Soil detachment due to the impact of rainfall *DR* is a critical process in hillslope erosional simulations. Most laboratory experiments have demonstrated the mechanisms by which the momentum of a raindrop falling on the hillslope surface can generate erosion. One of the effects of rainfall is the initial compaction of the soil surface. Another effect, and the main source of the sediment production, is related to raindrops that possess sufficient kinetic energy for soil detachment (Poesen & Govers, 1986).

The following relationship has been proposed by Torri, Sfalanga, & Del Sette (1987) and is based on previous research:

$$DR = \left(\frac{k_{sd}}{\rho_S}\right) KE \cdot e^{-Zh} \tag{3.6}$$

Here, k_{sd} represents the soil detachment index ranging from 0.01 to 10 g J^{-1} according to the soil texture and shear strength, ρ_s represents the soil density (kg m^{-3}), $KE = 8.95 + \log(r)$, e^{-Zh} represents a correction factor that reduces the capacity of raindrop impact to produce sediment, r represents the rainfall intensity (mm h^{-1}), h represents the surface runoff depth (m), and Z represents the experimental exponent ranging from 0.9 and 3.1. The raindrop detachment is reduced when surface flow is present, with significant surface flow depths completely preventing soil detachment as a result of reduced raindrop impact.

The solution obtained by implementing the four-point method is derived and used based on Eq. 3.3 as follows:

$$\left.\frac{\delta(A \cdot C_S)}{\delta t}\right|_{i}^{i+1} + \left.\frac{\delta(Q \cdot C_S)}{\delta x}\right|_{j}^{j+1} - e(x,t) = q_S(x,t)$$

The notation relative to space and time in finite differences is presented as follows:

$$\frac{QC_{S\,i+1}^{\,j+1} - QC_{S\,i}^{\,j+1}}{\Delta x} + \frac{\left.\frac{QC_S}{V}\right._{i+1}^{j+1} - \left.\frac{QC_S}{V}\right._{i+1}^{j}}{\Delta t} - [e(x,t)]_{i+1}^{j+1} = 0 \tag{3.7}$$

Figure 3-4 presents the conceptual diagram for deducing a solution to the discharge and sediment concentration as a sequential process via adoption of the four-point scheme method. The data on the results are stored and used subsequently to obtain solutions on the sediment concentration in the assigned time step and spatial division, and the background plane represents the approach used for calculation.

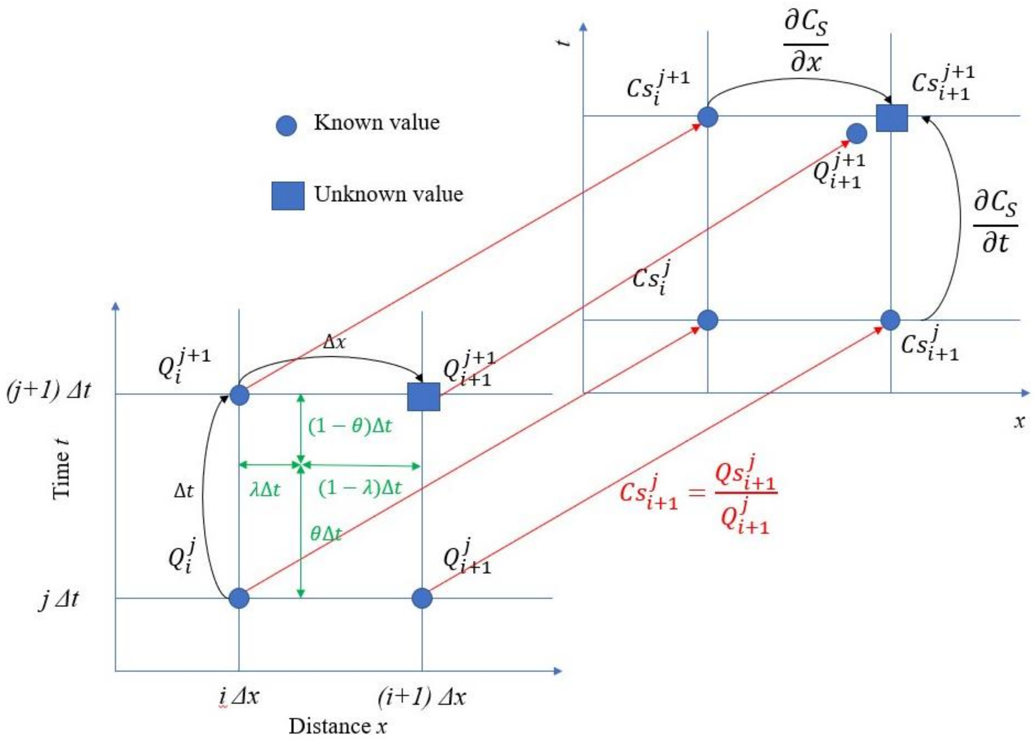

Figure 3-4 Four-point solution model scheme for the parallel sediment concentration calculations.

For slope section $e(x,t) = DF+DR$:

$$\frac{QC_{S\,i+1}^{\;j+1} - QC_{S\,i}^{\;j+1}}{\Delta x} + \frac{\frac{QC_S}{V}{}_{i+1}^{j+1} - \frac{QC_S}{V}{}_{i+1}^{j}}{\Delta t} - [e(x,t)]_{i+1}^{j+1} = 0$$

$$(C_S)_{i+1}^{j+1} = \frac{2\Delta t\Delta x(D_R+\beta_S w v_s T_C)+\Delta t\Delta x\beta_S w v_s {C_S}_{i+1}^{j} + 2\Delta x\left(\frac{Q}{V}\right)_{i+1}^{j}{C_S}_{i+1}^{j}+2\Delta t Q_i^{j+1}Q_i^{j+1}}{\left[2\Delta x(\frac{Q}{V})_{i+1}^{j+1}+2\Delta t Q_{i+1}^{j+1} \ +\Delta t\Delta x\beta_S w v_s\right]} \tag{3.8}$$

For channel section $e(x,t) = DF$:

$$\frac{Q{C_S}_{i+1}^{j+1} - Q{C_S}_{i}^{j+1}}{\Delta x} + \frac{\frac{QC_S}{V}_{i+1}^{j+1} - \frac{QC_S}{V}_{i+1}^{j}}{\Delta t} - [e(x,t)]_{i+1}^{j+1} = 0$$

$$(C_S)_{i+1}^{j+1} = \frac{2\Delta t\Delta x(\beta_S w v_s T_C)-\Delta t\Delta x\beta_S w v_s {C_S}_{i+1}^{j} + 2\Delta x\left(\frac{Q}{V}\right)_{i+1}^{j}{C_S}_{i+1}^{j}+2\Delta t Q_i^{j+1}Q_i^{j+1}}{\left[2\Delta x(\frac{Q}{V})_{i+1}^{j+1}+2\Delta t Q_{i+1}^{j+1} \ +\Delta t\Delta x\beta_S w v_s\right]} \tag{3.9}$$

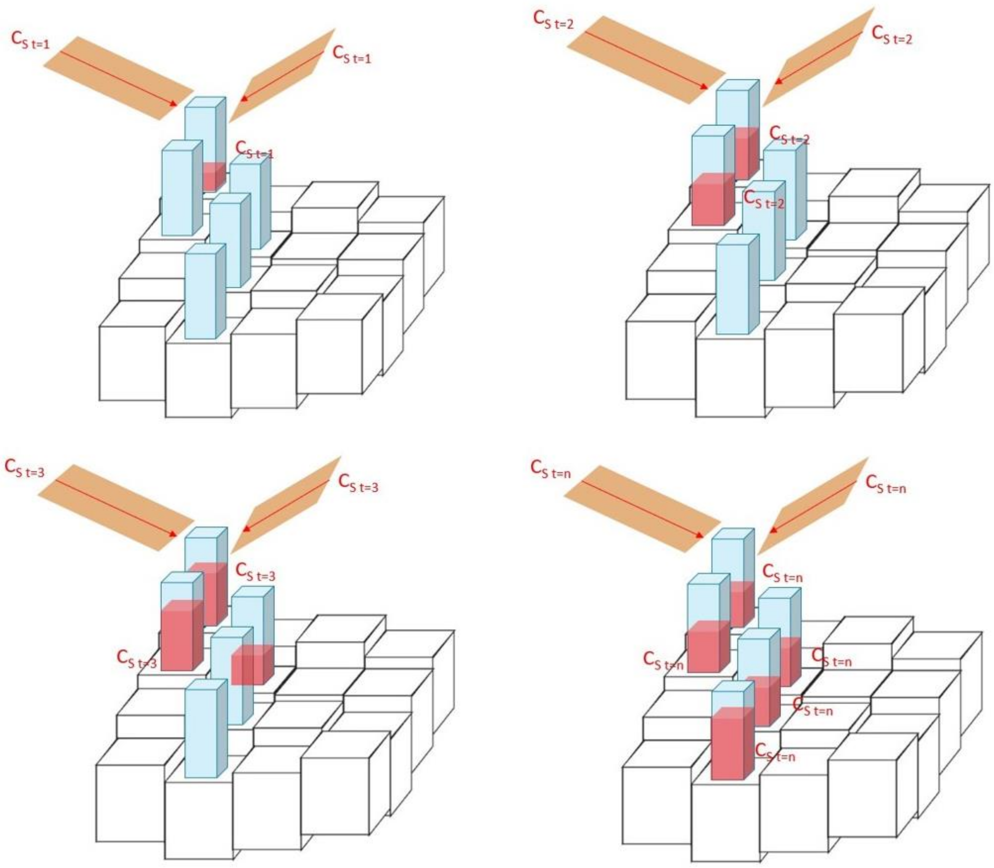

Figure 3-5 Sediment concentration storage for sediment routing process.

Figure 3-5 depicts the schematic process used for sediment routing. After the flow routing is complete, the discharge data stored in the memory of each cell are used for the same time step *dt* and same time division *dt*.

3.5.3 River bed profile evolution

The one-dimensional sediment transport was studied by Dunne (2010) according to the mass balance equation. Transport-limited conditions for this solution approach considers the change in the elevation of the river bed was calculated for every cell identified as a river by applying the Exner equation, whilst the differential grid element elevation was calculated using the sediment flux as follows:

$$\frac{\delta z_b}{\delta t} = -\frac{1}{(1-p_0)}\frac{\delta Q_S}{w \cdot \delta x} \tag{3.10}$$

Here, z_b represents the bed elevation, w represents the unit width of the cell element (m), δx and δt represent the differential time and space elements, Q_S represents the volumetric sediment discharge (m^3 s^{-1}), and p_o represents the soil porosity set at the experimental value 0.43.

3.6 Solution algorithm

First, rainfall-runoff simulations were performed using Eq. (2.1), (2.3), and (2.4). The hydrological model was operated using the parameters presented in **Table 4-2**.

Eq. (3.4), (3.5), and (3.6) were used for deducing the numerical solutions on the sedimentary process, with the initial sediment concentration set to an extremely small value near zero. The soil parameters and equation factors are presented in Table 4-2. *DR* and *DF* were computed for every grid cell involving the hillslope process, whereas only *DF* was computed for river processes as raindrops that did not establish physical contact with the riverbed (**Figure 3-3** and Equation 3.6).

The flowchart in **Figure 3-6** schematically presents the algorithm used for the parallel processing of both the hydrological and the sediment model. For the entire simulation process, the flow rate of the next time step to each cell $Q_{n[i]}$ was calculated using the 4-

point box scheme and data were stored temporarily, after which the stored data were accessed for performing the parallel sediment concentration calculations $C_{S[i]}$, in which i represents a spatial discretization index. These routine calculations were performed for set time steps at the given [i] spatial divisions.

The developed model is based on one-dimensional cell distribution; hence, the direction for flow discharge Q_n and sediment discharge ($Q_S = Q \cdot C_S$) is controlled by considering the flow direction DIR under conditions of application of the eight-direction algorithm (Lehner *et al.*, 2006). The mathematical relations and the program code have been modeled to reproduce the sediment transport processes to the steepest downslope neighbor grid cell. A graphical representation of this drainage process has been depicted in Figure 2-3. The model was coded in C++ language and compiled in a Linux environment.

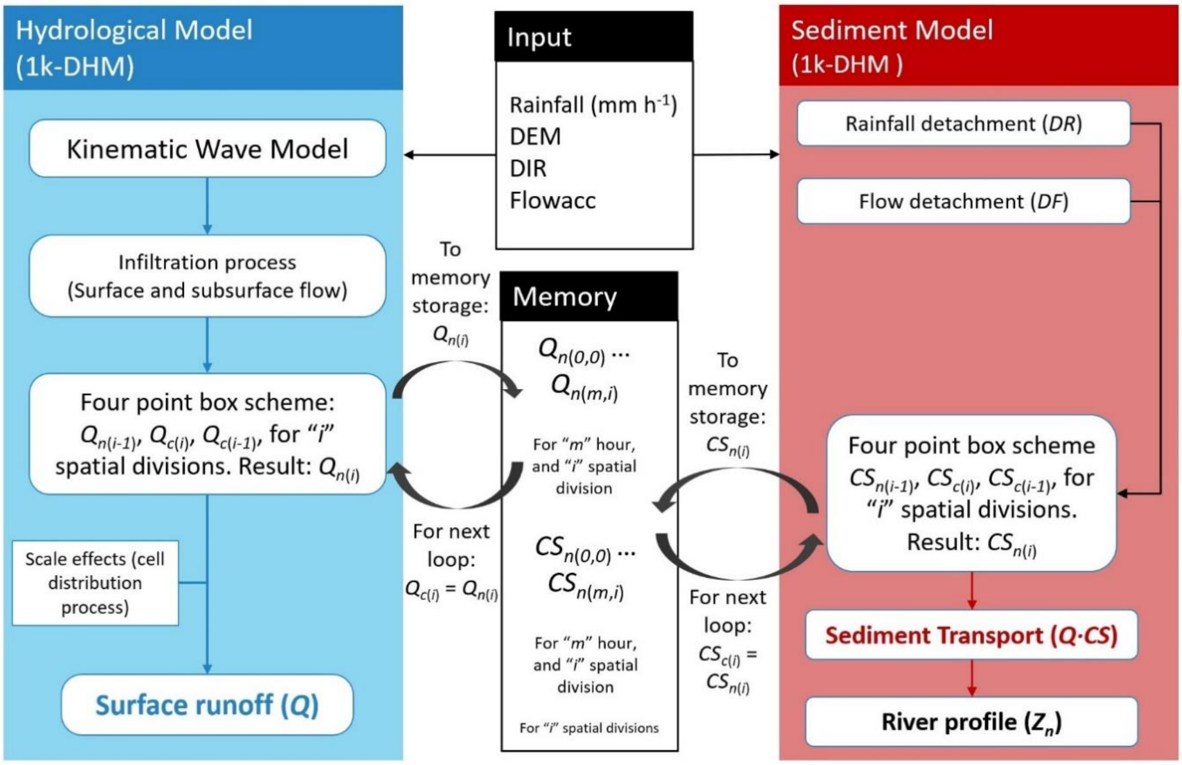

Figure 3-6 Model processes flowchart. The output from the kinematic wave equations being current discharge $Q_{C[i]}$ and next time step discharge $Q_{n[i]}$ are stored in a temporal memory. The subscript [i] denotes the current spatial division, whilst the initial simulation loop i = 0 considers the initial surface water depth by using initial runoff height (mm h^{-1}). Alongside other inputs at the upper box, the sediment model calculates the concentration CS_c and sediment flow Q_C ending the first iteration.

3.7 Chapter conclusion

The main conclusion from this chapter is related to the possibility of processing the results of the sediment concentration by using the same time step and spatial division as those used in the discharge solution based on the use of a the four-point scheme. The process is feasible, and the model can be operated in terms of computing memory space and processing capacity. The importance of input precision and sensitivity analysis in reproducing extreme events has been discussed in the subsequent chapters.

Chapter 4. Application of the sediment routing model to a mountainous basin in Japan and analysis of sediment transport and topographic change

4.1 Introduction

This chapter presents and describes the application of the sediment routing model and the results obtained for the Akatani River basin (**Figure 4-1)**. As briefly described in the previous chapter, the basin was selected for investigation because of the quality of the input data that were kindly shared by MLIT and the detailed sediment reports that were previously published.

The application of the model to the Akatani River basin in Japan is described in Section 4.2, beginning with explanation for the input data used for the sediment routing model. The calibration of the model parameters for rainfall-runoff and sediment production-transport is described in Section 4.3, and the results of the runoff simulations are provided in Section 4.4. Finally, the sediment yield simulations associated with the change in the elevation of the riverbed are described in Sections 4-5, along with an analysis of the change in the riverbed elevation before and after occurrence of the 2017 Northern Kyushu extreme rainfall event. The results of the sediment simulation are analyzed using DEMs with resolutions of 10 m and 100 m (Chero and Tachikawa, 2020). Based on the results of the simulation, the discussion has been presented with emphasis on the sensitivity of the model resolutions to the hydrological and sediment predictions.

4.2 Akatani River input data

The DEM was used to provide a topographical representation of the study basin. The DEM was used as the base topography before performance of the simulation is referred to as “Before (MLIT)” throughout this chapter. After occurrence of the extreme event in July 2017 in the northern Kyushu region, an aerial survey was conducted by the RSRTC, wherein raw data were collected for the Akatani River basin using a laser profiler (LP). A DEM with a spatial resolution of 10 m was generated based on the results of the survey, and the DEM was used as the topographical reference to analyze the results obtained in the present study; this is referred to as "After (MLIT)" in Figure 4-5 and Figure 4-6. The DEM and DIR are shown with a resolution of 10 m in **Figure 4-2** and **Figure 4-3,** respectively. The two digital models provide information about the flow accumulation according to the steepest direction downstream. The digital accumulation grid "flowacc" is used to count the number of connected upstream elements. The element with the highest "flowacc" number was assigned as the basin outlet (P1 in Figure 4-3). The rainfall data that were used for the simulation were obtained using XRAIN with a spatial resolution of 10 m provided by MLIT (Ministry of Land, Infrastructure, Transport and Tourism) and the Transport and Tourism Kyushu Regional Development Bureau in Japan.

The radar rainfall data (XRAIN) that were collected by MLIT were used for performing the rainfall-runoff simulations in the model. The rainfall data collection timeline ranged from 7:00 on July 5th to 23:00 on July 6th, covering a total interval of 40 hours. The maximum rainfall recorded in the catchment was 107 mm h^{-1} on July 5th, which is considered within the extreme rainfall category.

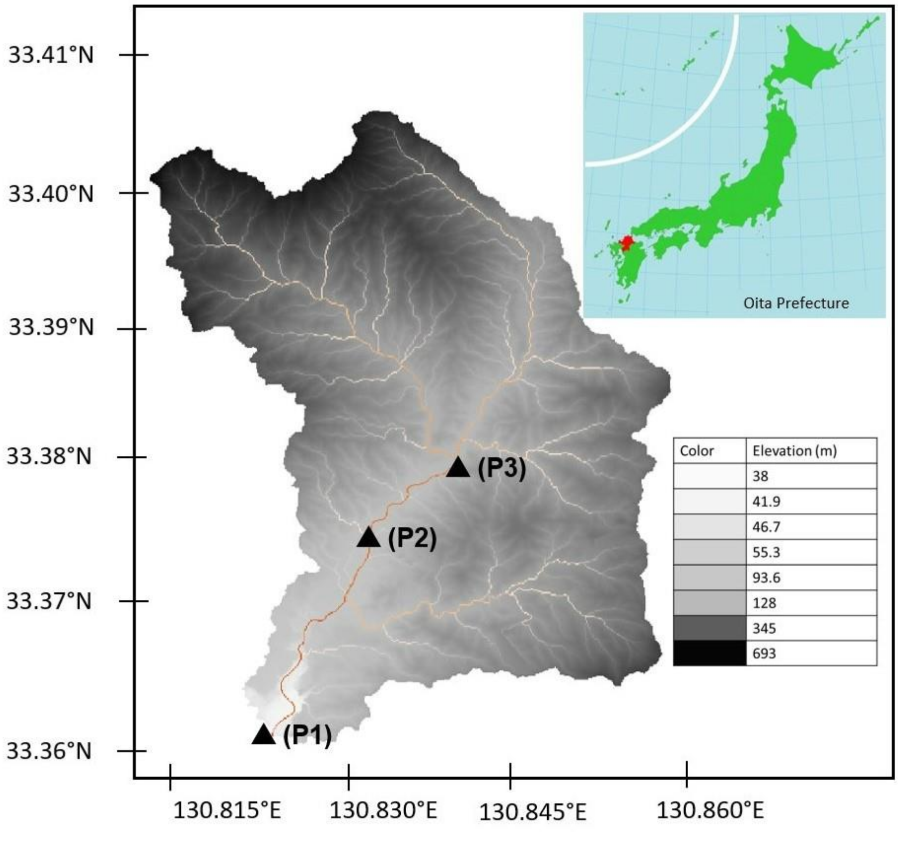

Figure 4-1 Akatani River location.

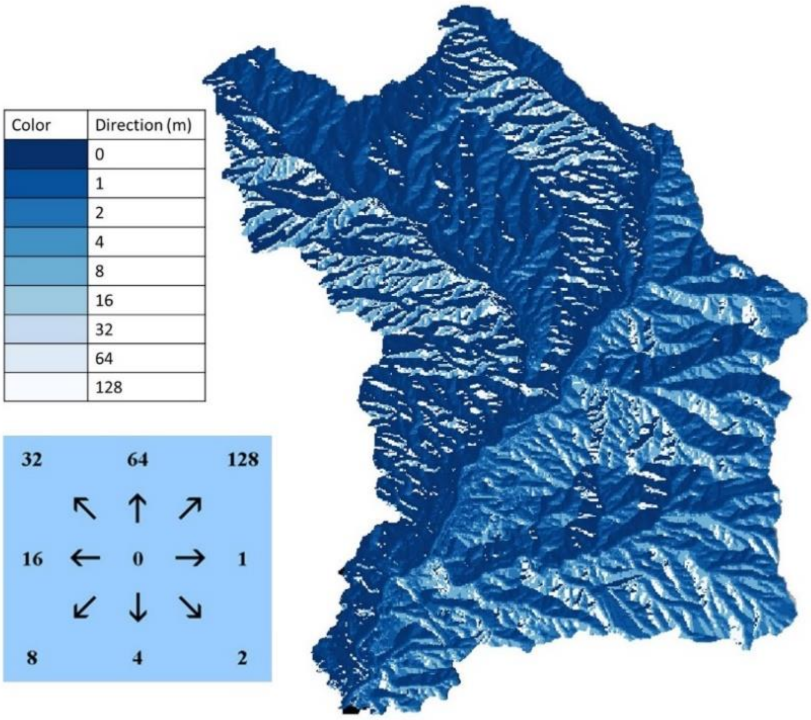

Figure 4-2 Flow drainage model (DIR). Every element was assigned with a flow direction number that will determine the drainage direction in the simulation (DEM data source: MLIT, 2018).

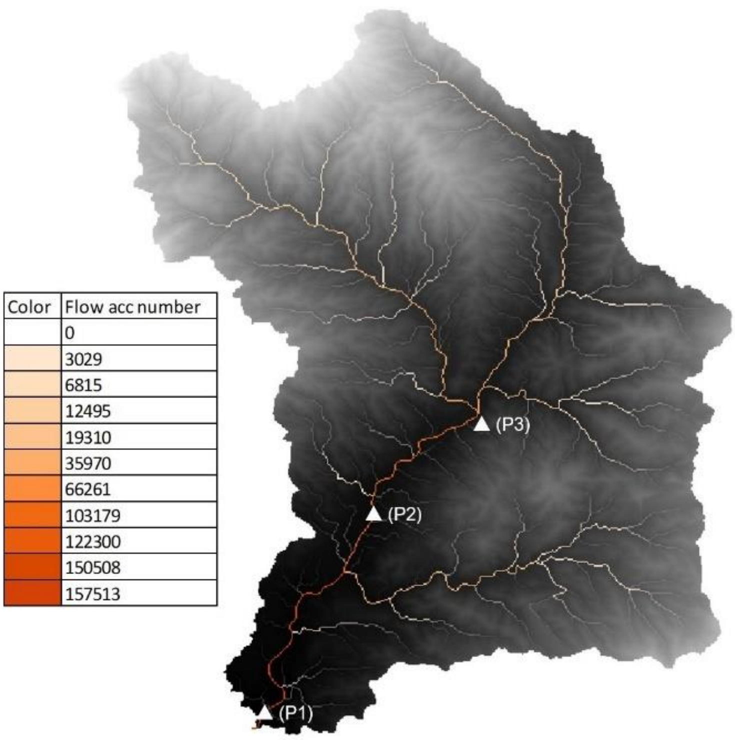

Figure 4-3 Flow accumulation number (flowacc). The number of elements connected from upstream according to the drainage direction DIR. The element with the highest accumulation number was assigned as the basin outlet. The cells with an accumulation number higher than 12,000 were defined as river cells, and the section between P1 and P3 is our sedimentation study area.

4.3 Calibration for the Akatani River simulations

Although the flow at the outlet of the Akatani River basin was not directly gauged, it was determined according to the rational method discharge estimations published by the Chikugo River Committee reports (RSRTC, 2018). The model parameters for the 100-m rainfall-runoff model were initially calibrated using the discharge data obtained at the Kagetsu River basin (Kagetsu parameters, **Table 4-1**) that is adjacent to the Akatani River basin. The initial parameter values were set based on prior knowledge of the model applications, following which the adjusted model parameters at 100-m resolution (identified at the Kagetsu basin) were calibrated by performing trials to the 10-m and 100-m resolution distributed models of Akatani River basin until they fit the estimated hydrograph derived from the RSRTC in terms of the maximum flow discharge and the time at which peak flow occurred. Calibration involved changing the roughness coefficients (slope and channel) to the time to peak, following which data on the depth of soil of the capillary and the hydraulic conductivity were fine-tuned to match the peak discharge. The parameters that are related to rainfall-runoff processes, such as hydraulic conductivity, soil depth, and roughness coefficients, are summarized in the following table:

Table 4-1. Hydrological model parameters including Manning coefficients, and depth of soil layers for groundwater simulations. Time step and spatial division account for convergence in simulations.

Parameter	Unit	Calibrated		Kagetsu River
Resolution	m	100	10	100
Manning coefficient for river	—	0.015	0.095	0.005
Manning coefficient for slope	—	0.185	0.085	0.15
Hydraulic conductivity	$m\ s^{-1}$	0.56×10^{-3}	0.46×10^{-4}	4.56×10^{-4}
Depth of capillary and non-capillary soil layers	m	0.084	0.084	0.73
Depth of capillary soil layers	m	0.027	0.078	0.71
Beta coefficient	—	6.35	6.35	6.35
Time step	s	600	6	600
Number of spatial divisions	—	20	20	20

Table 4-2. Sediment model parameters. Particle size, settling velocity, and conductivity are based on average values for mountain regions in Fukuoka. Detachability and stream power are based on empirical values according to Morgan et al. (1998).

Symbol	Parameter	Value	Unit
Z	Soil Texture	3.5	—
CS	Initial sediment concentration	5 x 10^5	m^3 m^{-3}
ρ_s	Soil Density	2650	kg m^{-3}
β_S	Correction factor to calculate cohesive soil erosion	0.5	—
υ_s	Particle settling velocity	0.005	m s^{-1}
k_{sd}	Index of soil detachability	0.09	g J^{-1}
ω_{cr}	Critical value of stream power	0.4	m s^{-1}
d_{50}	Median particle size	250	μm

4.4 Application of the sediment routing model to the Akatani River basin

Figure 4-4 shows the predicted discharge hydrographs for the extreme rainfall event using the 10-m and 100-m resolution rainfall-runoff models and the hydrograph generated by the RSRTC (2018) using the synthetic rational method. The maximum rainfall intensity during occurrence of the flood event was more than 100 mm h^{-1} and the catchment size was 21 km^2. Under these conditions, the estimated hydrograph that was generated by the RSRCT using the rational method represented by the dotted line is considered reasonable.

The simulations for 10-m and 100-m resolutions provide similar runoff results overall. The peak river discharge hydrograph at outlet (P1) of the Akatani River was estimated to be 480 m^3 s^{-1} using the developed model, while the discharge based on the RSRTC was determined to be 520 m^3 s^{-1}. The hydrologic features were similar in terms of the time at which the peak occurred and the peak discharge. However, this model includes the subsurface flow with the consequence that the recession limb will be gentler. This is observed in the hydrographs at both resolutions.

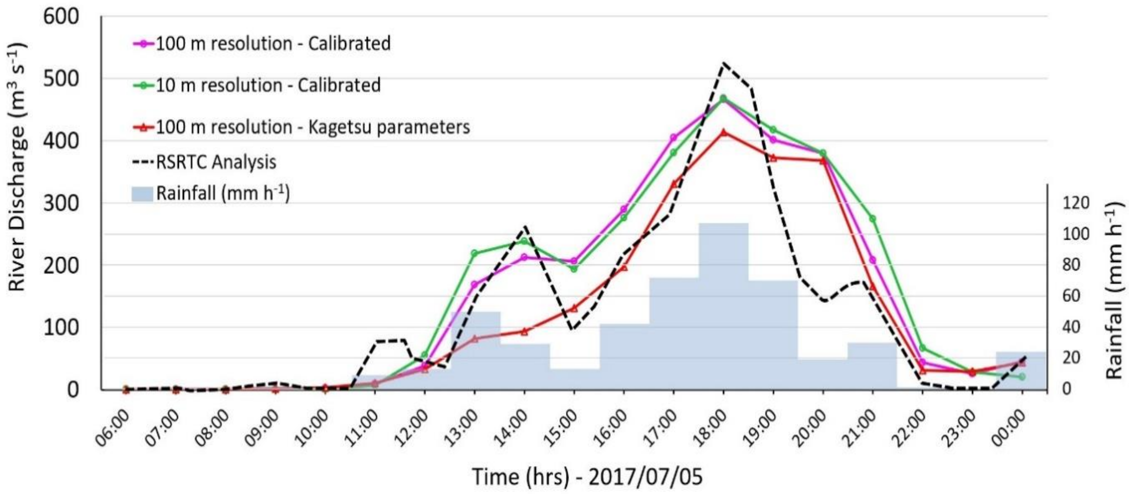

Figure 4-4 River flow hydrographs simulations for the outlet (P1) of the Akatani River basin (at 10 m and 100 m spatial resolutions) compared to the synthesized rational method estimated by RSRTC (July 5th, 2017).

4.5 Sediment transport results

The use of high-resolution DEM and DIR enabled higher convergence in the results obtained for the transport of sediment and sedimentation. It is also noticeable that the model is sensitive to the spatial resolution. The peak sediment concentration is 0.061, 0.695, and 0.080 at control points P1, P2, and P3, respectively. Cells for the river in the lower or middle basin are expected to contain higher volumetric concentrations and the highest sediment transport rate in m^3.

The highest intensity (mm h^{-1}) of distributed rainfall is observed in the upper catchment; thus, the C_S will surge due to D_R and reach its peak value at the upper or middle basin before or during peak rainfall. This is according to the principles of a physical process in which the outflow from the sub-basin enters the river system. The peak value in this simulation occurred at point (P2), as illustrated in Figure 4-3, at 18:00 h on July 5th. According to Eq.(3.6), the sediment concentration is expected to follow a similar pattern to rainfall intensity if the depth of the runoff is close to zero; beyond this, it is exponentially reduced by the right-hand side expression e^{-Zh}, where h represents the depth of the water on the surface. Following the initial stage, the total erosion process $e(x,t)$ derived from Eq.(3.4) is controlled by detachment via the flow and the sediment continuity Eq.(3.3). Finally, after completion of a rainfall-runoff cycle and after the water depth h at the slopes returns to the minimum value, a new rainfall event can trigger sediment production as depicted in the final hours illustrated in **Figure 4-5a**. It is verified that *DR* and *DF* operate accordingly at separate threads, after which the full integration of the sediment is completed according to the expression in Eq.(3.3).

The simulated main river profile was generated by considering the reference from the original bed elevation “Before (MLIT)” DEM. The change in the bed elevation for every differential element is in accordance with the Exner relations. For instance, **Figure 4-5b** shows the elevation relationship at the three selected points (P1, P2, and P3) over time where the level change is stable after 20:00 h on the first day. To generate the profile for the full river extension, the same algorithm was used for every element to determine the final elevation profile shown in **Figure 4-6**. In the figure, the simulated river elevation profile has been compared to the laser profiler topography “After (MLIT)” that was generated by the RSRTC. The bed profile of the downstream river provides evidential support to the expected aggradation trend.

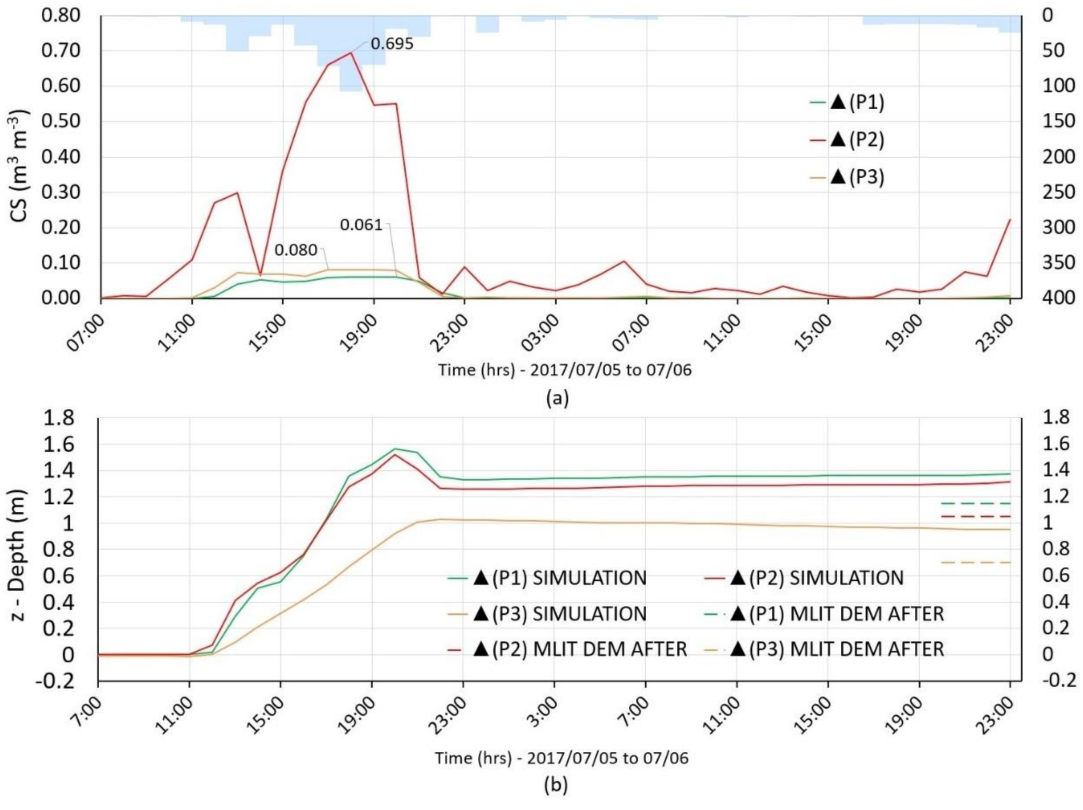

Figure 4-5 Simulation results from Figure 4-3 analysis points: outlet (P1), critical point for maximum concentration (P2), and the junction point where the upper tributaries merge with the main river (P3). (a) Sediment concentration results. (b) Bed elevation change for the first 40 hours.

The high-resolution DEM river model and sediment discharge allows for the one-dimensional simulation of the riverbed elevation over time (July 5th to 6th, 2017).

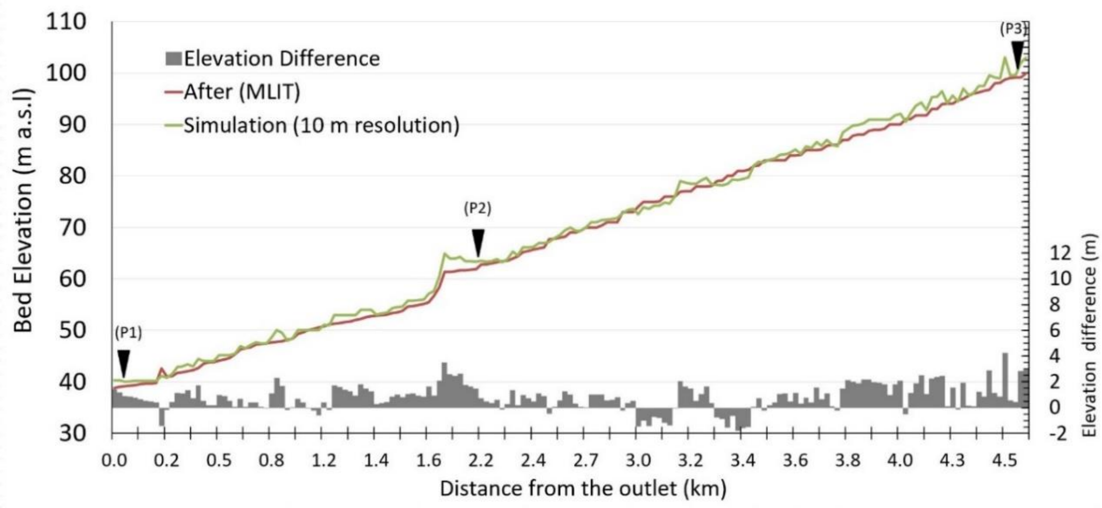

Figure 4-6 River Bed profile comparison River bed profile elevation comparison (m a.s.l.). Results presented here belong to the 48th hour of simulations. The expected result, according to the RSRTC survey, is a net river aggradation.

To offer a more profound understanding of the results, a comparative sediment transport balance based on the simulations performed at 10 m and 100 m and the RSRTC LP-processed data have been summarized in **Figure 4-8** and **Table 4-3**. The figure indicates that the simulations are sensitive to the DEM resolution. The 10-m resolution results show sediment transport rates that are closer to the upstream Otsushi and the mid Akatani basins. The estimated sediment transport using the 100-m resolution model is lower in comparison.

Consequently, the developed model can be used to reproduce the sediment transport and change of topography using spatially distributed rainfall at the upper catchment, steep basin topography, and soil parameters that are set based on the unconsolidated mountain region. The critical sediment deposit was suggested to be located at the Akatani River middle basin according to Figure 4-8 and the profile estimation according to the results in Figure 4-6. The sediment transport balance at both resolutions after occurrence of the event and comparisons with the RSRTC Report are provided in Table 4-3.

Table 4-3. Sediment transport comparison between RSRTC and simulations at 10 m and 100 m resolutions.

Basin Name	Sediment Transport (RSRTC Report)	Sediment Transport (Simulation - 10 m Resolution)	Sediment Transport (Simulation - 100 m Resolution)
	Vol (10^4 m^3)	Vol (10^4 m^3)	Vol (10^4 m^3)
Akatani Upper	12.00	13.87	12.90
Otsushi	85.00	30.65	21.10
Oguchi	4.00	7.88	6.31
Akatani Middle	90.00	52.21	47.47
Oyama	0.00	8.94	8.31
Akatani Lower (Outlet)	68.00	58.21	56.81

4.6 Chapter conclusion

The use of a flow discharge and sediment transport parallel model is an effective approach to simulate erosion/deposition for hillslopes and rivers. It could be used to reproduce field data collected before and after the occurrence of an event according to the physical processes involved. Figure 4-6 supports these results. The developed model shows an improvement in the sediment simulations when a 10-m resolution DEM was considered. Compared to the results obtained at lower resolutions, the slope represented by using the developed 10-m resolution model enabled higher spatial divisions, and thus resulted in higher convergence. Furthermore, the model aids the estimation of a sediment budget, which can be used to describe the volume of sand that has been subjected to erosion from or deposition on the riverbed. **Figure 4-5, 4-6, 4-7,** and **4-8** provide an understanding of the manner in which the main river section downstream underwent the most considerable extent of accretion and the manner in which the upstream basin underwent the most substantial extent of erosion.

The theoretical assumption adopted to simulate the sediment production on the slopes corresponded to the real physical process, in which the sediment production rate declined gradually after the peak discharge was reached (Figure 4-5a).

One limitation of the developed model is that it cannot be used to account for the river processes that are associated with sedimentary particles of large diameter such as boulders on the riverbed. Another consideration is that the flow direction (DIR) information is processed before the conduction of simulation, rendering the drainage path constant throughout the simulation and restricting the model to a one-dimensional change after the achievement of sediment yield. This is the underlying reason for recommending the application of the kinematic wave equation for steep basins in which the drainage path remains constant over time.

In summary, it is necessary to collect more data both before and after the occurrence of sediment-related disasters to improve the simulation of physical processes, especially in terms of the location of critical sediment deposits or erosive areas.

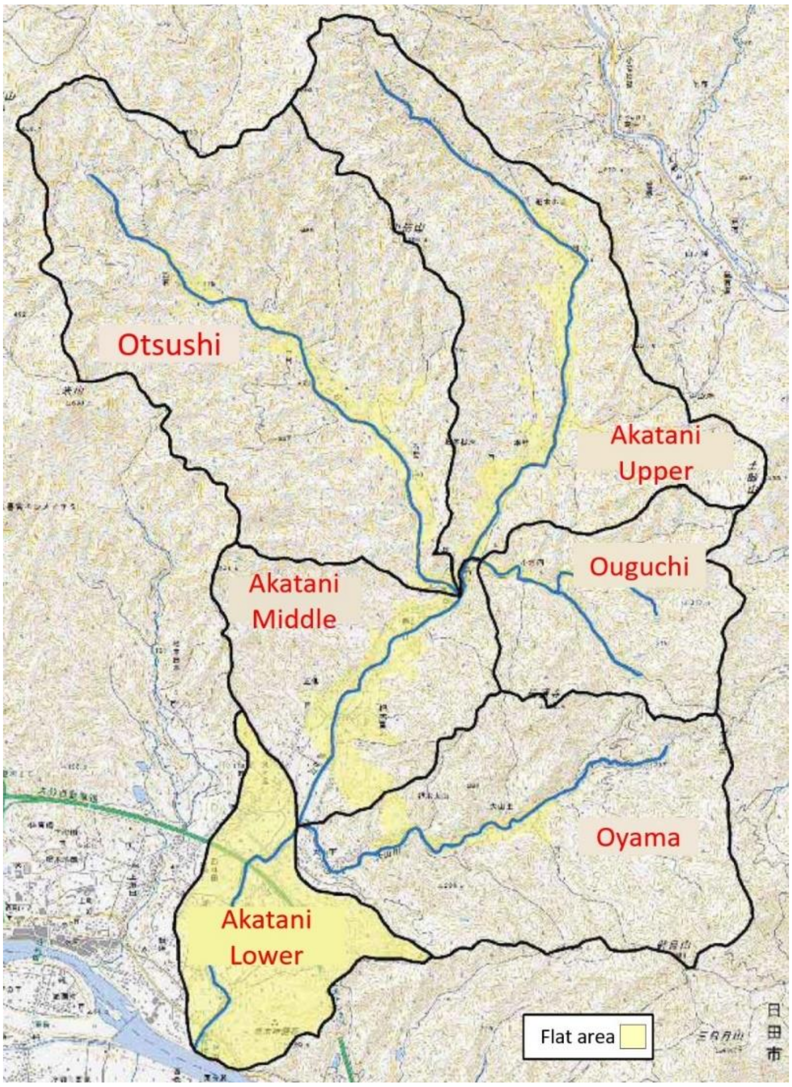

Figure 4-7 Sub basin identification and location of flat land (Source: RSRTC 2018 Report).

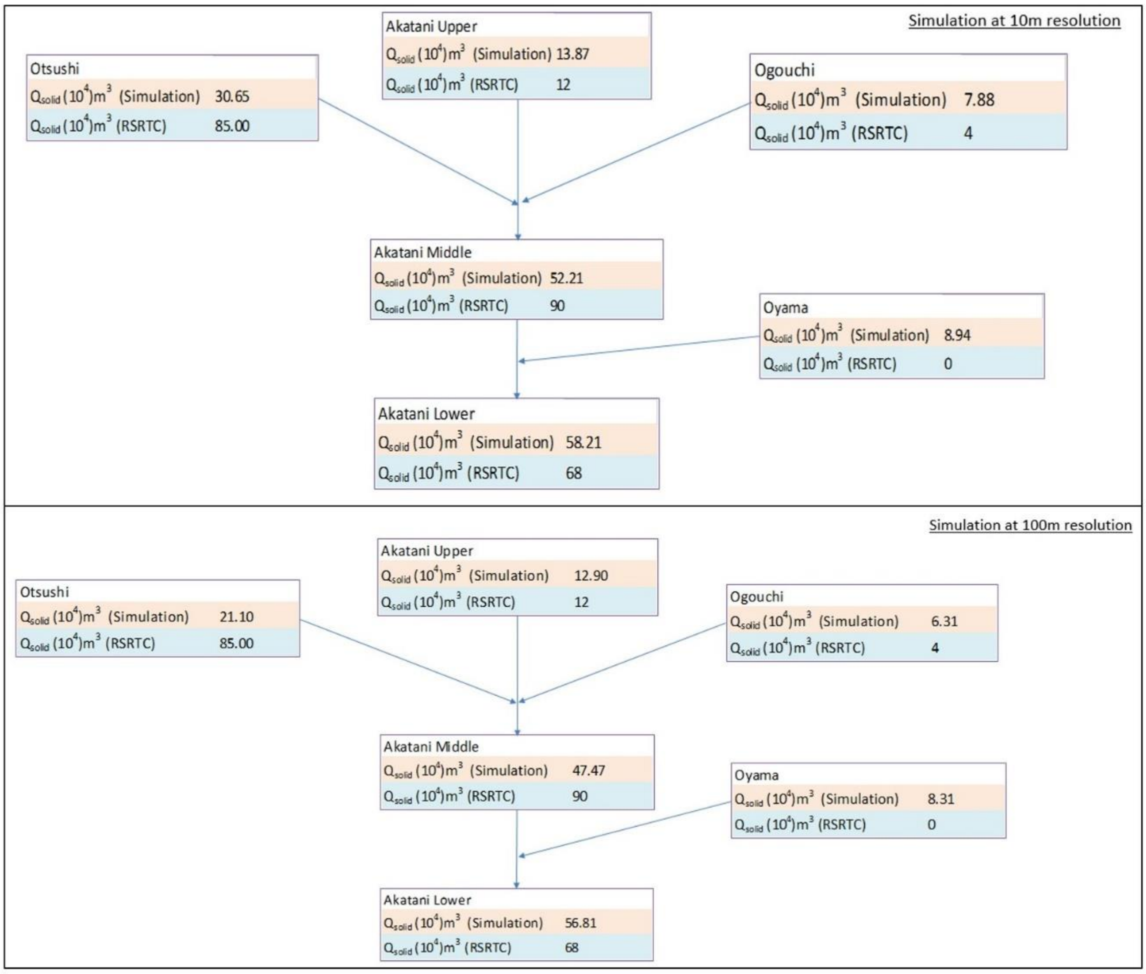

Figure 4-8 Sediment transport calculations after the event for 10 m and 100 m resolutions.

(This page intentionally left blank)

Chapter 5. Application of the sediment routing model to a mountainous basin in Peru and analysis of the interaction between rainfall-runoff and sediment transport

5.1 Introduction

Studies involving sedimentology and hydrological predictions in the northern coast of Peru are constrained by the availability of distributed rainfall data and gauging stations at key observation points. Most basins are ungauged. The development of a spatially distributed integrated hydrological and sediment model is a promising approach with which hydrologic and sediment predictions can be performed for ungauged basins. The dependence of the hydrological-sediment models on topographic resolution is a critical issue for identifying the uncertainty in the structure of a model and its parameters. This chapter addresses parameter uncertainty in terms of DEM resolution.

The numerical simulations performed using hydrological-sediment models depend on accurate rainfall data, accurate topographic representation, and descriptive soil parameters. Considering the transport mechanism for highly erosive and steep rivers, our model was developed based on the approach put forth by Egashira & Matsuki (2000) which enabled the provision of solutions for sediment transport in a complex channel network. The aforementioned model is considered relevant given the satisfactory results for sediment simulations in steep Japanese rivers. Hence, an extended fully distributed rainfall-runoff and sediment transport model was designed by Chero & Tachikawa (2020). The main challenge of this study was to analyze the dependence of a model on the topographic resolution and the identification of parameters for a highly erosive Peruvian basin located on the northern Pacific Coast.

The study area and its hydrological features are introduced in Section 5.2. A brief description of the integrated model assumptions that are used to perform adaptations of the sediment simulations to the Tumbes River is provided in Section 5.3. The results and discussion of the rainfall-runoff and sediment model output are presented in Section 5.4. Analysis of the parameters and the model output sensitivity according to topography resolution settings are discussed in Section 5.5. Results on the model and the implications of sensitivity analysis for multi-annual simulations in the final chapters are presented in the conclusion.

5.2 Application of sediment routing model in Tumbes River basin in Peru

The Tumbes River, which is illustrated in **Figure 5-1**, is located on the northern coast of Peru. The upper catchment is located in the Andes Mountain at an average elevation of 2000 m.a.sl. This basin is considered ungauged as the catchment has only two automatic hydrological gauging stations and three automatic rain gauging stations that are currently in operation, covering a total area of 5200 km^2. A floodplain, or an alluvial plain with extensive sediment deposits, has reportedly formed near Tumbes City, which is a consequence of the continuous transport of sediments.

The “El Niño Southern Oscillation” (ENSO) events occurring during the rainy seasons of 1982–83 and 1997–98 were recorded as disaster category events. The flooding of paddy fields, disruption to farming, and economic losses pertaining to tourism were the main aftermaths of the floods. Erosion and sedimentation extended the effects of flooding, and thus it was acknowledged by the scientific community that the presence of the ENSO depended on the development of an emergency protection protocol in terms of the infrastructure in this area.

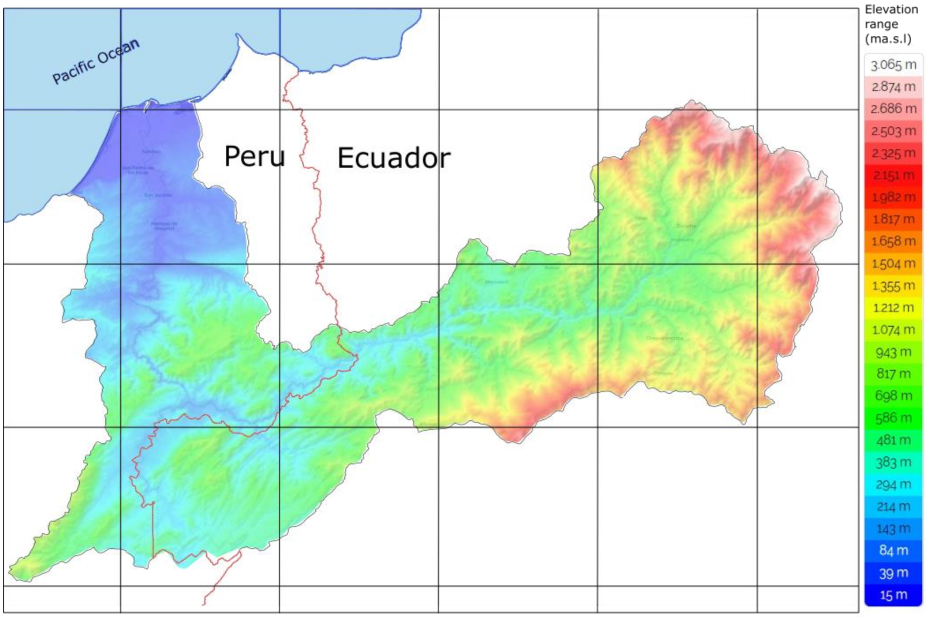

Figure 5-1 Tumbes River Location and elevation range.

Regardless of the occurrence of ENSO events, the transport and erosion of sediments are recorded every year. Frequent floods are recorded in the rainy season (January to May). Predictability of the sediment volume flux is necessary to conduct dredging and to confer protection to the rivers from embankment failure and to counter subsequent flood-associated damage in Tumbes City. Thus, the purpose of this study was to reproduce the physical processes in which the runoff and sediments could be flushed from the upstream areas to the lower elevation areas.

5.3 Description of the model for application in Tumbes River

To complete the development of the model for larger basins, the model input, code scaling factor according to the DEM resolution, and the resolution used for the rainfall input were subjected to verification. The integrated hydrological and sediment model kinematic wave equations presented in Chapters 2 and 3 were used. The test provided satisfactory results and data on the appropriate hydrological and soil parameters were obtained that have been discussed in the remaining parts of this section.

5.3.1 Distributed rainfall and topography data

The input rainfall data were recorded at three meteorological stations, namely two in Ecuador at the upper part of the basin and one in Peru at the outlet of the basin. The monthly gauged rainfall data obtained from the Ecuador Meteorological Service (INAMHI) and the Peruvian Meteorological Service (SENAMHI) were used to perform calibration of the spatially distributed rainfall data obtained from Global Satellite Mapping of Precipitation (GSMaP) time series. A monthly bias correction was performed to the GSMaP time series data to generate the hourly rainfall input series.

The other inputs used in the model were the DEM (Digital Elevation Model) and DIR (Flow DIRection, digital drainage model directing flow to the steepest down-slope neighbor cell) at 500-m and 1000-m resolutions whose data were extracted from the USGS Hydrosheds database (**Figure 5-2**). The steep slope at the upper and middle catchment were reproduced by using a DEM with a resolution of 1000 m; however, the higher resolution 500-m DEM enabled data on the slopes to be processed with higher accuracy in every grid cell, as discussed in Section 5.5.

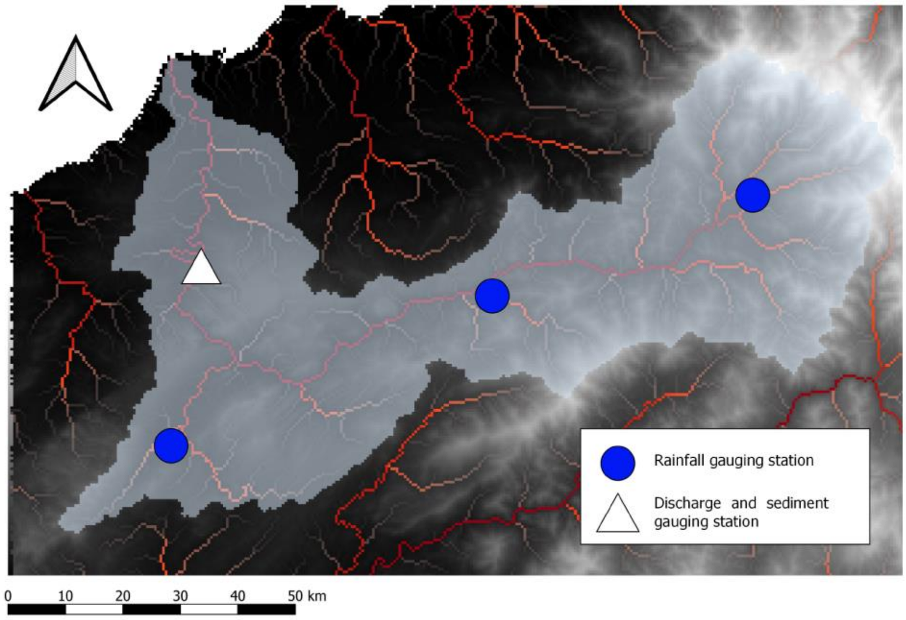

Figure 5-2 DEM and the *flow accumulation number* cells that outlines the reach of the river process. The location of the three rain gauges and the discharge station in the study area are displayed.

5.3.2 Sediment generation modeling for Tumbes River

The soil detachment attributable to the raindrop impact *DR* is an erosional process in hillslope simulations. Related laboratory experiments have demonstrated the mechanisms by which the momentum of a raindrop falling on the hillslope surface can lead to erosion. One of the effects of rainfall is the initial compacting of the soil surface, illustrated in **Figure 5-3**. Another effect, and the main source of the sediment production, is related to raindrops which possess sufficient kinetic energy that is used to detach particles of soil from the surface (Poesen & Govers, 1986).

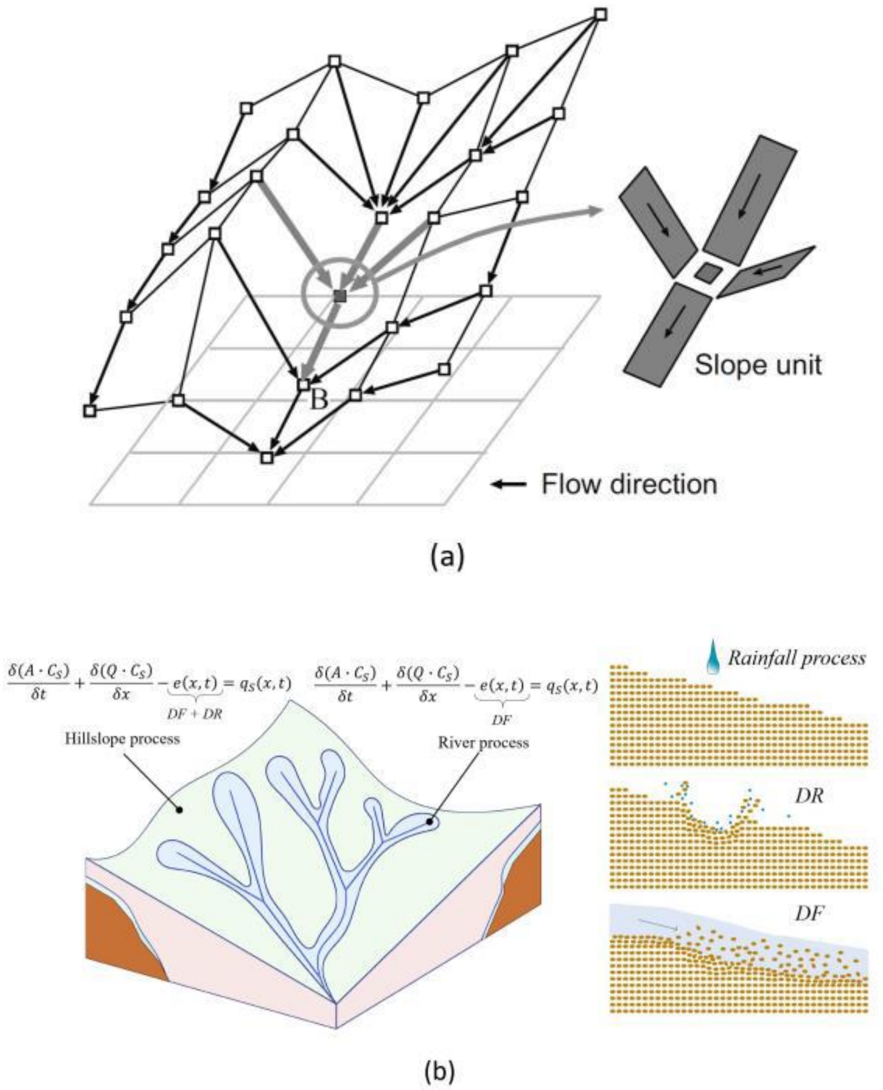

Figure 5-3 Hydrological model DEM grid slope unit representation. The erosion process at slopes includes DR and DF, whereas river process is controlled by DF.

The relationships proposed in Section 3.5 were considered for investigation of Akatani River (Japan) with satisfactory results. The model was thus adopted under the same relationship conditions for application with Tumbes River; however, it could be acknowledged that some soil parameters would vary according to the calibration and scale used (modeling for Tumbes River was performed using DEM and DIR at a 1-km resolution).

Emphasis is laid on Eqs. 3.5 and 3.6 expressed in the following manner:

$$DR = \left(\frac{k_{sd}}{\rho_S}\right) KE \cdot e^{-Zh}$$

Here, k_{SD} represents the soil detachment index that ranges from 0.01 to 10 kg·j^{-1} according to the soil texture and shear strength, $KE = 8.95 + \log(r)$, ρ_s represents the soil density, e^{-Zh} represents a correction factor that reduces the capacity of the raindrop impact to produce sediment, h represents the depth of the surface runoff, and Z represents the soil texture that ranges from 0.9 to 3.1. Raindrop detachment is reduced when surface flow occurs, and a significant surface flow depth prevents soil detachment due to a reduction in the impact made by raindrops, which is numerically represented by the reduction factor (e^{-Zh}).

The effect of rill erosion was studied by Dunne & Aubry (1986). Laboratory and field observations were performed wherein water was allowed to flow over the land or a surface was subjected to artificial rainfall at different intensities that reached rates of 140 mm h^{-1}. The conclusions deduced were that raindrops did not produce rills, which were only generated as a result of sediment transport, while surface runoff led to transport and the formation of rills only near the lower part of the prototype slope. Rainfall at a rate of 140 mm h^{-1} was considered for comparison, and resulted in the removal of rills and sediment transport. These experiments indicate that the rainfall intensity in extreme events possesses sufficient kinetic energy to flatten rills, rendering uniformity to the surface overall.

5.4 Rainfall-runoff and sediment simulation results

5.4.1 Rainfall-runoff simulation results

The hydrological model optimization for 500-m and 1000-m resolution models was conducted by performing auto-calibration with the SCE-UA (shuffled complex evolution method) that was developed at The University of Arizona. The target result is the obtainment of information on the daily average recorded discharge. After a calibrated result was obtained, the sensitivity of the roughness coefficients was analyzed to avoid an erroneous equifinality. It was found that a considerable range of roughness coefficient combinations could be used to reproduce the observed hydrograph, thus indicating that the roughness that was used for the 1000-m resolution model could also be used for the 500-m resolution model. The final set of hydrological parameters has been summarized in **Table 5-1**, and the parameters were maintained constant to analyze the sensitivity of the sediment simulations.

Table 5-1 Hydrological parameters for each resolution.

Parameter	1000 m model	500 m model
Manning coefficient (river)	0.03	0.03
Manning coefficient (slope)	0.09	0.09
Hydraulic conductivity (m s^{-1})	0.016	0.0026
Depth of capillary and non-capillary soil layers (m)	1.80	0.80
Depth of capillary soil layers (m)	1.40	0.70
Beta coefficient	6.5	6.5
Time step (s)	600	600
Number of spatial divisions	20	20

The hydrological simulations are summarized in **Figure 5-4**. Considering that measurement was sparse in the catchment, the hydrological parameters were identified in terms of the time of peak flow and the maximum discharge with an acceptable accuracy at both resolutions. Analysis of the hydrograph indicated a slight overestimation in the recession limb in both models, which could be attributed to real conditions such as accelerated evapotranspiration and/or infiltration processes in the dry period that could be observed in the Andes.

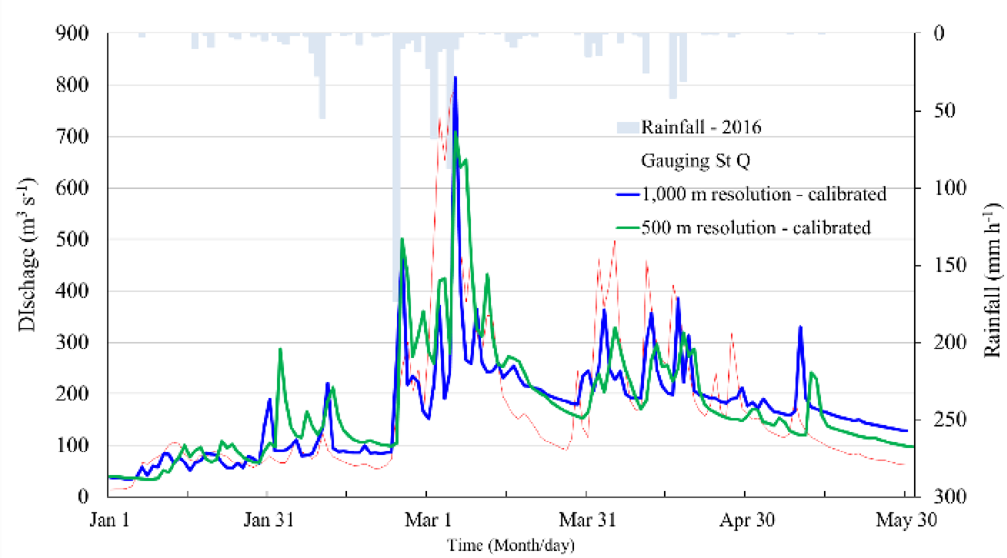

Figure 5-4 2016 rainy season hydrological simulations by 500 m and 1,000 m model.

5.4.2 Sediment simulation results

For the models established at 500-m and 1000-m resolution, an auto-calibration using SCE-UA was performed using the daily and monthly average sediment concentrations as the target results. The optimized parameters were obtained according to each topographic scale and were considered the baseline for the sensitivity analysis discussed in the next section (refer to **Table 5-2**).

Table 5-2 Sediment model parameter baseline for each resolution.

	Parameter	500 m	1000 m	Units
Z	Soil Texture	2.0	1.0	–
CS	Initial sediment concentration	5 x 10^5	5 x 10^5	$m^3\ m^{-3}$
ρ_s	Soil Density	2650	2650	$kg\ m^{-3}$
β_S	Correction factor to calculate cohesive soil erosion	0.0065	0.65	–
υ_s	Particle settling velocity	0.005	0.0005	$m\ s^{-1}$
k_{sd}	Index of soil detachability	0.01	0.5	$g\ J^{-1}$
ω_{cr}	Critical value of stream power	0.4	0.4	$m\ s^{-1}$
d_{50}	Median particle size	250	250	µm

To assess the performance of the sediment generation, the relationship between discharge and sediment concentration obtained by Morera et al. (2017) was considered. Statistical analysis was performed based on historical data collected between 2004 and 2013 to describe the transport of the sediment in the study basin. The results are summarized in **Figure 5-5**. The highest precipitation was recorded from January to April, during which the highest rate of sediment generation was attributable to raindrop detachment and high flow. From April onward, an inward declining trend was observed as the rainfall intensity decreased, thus resulting in the achievement of lower sediment rates.

According to Figure 5-5, the 1000-m resolution simulation for the year 2016 conducted in this study revealed that the monthly average sediment concentration against the monthly average discharge fit hysteresis loop behavior in the same manner as the trend observed in the historical time series. **Figure 5-6** shows the sediment concentrations at the outlet for both models, which satisfactorily match the historical monthly average concentration in terms of the time at which peak flow occurred, the rising limb, and the behavior when rainfall ceased for a few days.

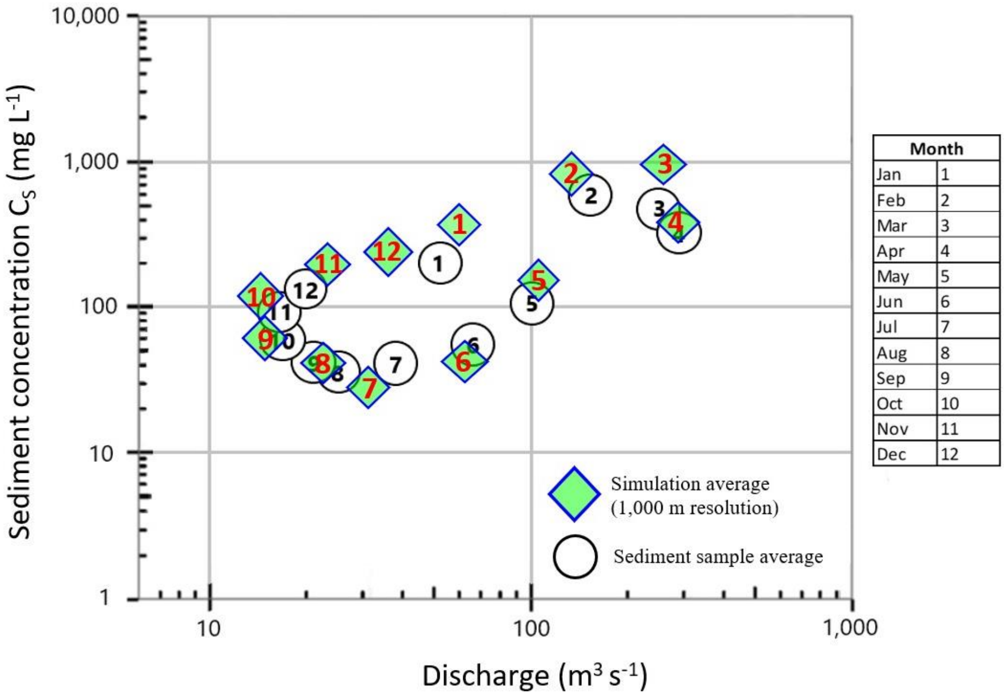

Figure 5-5 Log-log correlation between monthly mean discharge (m^3.s^{-1}) and monthly mean suspended sediment (mg.L^{-1}). The 1,000 m resolution 1KDHM monthly average simulation results are displayed in the green diamond markers and well fit to the observed data from processed by Morera (2014) and published by the IGP in the white circle markers.

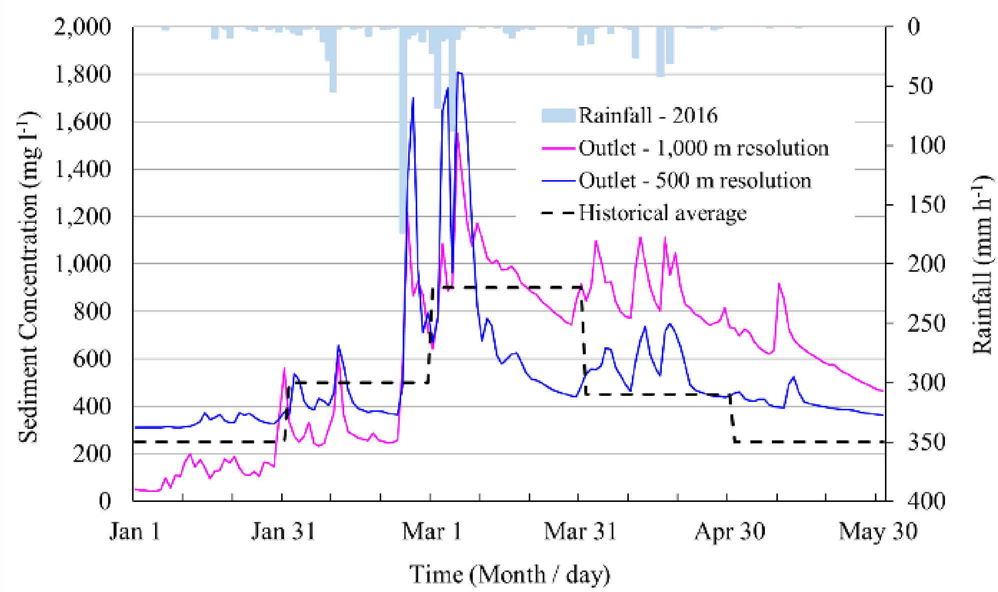

Figure 5-6 Sediment concentration (mg.L^{-1}) at 500 m and 1,000 m resolution model baseline. The sediment samples were taken at the same location as the discharge gauging station.

The outlet will receive the highest C_S (1,500 to 2,000 mg.L^{-1}) that is classified as suspended sediment at high concentrations. A consistent pattern in the C_S is observed, considering that detachment by flow and raindrops is present throughout the rainy season. Downscaling to a 500-m elevation and the flow direction data enables calculation of the slope effect for soil detachment with higher precision for every differential element. It is possible to confirm this when the rising limb for January and February and a steeper sediment flush (recession) in the month of March and April are observed.

5.5 Sensitivity analysis of model resolution using an integrated model

Through the performance of a wide range of model simulations at resolutions of 500 m and 1000 m, it was possible to quantify the sensitivity of the model sediment parameters to the downscaling of the topographic resolution. By using the one-at-a-time approach, variation in the output was examined by setting the parameters from the maximum to the minimum physically possible range. Historical suspended sediment yield (SSY in t.km^{-2}.y^{-1}) data recorded by the Peruvian Geophysical Institute (Morera, 2014) was used to determine the optimum range of sediment parameters. The historical SSY plot in the northern coast is presented in **Figure 5-7.** The annual sediment transport in the Tumbes River basin ranges from 341 to 556 t.km^{-2}.y^{-1}. This range is plotted using a yellow bar in **Figure 5-8** for every parameter at the respective resolution.

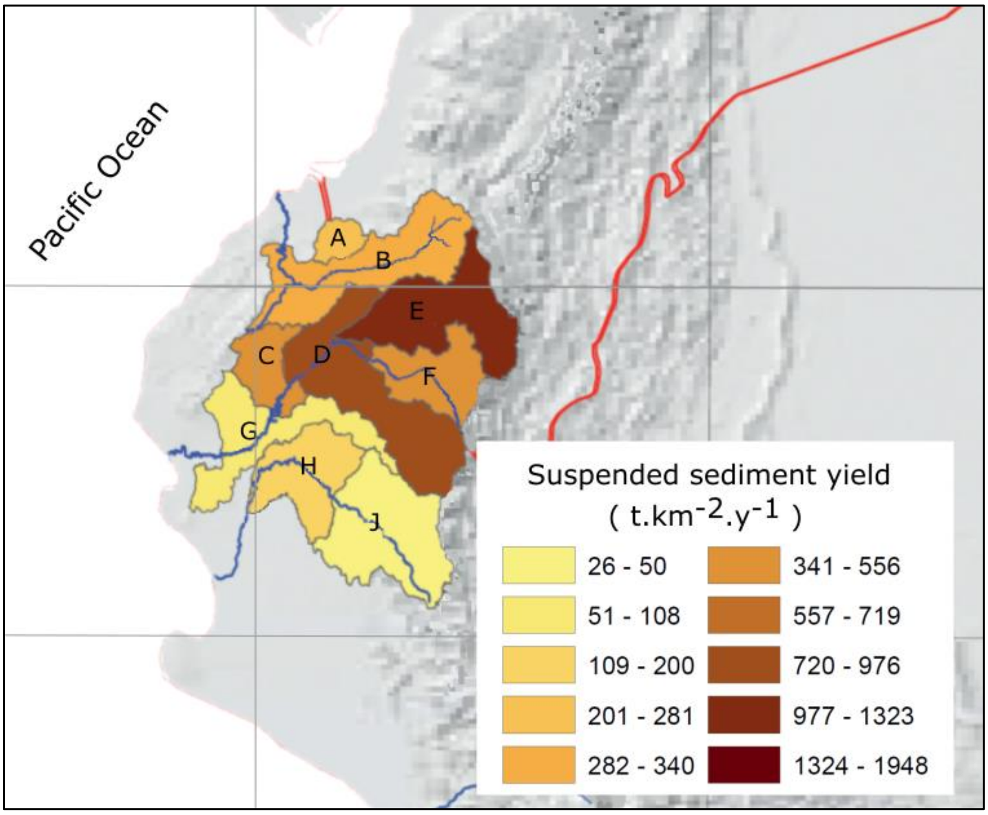

Figure 5-7 Suspended sediment yield ($t.km^{-2}.y^{-1}$) at the northern coast of Peru from long-term series. For Tumbes River (Basin B) the expected sediment yield after a rainy season is in the range of 341 to 556 $t.km^{-2}.y^{-1}$. Suspended sediment yield estimations were published by Morera (2014).

For a 1,000-m resolution, the most noticeable tendency was attributable to the particle diameter d_{50} and the settling velocity v_s, which collectively led to a higher divergence in the results. A smaller settling velocity (related to the sediment suspension) will produce a substantial increase in the sediment yield. Regarding the particle diameter, an inverse relationship could also be observed; thus, a particle diameter higher than 250 μm could reduce the transport capacity T_C and consequently the total sediment transport. The remaining parameters exert a smaller influence on the output. The sediment transport is directly proportional to the detachment coefficient K_{sd} and inversely proportional to the soil texture Z, which is included in the exponential reduction factor e^{-Zh} included in the DR in Eq.(3.6).

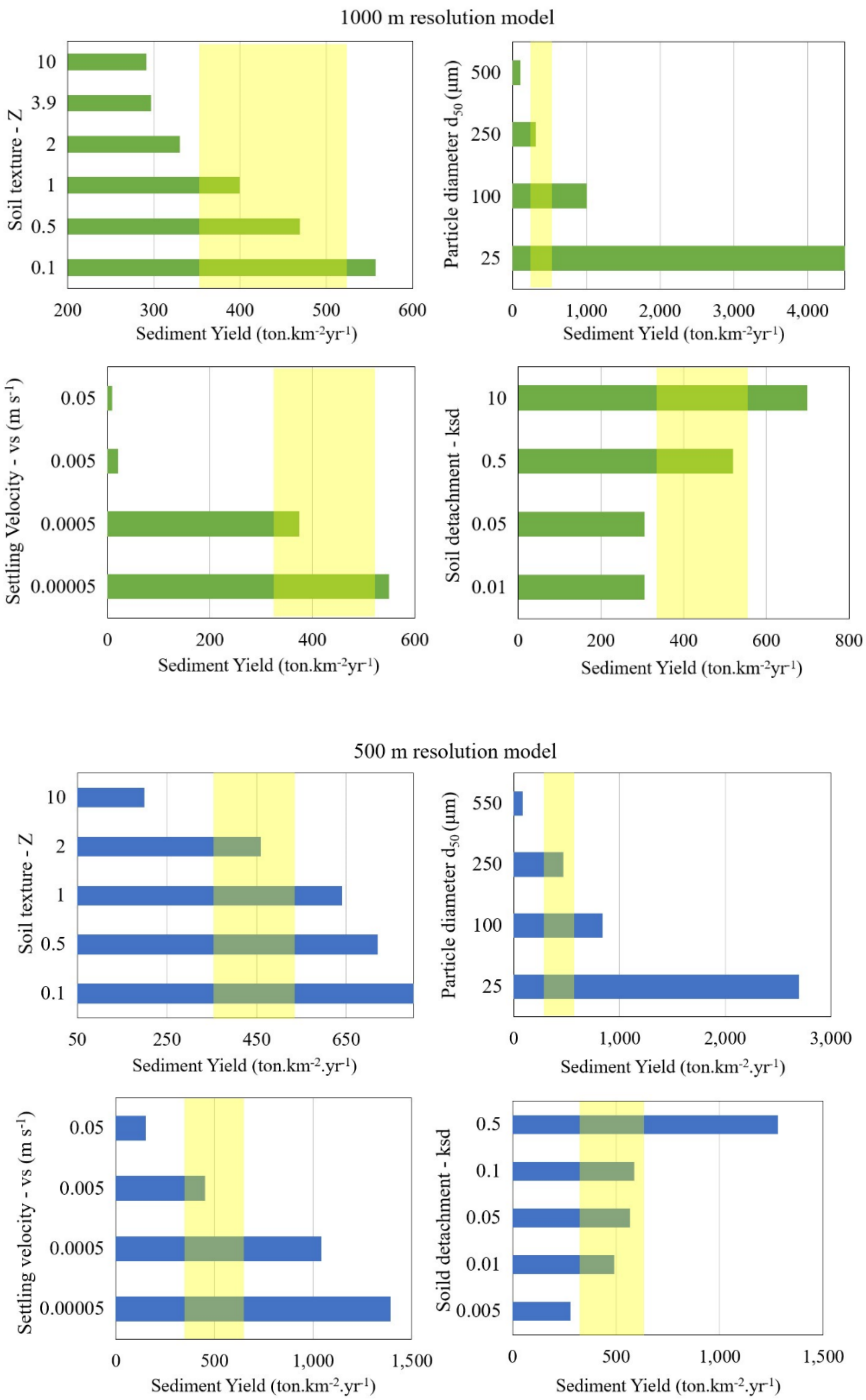

Figure 5-8 SSY results comparison at 500 m and 1,000 m resolutions for each parameter range. The yellow bar represents satisfactory range for SSY results (341 to 556 t.km^{-2}.y^{-1}).

For the 500-m model, the settling velocity is shifted to a range of 0.005 to 0.0001 m/s according to Figure 5-8. This implies that the most important aspect of the downscaling is an increase in the settling velocity input values (by a scaling factor of 10). The soil detachment and soil texture remain the least sensitive parameters and demonstrate maintenance of the same range of input values. Another important aspect of downscaling is a different C_S behavior. A gentle rising limb in the sediment graph and steeper recession is observed when the parameters are tuned to 500 m (refer to Figure 5-6).

5.6 Chapter conclusion

In this chapter, the development of an integrated hydrological and sediment model was discussed which combined hillslope hydrological and sedimentary processes that concluded in the river routing process. This is a novel sediment transport simulation approach to offering ungauged predictions for the Andes Mountains, where lumped models have been applied without the accurate consideration of the topography. The generation of sediment by surface flow and the detachment as a result of raindrop impact have been considered a driving erosive mechanism underlying the production of a sediment via an extreme rainfall event occurring on a slope. Upon assessing the trends identified by the Peruvian Geophysical Institute and comparing these with the produced model, a good fit of the simulation to hysteresis loop behavior was demonstrated when performed at a resolution of 1,000 m for the year 2016.

The influence of topographic resolution on sediment parameters was also analyzed, and it was found that the particle diameter (d_{50}) and the settling velocity (v_s) were the most sensitive parameters in terms of producing sediment and yielding sediment as output. These parameters must be prioritized when applying a physically-based hydrological and sediment model.

(This page intentionally left blank)

Chapter 6. Generation of sediment rating curves for a mountainous basin in Peru and consideration of the effect exerted by ENSO on the characteristics of the rating curves

6.1 Introduction

The ENSO (El Nino Southern Oscillation) is a quasi-periodic event that produces some of the most considerable inter annual variabilities in the Pacific atmospheric system. The effects of ENSO on the Peruvian coast are measured by assessing the climatic and hydrological anomalies that occur (Tote, et al., 2011). The effects of the ENSO phenomenon can be estimated in terms of typical rainfall intensities and distribution (Lagos, Silva, Nickl, & Mosquera, 2008), with a noticeable increase in the concentration of sediment recorded at gauging stations. Furthermore, recent risk survey and satellite observations have provided correlations between extreme ENSO events and increasing flooding and the associated economic impact (Khalil, Kwon, Lall, Miranda, & Skees, 2007).

According to studies investigating the effects of climate change, the forecast for the next few decades includes a higher frequency of ENSO events and a consequent increase in rainfall persistence. Therefore, the necessity to improve the estimation of sediment transport for river management (dredging, flood control, and riverbank protection) and ecosystem protection is deemed necessary for Peruvian river basins. The control of sediment transport and short-term predictability are considered essential for infrastructure management in ungauged basins. To establish a relevant forecast tool for river management, an integrated distributed sediment model was developed by adding information on the production and transport of sediment into a distributed rainfall-runoff model 1K-DHM (1-km resolution Distributed Hydrological Model) (Kyoto University, 2021), which enabled the simulation of both discharge and sediment concentration. An accuracy assessment and equifinality analysis was conducted for a range of hydrological and sedimentary parameters (Chero & Tachikawa, 2020).

In this section, application of the sediment routing model to Tumbes River basin in Peru has been discussed, considering the impact of the extreme ENSO events in the basin, the flood history, substantial amounts of sediment transported, topographic characteristics, and preliminary studies available.

This chapter is structured by introducing the following contents: in Section 6.2, the study area and the context in which ENSO affects the hydrological cycle have been described. In Section 6.3, the methodology that was used to develop the model has been provided. Considering the complexity of the sediment transport process, it is appropriate to perform a daily numerical integration between the sediment concentration and discharge. In Section 6.4, the hydrological parameters that were identified in the previous sections were applied to obtain an estimation of the river discharge and the concentration of sediment in ENSO and non-ENSO years. Next, model validations were conducted based on the sediment samples and gauged discharge acquired in the years 2012 to 2016. A database of water samples collected periodically by the Peruvian Geophysical Institute (IGP) were referred to for validation of the sediment transport. The regression analyses of the sediment rating curves has been discussed to examine the effect of the ENSO events on the production of sediment in Section 6.5.

The scope of the study described in this chapter was to analyze the remarkable effects exerted by extreme ENSO events on the generation of sediment in an ungauged basin in Peru by using a computer distributed sediment model and limited gauged data. The sediment rating curves generated and the hysteresis loops produced were compared by the Peruvian Institutes to understand the effects exerted by the ENSO on runoff and sedimentary processes with the physical interpretation of hysteresis behavior under conditions of extreme rainfall events.

6.2 ENSO effects exerted on the Tumbes River basin

To describe the effects of ENSO on the basin, it is necessary to recall two important indices that are conventionally used. The SOI (Southern oscillation index) difference and SST (Sea surface temperatures) anomalies in Region Nino 3.4 illustrated in **Figure 6-2** describe the strength of ENSO. Both indices are positively correlated and have been studied previously by Bazo, de las Nieves, & Porfirio da Rocha (2013).

The inter-annual variability of the runoff is predominant in coastal basins, including the Tumbes River basin, and there is robust scientific evidence that the SST and SOI are related to the origin of the variability in rainfall and runoff in the northern Peruvian territory under conditions of the occurrence of ENSO events (Lavado, Ronchail, Labat, Espinoza, & Guyot, 2012).

The satellite estimated rainfall data GSMAP were used to reflect the strong temporal and spatial variability of precipitation, and this has been discussed in the next section. Atmospheric effects were included in the definitions of SST and SOI as the spatial distribution anomalies in the input data. The phenomena termed as "the short-wave effect" consists of a micro weather system that is persistent for a considerable duration in the rainy season in Region Nino 2 presented in Figure 6-2. The effects of this system enhance heavy precipitation with an accelerated rainfall runoff cycle near the downstream section of the Tumbes River.

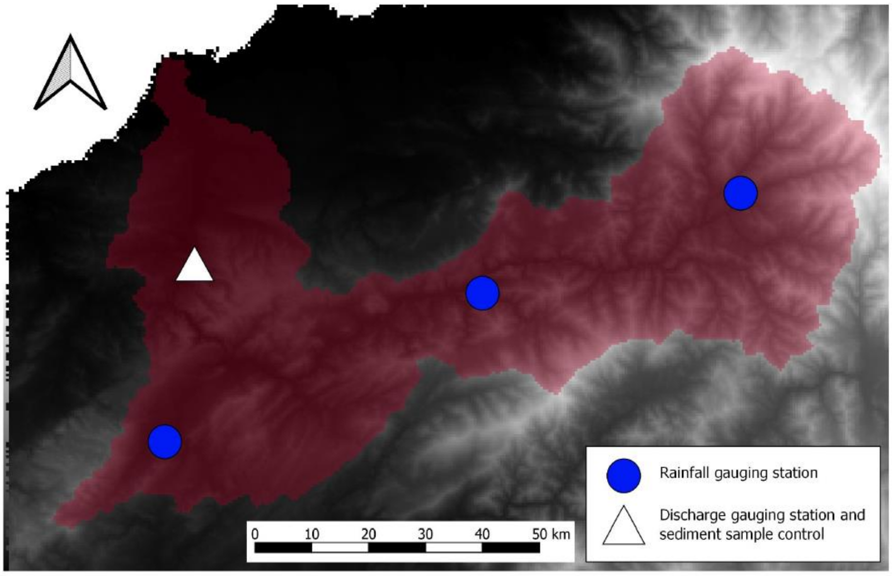

Figure 6-1 Tumbes River basin DEM and river delimitation at 1 km resolution.

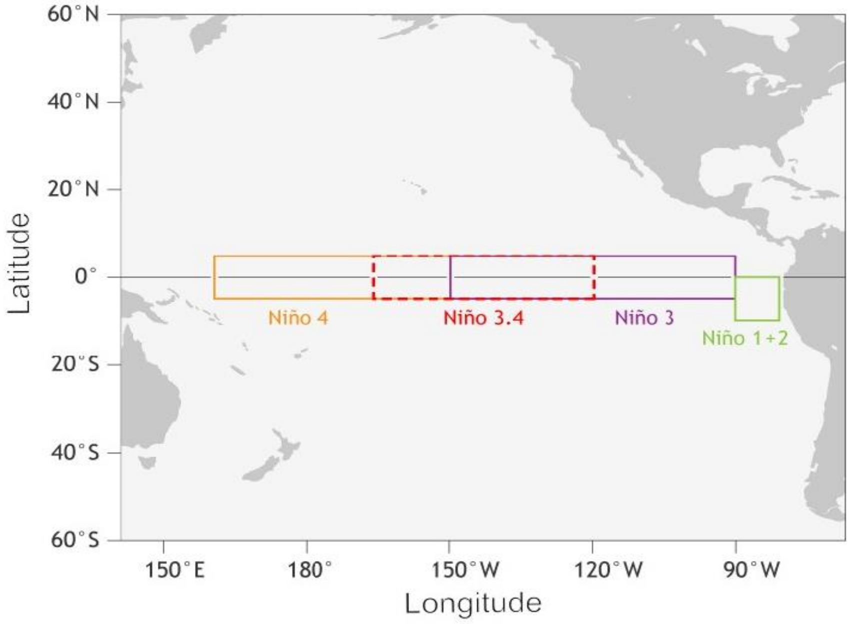

Figure 6-2 Location of El Nino regions. For our research Region 3.4 and 1+2 interaction is for particular interest.

6.3 Data sources and quality analysis

Rainfall data was recorded at three rainfall gauging stations located in Ecuador (2 stations) and Peru (1 station), as illustrated in **Figure 6-1.** The hourly average discharge data (in m^3 s^{-1} units) at the outlet were provided by SENAMHI (Peruvian National Service of Meteorology and Hydrology).

To consider the marked spatial distribution that was associated with the strong ENSO events reported in 1983 and 1998, bias correction was performed to the GSMAP grid-based database with reference to the gauged rainfall intensity, from which a spatially distributed rainfall data file (*P*) with (mm h^{-1}) units and a 1-km spatial resolution was obtained. The historical trend of the special conditions under ENSO in the study basin is shown in **Figure 6-3**.

The distributed rainfall input used in the distributed rainfall-sediment-runoff model (*I*) considers loss by evapotranspiration. The effective rainfall intensity (*I*) is provided by subtracting the monthly mean evapotranspiration rate (*E*) (mm h^{-1}). Samples of sediment were collected from the outlet located in the Peruvian territory from 2012 to 2016. After the conduction of laboratory processing at the IGP, the sediment concentration database (mg L^{-1}) were accessed.

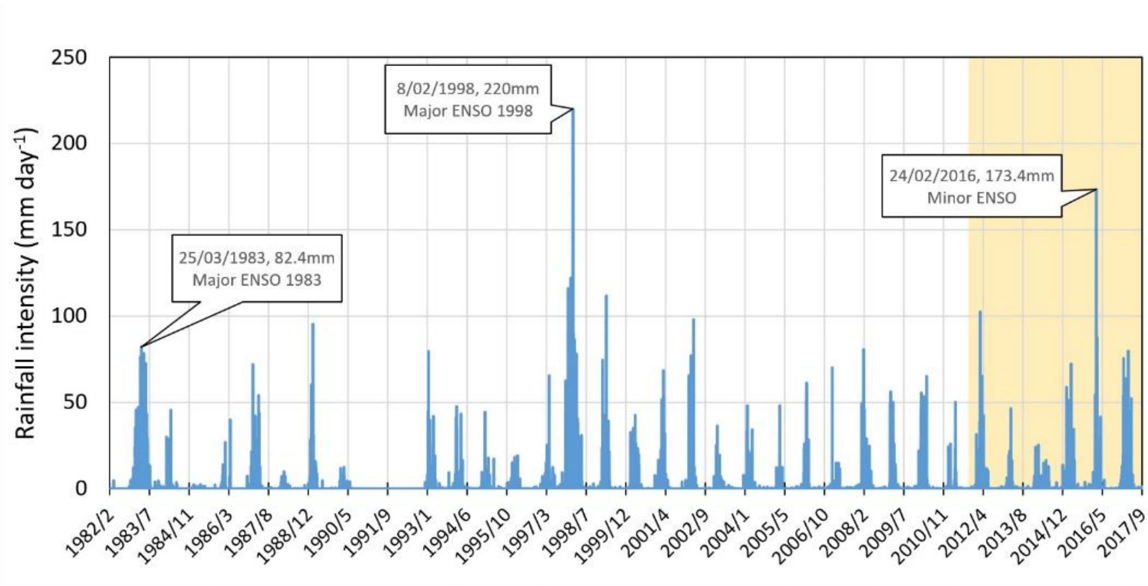

Figure 6-3 Historical gauging rainfall intensity P recorded at the Peruvian gauging station. The presence of ENSO is called in the white boxes. The orange shaded area belongs to the period in which sediment sampling was carried out.

6.4 Rainfall-runoff and sediment simulation results

6.4.1 Identification of the hydrological and sediment model parameters

The hydrological model parameters were set for each year after automatic calibration was performed using the SCE-UA package (Seong, Her, & Benham, 2015). This set of parameters represents the hydrological conditions for a specific year (degree of saturation, runoff conditions, and infiltration velocity) according to **Figure 6-1**.

The sediment flux T_R (t d^{-1}) and field sediment samples help in the obtainment of relevant information with which the impact of the extreme phenomena in ENSO can be analyzed. The simulation uncertainty is further reduced by conducting model sensitivity analysis using the sedimentary parameters included (**Figure 6-2**). Identification of the sensitivity by which the sedimentary parameters exert influence on the sediment yield was previously performed by Chero, Tachikawa, Yorozu, & Ichikawa (2020) for the river basin, wherefrom it was suggested that the particle diameter d_{50} and the settling velocity v_S were critical variables that could result in the highest divergence in terms of sediment transport (mg L^{-1}).

The simulated sediment graphs presented in **Figure 6-4** display the average daily sediment concentration C_S (mg L^{-1}) for the rainy season in the ENSO years 1983 and 1998. These graphs provide information on the manner in which the daily average simulated sediment concentration behavior is compared to the discharge peaks in terms of lag and the scale of the peaks. The river discharge information is plotted as blue lines and the sediment concentration is depicted as yellow lines in these figures. Special behavior is evident in terms of the sediment concentration when the ENSO is present in the hydrological cycle of the basin. On the other hand, the simulated sediment graphs for the non-ENSO years 2012, 2014, and 2016 presented in **Figure 6-5 (a) to (c)** display a linear response in the peaks and lag associated with discharge. This has been discussed in Section 6.5.

The relation between monthly mean river discharge and sediment concentration presented in **Figure 6-6** was deduced by the IGP considering the non-ENSO years from 2008 to 2015. The average monthly values obtained from 2008 to 2015 have been plotted in the white circles in the figure. Indeed, it is noticeable that the monthly behavior follows a clockwise hysteresis loop under non-ENSO conditions. The results of the simulations conducted in the study are indicated by using the green diamond markers in Figure 6-6. Hence, the model can be considered to reproduce the sedimentary transport according to the preliminary assumptions and mathematical relations.

6.4.2 Sediment model validation

Validation of this model was performed by assessing the simulation performance under standard soil conditions (in which the soil parameters are maintained constant). Automatic calibration indicated that the set of parameters in **Table 6-2** roughly represented a baseline for each parameter in each year (2008 to 2015). Subsequently, the first reference validating the performance is the loop behavior of the monthly average relationship between sediment concentration and gauged discharge that can be observed in Figure 6-6 Tumbes River discharge-sediment concentration relationship. The monthly average simulation for non-ENSO years is displayed in the green diamond markers.

Table 6-1 Hydrological parameters during important years for the analysis.

Parameters for relevant ENSO events						
ENSO status	Strong	Strong	Neutral	Neutral	Moderate	Observations
Year	1983	1998	2012	2014	2016	
Hydraulic simulation parameters						
$n_{channel}$	0.03	0.03	0.03	0.03	0.03	Set as default
n_{slope}	0.1	0.1	0.1	0.1	0.1	Set as default
K_a	0.0007	0.0015	0.005	0.007	0.0015	According to the event
D_a	0.8	2.8	0.8	1.6	0.8	According to the event
D_m	0.6	2.6	0.6	1.8	0.4	According to the event
Beta	6.3486	6.3486	6.3486	6.3486	6.3486	Set to default

Table 6-2 Sediment simulations parameters.

Parameters for major ENSO events							
ENSO status		Strong	Strong	Neutral	Neutral	Moderate	Observations
Symbol	Units	1983	1998	2012	2014	2016	Parameter
Z	–	2.5	2.5	2.5	2.5	2.5	Soil Texture
C_S	$m^3\ m^{-3}$	$5x10^{-6}$	$5x10^{-6}$	$5x10^{-6}$	$5x10^{-6}$	$5x10^{-6}$	Initial sediment concentration
ρ_S	$kg\ m^{-3}$	2650	2650	2650	2650	2650	Soil Density
β_S	–	0.65	0.65	0.65	0.65	0.65	Correction factor to calculate cohesive soil erosion
υ_S	$m\ s^{-1}$	0.00001	0.00001	0.00001	0.00001	0.00001	Particle settling velocity
k_{sd}	$g\ J^{-1}$	0.005	0.005	0.005	0.005	0.005	Index of soil detachability
ω_{cr}	$m\ s^{-1}$	0.4	0.4	0.4	0.4	0.4	Critical value of stream power
d_{50}	μm	250	250	250	250	250	Median particle size

To complete the validation stage, the relationship between discharge and sediment concentration from observation and simulation is considered. The plot discharge Q ($m^3\ s^{-1}$) in the horizontal axis and sediment transport T_R ($t\ d^{-1}$) is presented in the vertical axes of **Figure 6-7, 6-8, and 6-9**. A logarithmic scale was used for both axes and a power law regression was set to compare with the results of the assessments that were based on sediment samples. The simulation results were found to significantly overlap with the observation plots. Guidelines that have been established by Syvitski, Morehead, Bahr, & Mulder (2000) indicate that the rating curves could correlate natural conditions to certain plot regions according to the range of the coefficient and exponent values of the regression curve. To validate the findings, these authors strongly recommend using data collected continuously over a timeframe of more than 3 years or using those collected in a non-continuous manner over a timeframe of more than 1000 days (within the years 2012 to 2015 in this case).

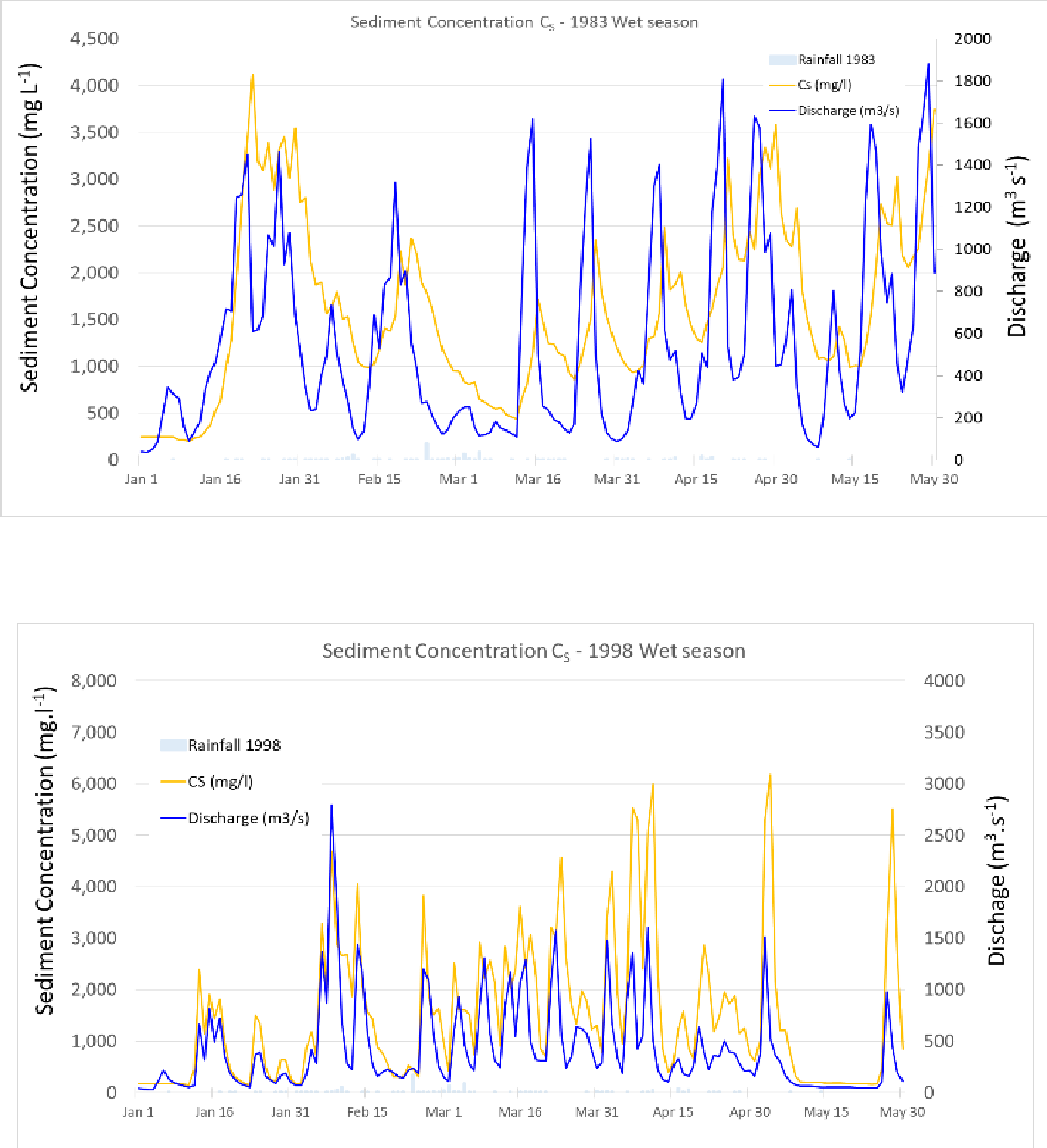

Figure 6-4 Sediment concentration and river flow simulation results for strong ENSO presence.

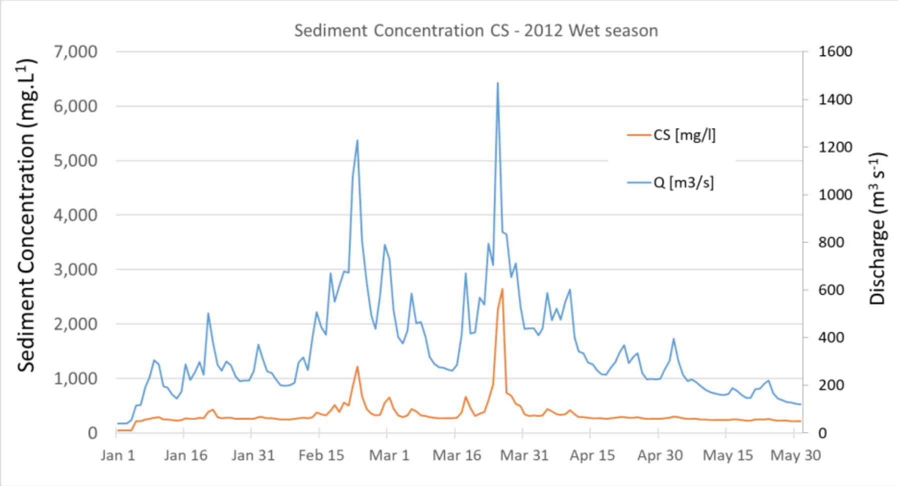

(a) 2012 Rainy season

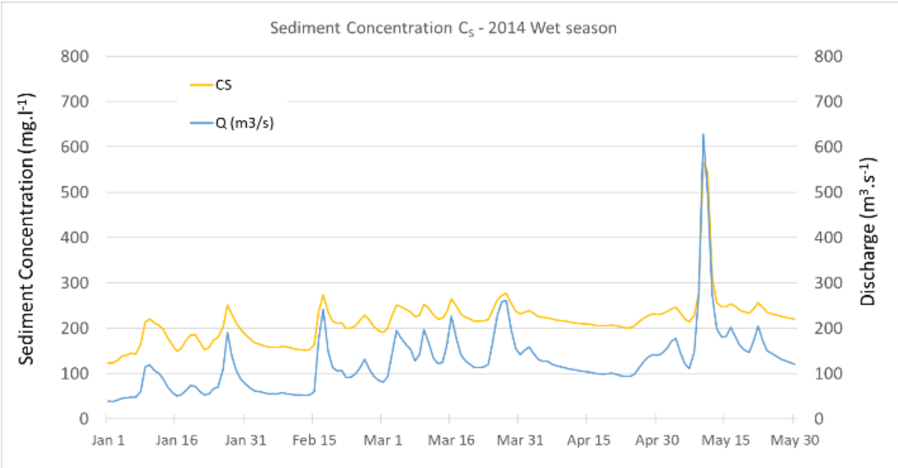

(b) 2014 Rainy season

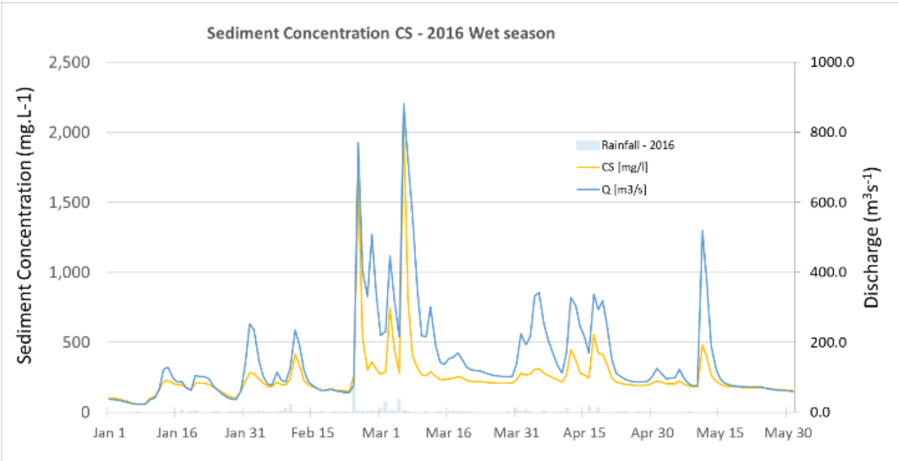

(c) 2016 rainy season

Figure 6-5 Simulated sediment concentration.

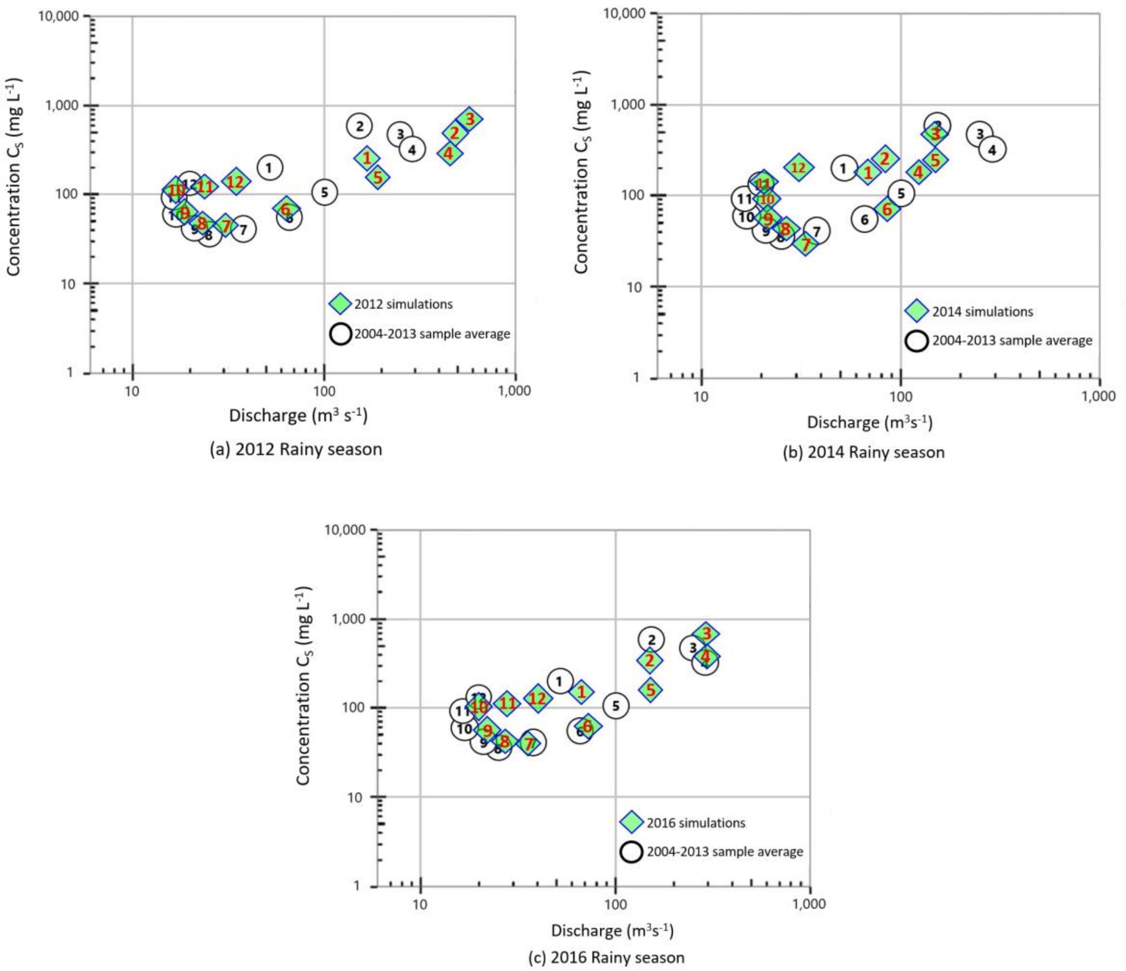

Figure 6-6 Tumbes River discharge-sediment concentration relationship. The monthly average simulation for non-ENSO years is displayed in the green diamond markers. The historical average for non-ENSO years is displayed in the background (2004 to 2014 samples originally taken by Morera (2014)).

6.5 The effect of ENSO on sediment generation

6.5.1 The effect of the ENSO on sediment rating curve

(1) Regression analysis of discharge and sediment

The results of the sediment transport simulations reveal important findings in the sediment rating curves in terms of the relationship between river discharge and sediment transport. Similar trends are observed in the sediment rating curves (**Figure 6-7 to 6-8**). Particularly, the relationship between simulations and samples collected during the rainy season was considered.

To initiate formulation of the mathematical description, the regression function is defined by using the following notation:

$$Q_S = aQ^b \qquad (6.1)$$

Here, coefficient *a* represents the erosion sensitivity and is affected by the river peak discharge; the value is usually higher than 0.5 for events related to ENSO conditions ranging from mild to strong intensities. Exponent *b* reflects the availability of sediment for extreme rainfall events, which is directly affected by the particle size distribution d_{50}. This parameter also exhibits a positive correlation with mean discharge. Syvitski, Morehead, Bahr, & Mulder (2000) stated that *b* changed with respect to physical erosional processes.

The scattering of the results in **Figure 6-7–6-9** reflects the expected result of spatio-temporal rainfall input and the direct effect of erosion that results from raindrop impact. This feature is observed in both the water samples obtained at the laboratory and the simulation results.

Figure 6-10 illustrates multiple simulation plots for daily discharge and sediment transport during the ENSO years 1983 and 1998 and the non-ENSO years 2012–2016. It was hypothesized that the regression curve generated based on the historical simulations conducted in non-ENSO years from 2012 to 2016 represents standard river conditions (termed as the baseline). This baseline (indicated by using a black line) was the result of the simulation that was performed using the soil parameters listed in **Table 6-2**.

A comparison of the simulations obtained in this study from which relevant insights could be put forth about the ENSO classification status for each year has been presented in Figure 6-10. It is noticeable that the simulations exhibit consistent patterns according to the presence of ENSO and acceptable R^2 values in most years (**Table 6-3**). The pattern is also noticeable in the two regions (indicated in blue and red) that show a wider arrangement of data clusters. Thus, a mathematical description and an interpretation for two regions can be deduced. The extreme precipitation that was associated with ENSO in the years 1983 and 1998 influenced the model, resulting in higher-than-predicted data compared to the baseline. It is observed that the scattered points that are associated with higher sediment transport in the blue-highlighted region may be described by using the sediment transport equations, specifically by Eq.(3.5) and Eq.(3.6).

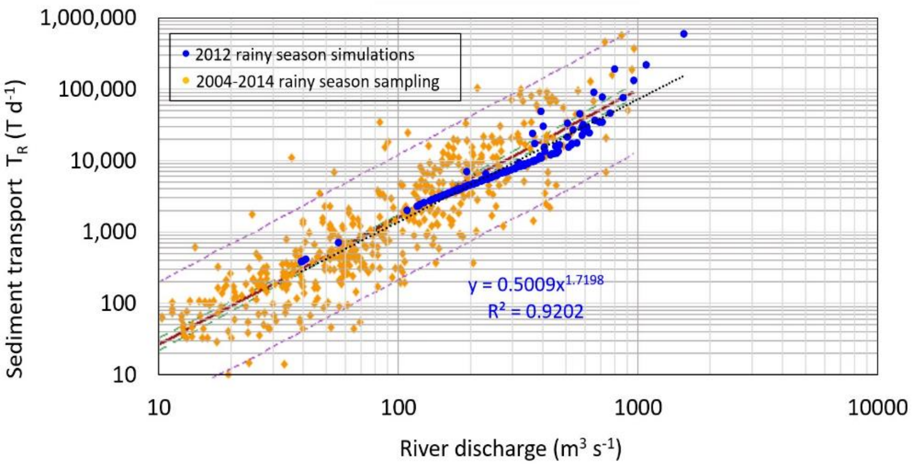

Figure 6-7 Sediment samples and simulations for rainy season in 2012. Simulation results for year 2012 are plotted over sampling data according to Quincho (2015).

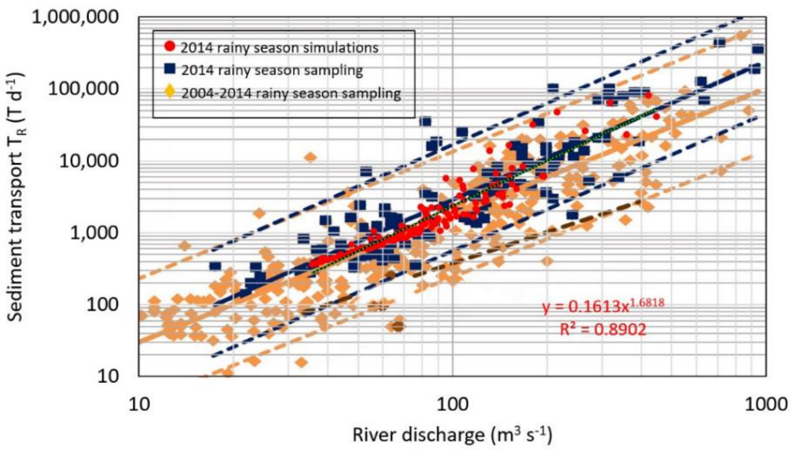

Figure 6-8 Sediment samples and simulations for rainy season in 2014. Simulation results for year 2014 are plotted over sampling data according to Quincho (2015).

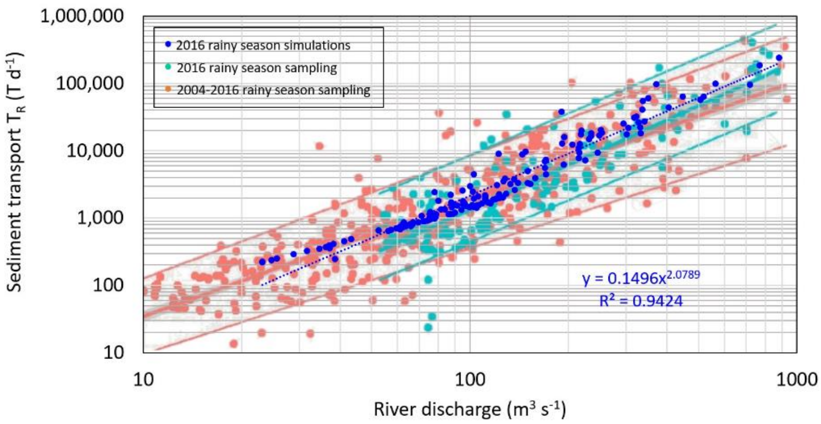

Figure 6-9 Sediment samples and simulations for rainy season in 2016. Simulations results for year 2016 are plotted over sampling data according to Goyburo (2017).

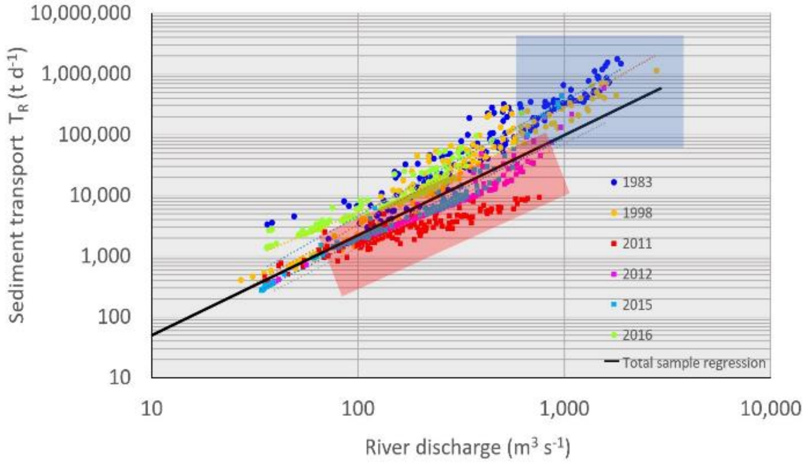

Figure 6-10 Tumbes River rating curves based on simulations for relevant years regarding ENSO presence. The black bold rating curve is the power regression for the 2012 to 2016 complete set of simulations.

Table 6-3 Sediment rating curve for the representative simulation years.

Year	Regresion from water samples		Regression from simulations	
1983 (strong ENSO)	Not available		$y = 0.7511Q^{1.8948}$	$R^2 = 0.91$
1998 (Strong ENSO)	Not available		$y = 0.4516Q^{1.9329}$	$R^2 = 0.94$
2011 (regular rainy season)	Not available		$y = 20.462Q^{0.9442}$	$R^2 = 0.86$
2012 (regular rainy season)	$y = 0.5005Q^{1.7192}$	$R^2 = 0.92$	$y = 0.5009Q^{1.7198}$	$R^2 = 0.90$
2014 (regular rainy season)	$y = 0.2043Q^{2.0324}$	$R^2 = 0.87$	$y = 0.1613Q^{1.6818}$	$R^2 = 0.89$
2016 (weak ENSO year)	$y = 0.2345Q^{1.9769}$	$R^2 = 0.87$	$y = 0.1496Q^{2.0789}$	$R^2 = 0.94$
Historical average	$y = 0.65Q^{1.65}$	$R^2 = 0.69$	$y = 0.75Q^{1.59}$	$R^2 = 0.72$

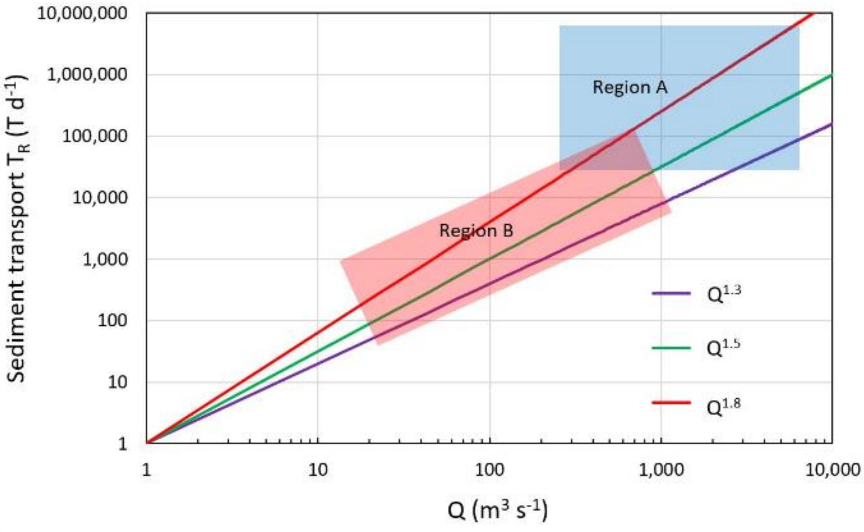

(a)

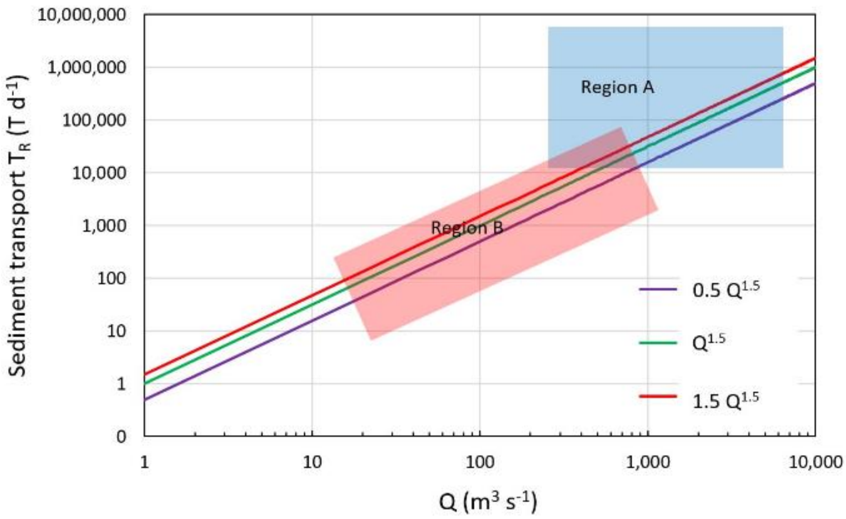

(b)

Figure 6-11 Difference of rating curves according to range of the exponent *b* (a), and according to range of the coefficient *a* (b).

(2) Interpretation of the regression results

The relevant outcome from the simulations and the rating curves generated represent the successful reproduction of the erosional process under conditions of extreme events. In the basin, the rainfall intensity that was induced by a strong ENSO represented an extreme event. The interaction between precipitation and surface water depth is included according to **Eq. (3.6)**, and the effects generated fit within the parameters established in previous studies that are related to the field of sediment transport (Hapsari, Onishi, Imaizumi, Noda,

& Senge, 2019). **Figure 6-11** shows a schematic plot indicating the interpretation of regression results in the following manner:

- Region A (blue) refers to the influence of extreme rainfall events and the mathematical relationship is represented by exponent b. Rating curves with exponent values ranging from 1.8 to 2.5 are plotted in **Figure 6-11(a)**. Values above 1.8 indicate high or extraordinary sediment transport. The exponent 2.5 represents the peak sediment transport according to strong ENSO events.
- Region B (red) refers to the area influenced by weak to mild ENSO events in which the erosion is described by coefficient a. The linear behavior that is the main feature in this range is represented by coefficient a as shown in **Figure 6-11(b)**.

The regression for water samples collected at the gauging station over the years 2012 to 2016 is expressed as:

$$Q_S = 0.65Q^{1.65} \qquad (6.2)$$

meanwhile, the regression based on sediment simulations is:

$$\mathrm{Q_S} = 0.75\mathrm{Q}^{1.59} \qquad (6.3)$$

A recent study reported by Tote et al. (2011) that was conducted at a neighboring southern basin (Catamayo-Chira Basin) helped identify few key elements related to the present study and the simulations conducted. The work describes the influence of pre- and post-ENSO events (Tote, et al., 2011) according to regions A and B. In the years after the occurrence of strong ENSO events, there is a possible increase in vegetation cover and this environmental change may extend the effects of sediment dynamics over longer periods. Consequently, the historical discharge from gauging stations also displays this trend for the Tumbes River (**Figure 6-10**). To include the discussed runoff trends, the hydrological parameters were prioritized by emphasizing on the Manning roughness coefficients in the years for which ENSO was forecasted. The hydraulic conductivity and capillary depth should therefore be set while considering the values that are found to fit the relevant events assessed by sediment sampling.

6.5.2 ENSO effects exerted on seasonal sediment transport

The purpose of organizing the simulations results in hysteresis loops is to describe the relationship between monthly average discharge and the suspended sediment concentrations, as shown in **Figure 6-12.** The loop enables the comparison of the events for different years for the same target basin.

Figure 6-12(a)(b) shows the relationship in the ENSO years 1983 and 1998. The hysteresis loop formed during non-ENSO years based on water samples collected from 2004 to 2013 is included in the background, published after many years of sampling by Morera (2014). This assessment method can be used to provide insights into the rainfall spatial distribution induced by ENSO events and the effects exerted by such events on discharge and sediment transport per month. Our findings are discussed by considering the following three points:

a) Hysteresis pattern during ENSO years

Lloyd, Freer, Johnes, & Collins (2016) argued that clockwise hysteresis patterns resulted from the concentration of sediments increasing at a higher rate compared to discharge during the rising limb. This expected behavior is observed in the years 2012 and 2014, with regular rainy seasons, In a cited article, Lloyd *et al.* support the theory that the intensity and persistence of rainfall control the sediment production response and the source of sediment in the middle to upper basin. On the other hand, during strong ENSO years, an anticlockwise and extended loop that resulted from longer lag between discharge and the sediment concentration time to peak flow was obtained as illustrated in **Figure 6-12(b)**. Hence, the ENSO events lead to unexpected behavior in the simulations (from moderate to strong). The explanation for the simulation of 1998 could be provided by describing a lag in the sediment concentration and the fact that the peak value was reached at the end of the rainy season given the persistence of the rainfall (please refer to **Figure 6-4**).

b) Sediment deposition in channels

One component that is not implicitly included in the simulations is the deposition of sediment in gully sections and its sudden transport response (channel simulations *DF* described in Section 3.2). Higgins et al. (2016) performed a thorough assessment of the deposition in the Magdalena River, Colombia via the conduction of simulations. This river basin exhibits similar topographic characteristics to the study area in terms of basin relief, with the upper catchment located in the Upper Andes. The assessment indicates the unusual pattern in the hysteresis behavior during an ENSO event, and provides an argument that the availability of sediments in channel sections increases in the years after the occurrence of extreme events. The ENSO effects in the Tumbes River can therefore be considered analogous to those of the Magdalena River. As outlined in Sections 2 and 3, this model contains a component that simulates the erosion of sediments on hillslopes and the transport of sediment in channel sections according to the assigned threshold number, with the difference leading to a forward step in the simulation. The simulation process in this study can be considered non-linear based on the discharge calculations and is also constrained to the sudden increases in rainfall and the runoff height in the Andes that are achieved by solving differential Eq.(3.6). These results indicate that the nature of the sediment in this model is non-linear, and the hysteresis loops reflect this component.

c) The variation of topographical features

The simulations of regular and extremely rainy seasons indicate that the model can simulate erosion by assigning uniform erosion conditions for the entire basin. The model resolution at 1000 m enables representation of the topography with rectangular slope elements, supporting the approach that a moderate slope is included throughout the solid flushing path. However, events such as landslides or topographical changes were not considered over the simulation time-lapse. The concept of landslides and the evolution of a profile over time were previously assessed by Roering, Kirchner, & Dietrich (2001), who demonstrated that an equilibrium profile in which gravity effects and critical saturation produced landslides could be reproduced by establishing a constant value across the hillslope. Soil-weathering parameters (Table 6-2) were therefore used in this study to address the magnitude of erosion and to optimize the simulation by assuming that no change occurred at the slope angles over the simulation period.

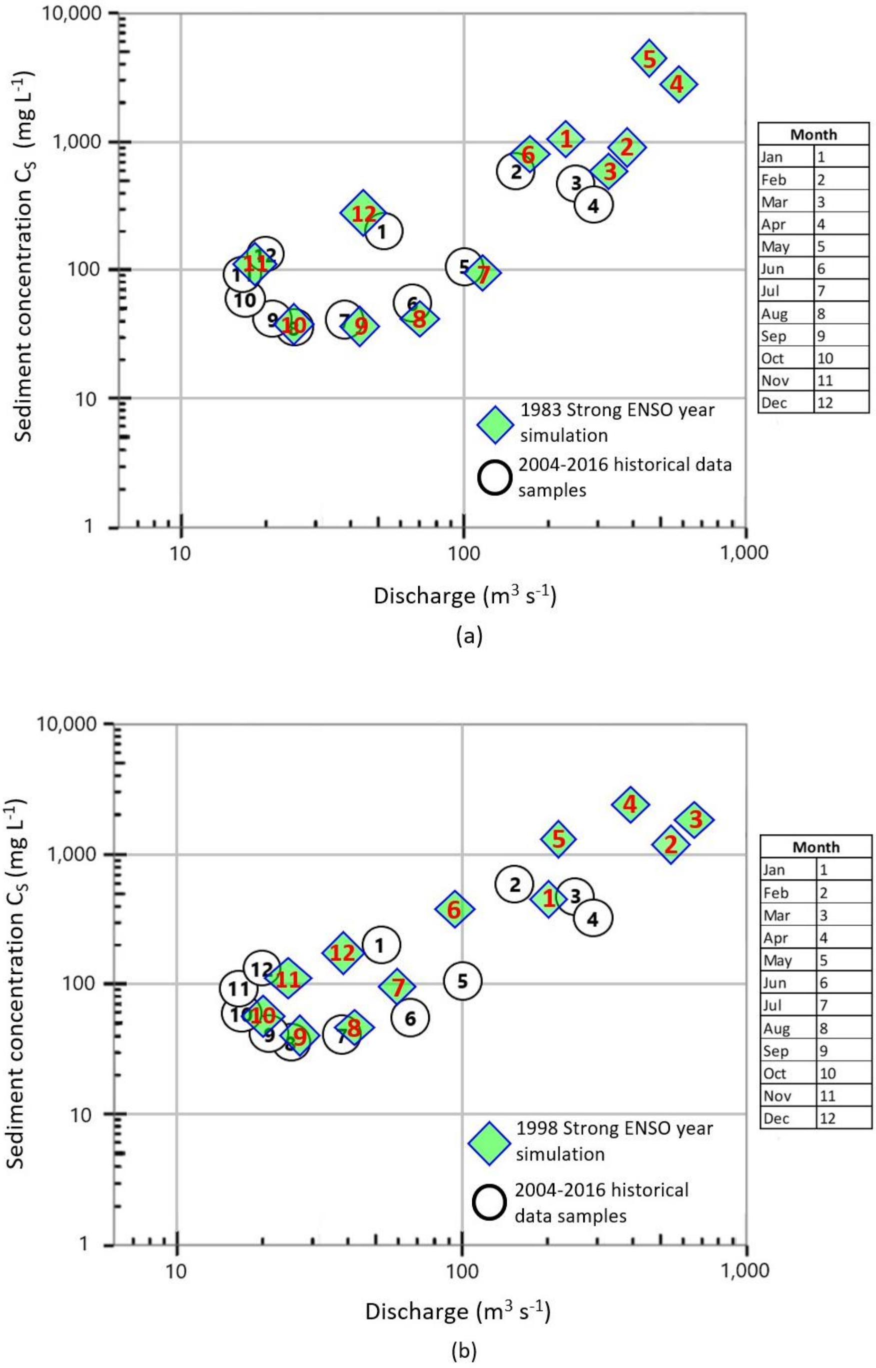

Figure 6-12 Hysteresis loop after Strong ENSO years 1983(a) and 1998(b) using simulated results (Historical non-ENSO background data in white circle markers is based from IGP and (Morera, Condom, Crave, Steer, & Guyot, 2017)).

6.6 Chapter conclusions

The mean daily and monthly sediment transport for the Tumbes River basin can be predicted by adopting a distributed rainfall-sediment runoff model that consists of slope and river flow processes, including sediment generation and transport processes. The appropriate hydrological and sediment parameters that can help avoid equifinality in the results were found, regardless of the ENSO or non-ENSO presence, by using the sediment rating curves as discussed.

The rating curves provided important insight that can be used to describe the relationship between the transport and discharge of sediments and to understand the manner in which rainfall intensity affects the sediment yield. The interpretation for the strong ENSO years 1983 and 1998 can be put forth by describing an instant increase in the amount of sediment transported and the instant production of sediments occurring as a result of the persistent rainfall and the extreme rainfall recorded. The difference between the ENSO and non-ENSO events is 10 to 100 times the average sediment transport rates.

It is also understood that a strong ENSO event with a stationary storm system in the lower basin produces sediment hysteresis loop behavior that indeed differs from the findings obtained for average studied samples from the IGP. The strong ENSO years 1983 and 1998 display a counterclockwise loop result. Both examples of the “Short-wave phenomenon” induced by ENSO are current research topics for the Peruvian Coast and this study is an attempt to describe the physical relationships between the ENSO process, the damage caused by flooding, and the increase in the amount of sediment transported.

For improvement of the predictions, extension of the sampling frequency is complicated in terms of safety and operational aspects; however, it is strongly recommended that the construction and precision of rating curves should be improved for future short- and long-term simulations. A detailed time and space distribution of the rainfall forecast for an ENSO event is also essential to properly estimate the river discharge and sediment transport.

(This page intentionally left blank)

Chapter 7. Discussion on ENSO effects exerted on the sediment dynamics of the Tumbes River basin in Peru

7.1 Introduction

The objective of the study described in this chapter is to describe the research problem, state and test the hypothesis regarding the effects of ENSO on erosion and the runoff process, and to demonstrate the findings obtained.

The general outlook for Peru during strong El Nino years was previously studied by Lavado, Felipe, Silvestre, & Bourrel (2013). There is a noticeable increase in sediment concentration, and the relationship described (Chapter 6, Section 6.5.b) is the most accepted and discussed aspect among various scientific journals and reports.

According to Tote et al. (2011), extreme climate variation causes marked changes in the seasonal transport of sediments. In this chapter, a comparison of ENSO studies has been described to simulate the years before and after the occurrence of the ENSO, which was based on the successful methodology and simulation algorithm discussed in Chapters 5 and 6. For instance, it is expected that similar rating curve parameters and basin response will occur for the Tumbes Rivers and its neighboring basin, Catamayo-Chira.

7.2 Analysis method of determining ENSO effects exerted on sediment routing

The research question for the Tumbes River basin was initiated with the purpose of understanding the effects exerted by ENSO on erosion and runoff processes.

It is hypothesized that ENSO events result in an increase in rainfall because of a stationary cumulus convective rainfall scheme. As a consequence of the runoff, an increase in the kinematic force of the stream is expected in the middle basin; indeed, increased peaks of rainfall runoff were recorded (by SENAMHI) in the rainy season between January and February in 1983, 1998, and 2016.

A further explanation of the increase in sediment transport may be provided to suggest that the anomaly observed in the distribution of rainfall during the years 1983 and 1998 may lead to a stationary phenomenon in the lower basin that flushes out the deposited sediments, which will contribute to a marked increase in sediment transport (**Figure 7-7**).

7.3 Description of ENSO-specific conditions in the Peruvian Coast

7.3.1 Normal conditions

Under regular conditions, the orographic effect predominates at lower elevations on the eastern slopes of the Andes Mountains, while on the western slopes, low precipitation rates are observed because of low sea surface temperatures. Precipitation increases with elevation. This feature is recurrent on all coasts with increasing elevations that are observed below 2100 m a.s.l.

7.3.2 El Nino Conditions

As described in Chapter 1, ENSO results in atmospheric pressure changes that lead to convection off the Pacific Coast of Peru, and this can result in heavy rainfall. The convection and high SST are considered as the main mechanics that drive the stationary effect (rainfall occurs in the same place) in the North Pacific Coast of Peru. The description according to the degree of ENSO highlights a range from weak El Nino (WEN) to strong El Nino (SEN). It is also important to consider the study reported by Barry (2008) when setting the standard rainfall intensity for average and ENSO scenarios across the Andes in **Figure 7-1** in the following manner:

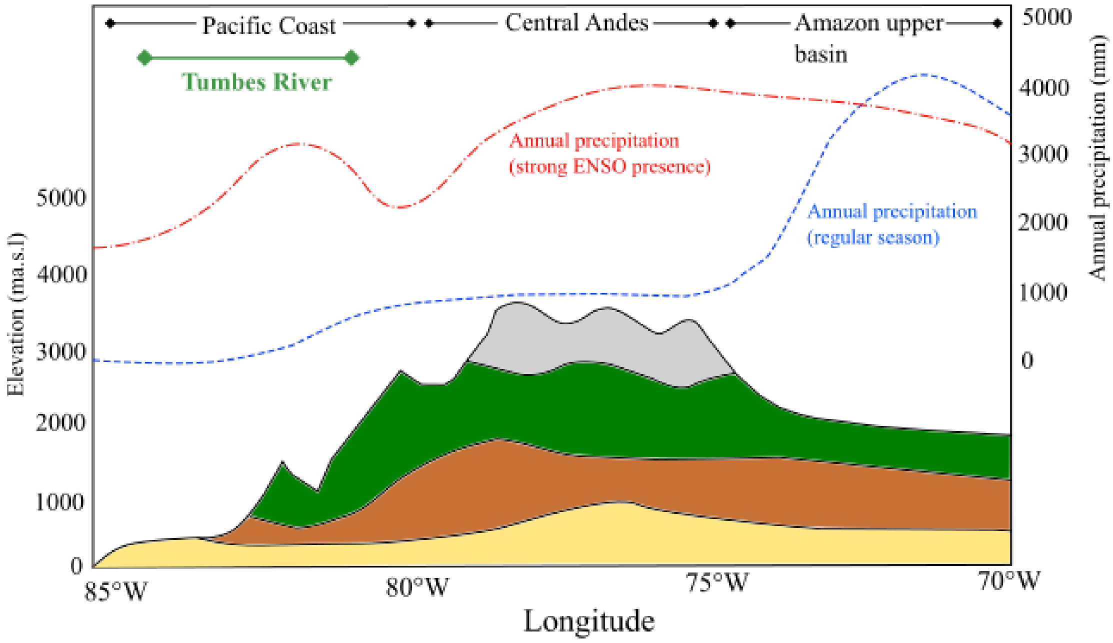

Figure 7-1 Anomaly of ENSO in the transverse Andes at latitude 5°S. Based on Barry (2008).

During the rainy seasons in 1983, 1998, and 2016, the NOAA and the SENAMHI declared the occurrence of an ENSO after measuring an increase in the SST from 26 to 29 °C in the eastern Pacific; thus, flooding and a specific rainfall distribution was expected in the middle and lower Tumbes River Basin.

The years 2012, 2013, and 2015 were declared normal in terms of events, as the sea surface temperature recorded was in the range 23 to 25 °C in the rainy season. The sediment routing simulations were performed with the log-log regression fit according to the relationships established by the rating curves described in Chapter 6 (see Figure 6-10).

The arranged gauged hydrographs for years representative of ENSO and non-ENSO conditions were placed alongside the average rainfall readings in the secondary axis, and were used to illustrate **Figure 7-2**. These years were selected with the purpose of obtaining evidence of the actual behavior of rainfall-runoff, and to support the theory based on sediment sample analysis and simulations described in Chapters 4 and 5.

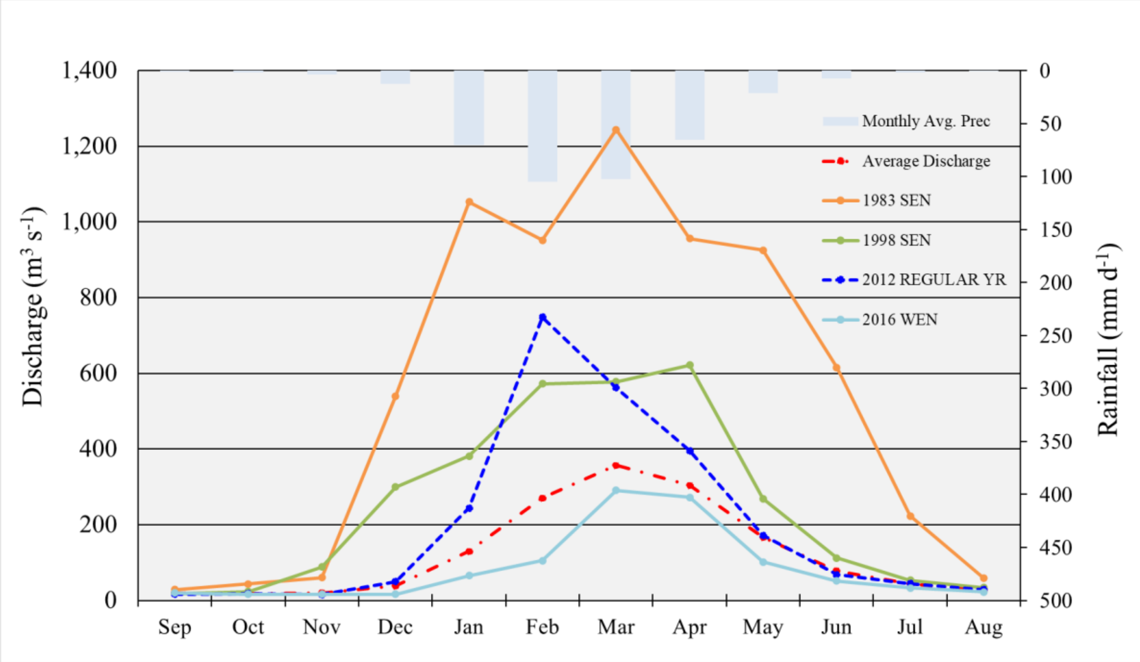

Figure 7-2 Historical monthly average observed discharge at Gauging Station, it includes the monthly average simulations for relevant ENSO events.

If emphasis is laid on the daily average discharge (**Figure 7-3)**, it can be also inferred that the ENSO events will lead to many iterations of high-intensity rainfall cycles, especially in the year 1983 that is deemed the most representative year studied. It is possible to appreciate the persistence in discharge when it reaches a value above 800 m^3s^{-1} in the rainy season during 1983. Discharge of above 400 m^3s^{-1} was observed between January and April in 1998. Additionally, the event in the year 2016 was declared as a weak ENSO event with lower than average rainfall intensity observed for the Tumbes River. This specific year is described by considering the rating curve exponents discussed in Section 2. Finally, the sediment transport in Figure 7-7 is described according to the presence of ENSO.

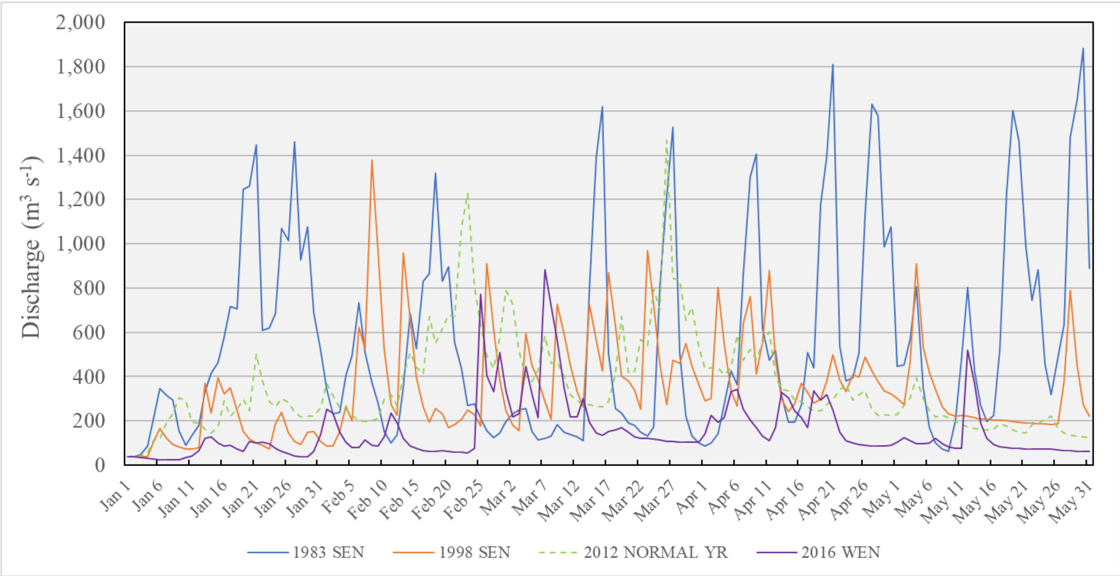

Figure 7-3 Historical daily average observed discharge at Gauging Station, according to the degree of ENSO.

It has been proposed to refer to such a stationary rainfall pattern and consequence in the hydrological cycle and sediment transport as the “short-wave effect”; this term has been used to summarize the aforementioned factors discussed in Section 6.5. During an ENSO event in the rainy season, the main characteristic of the stationary rainfall is a precipitation anomaly of beyond > 1000 mm in focused areas of the lower basin and up to 300 mm in the middle basin. Based on a comparison of the rainfall distribution during strong ENSO events (1983 and 1998), the weak ENSO event in 2016 and the regular year 2012 can be observed in **Figure 7-4**. When strong and moderate ENSO events occur, anomalies in the distribution of rainfall can be described according to isohyets and information can be used as inputs for the establishment of distributed hydrological models.

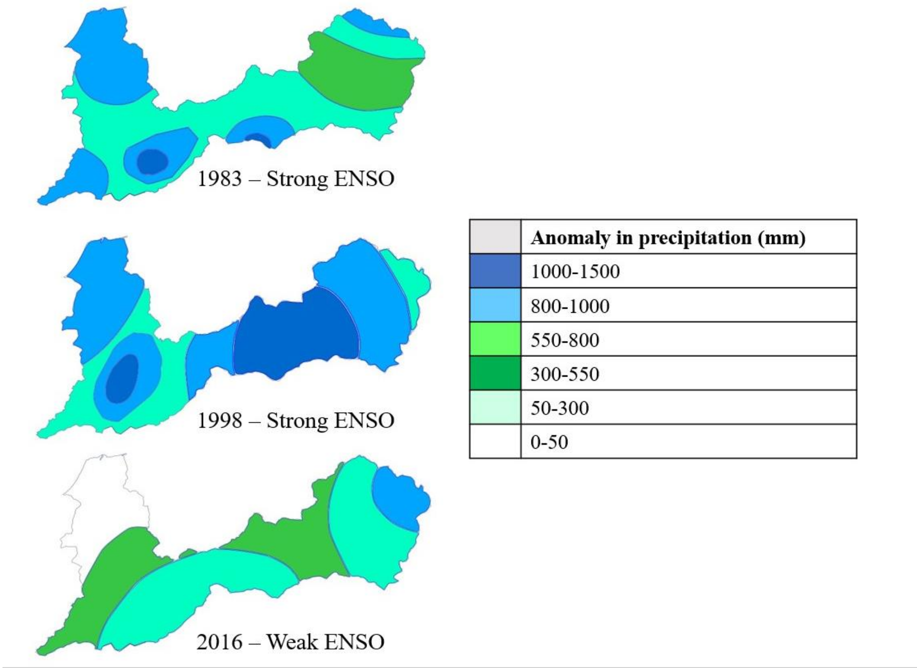

Figure 7-4 Anomalies in rainfall intensity in reference the ENSO presence (This is in reference the months of January to April, based on the isohyet formats published by the SENMHI (2021) and INGEMMET (2006)).

7.3.3 Generation of rainfall data for past El Nino conditions

The daily rainfall disaggregation to process the 1KDHM input for representative strong ENSO events (1982-1983 and 1997-1998) begins referring the Isohyets produced by INGEMMET (2006). The isohyet information (total rainfall in mm for a complete rainy season) must be arranged into grid format (each grid covers a square area with 1km side, for a graphic depiction please refer to Figure 7-5). The available daily rainfall intensity patterns (in 1-hour intervals) at 4 locations were employed to generate the distributed rainfall intensity by interpolation to the nearest neighbor locations. The daily distribution must be scaled with an appropriate multiplication factor to reach a total rainy season estimate. Finally, the rainfall data in grid format is included in the HWRL Point2dist.exe and proceed generate the distributed rainfall file to run 1KDHM simulations.

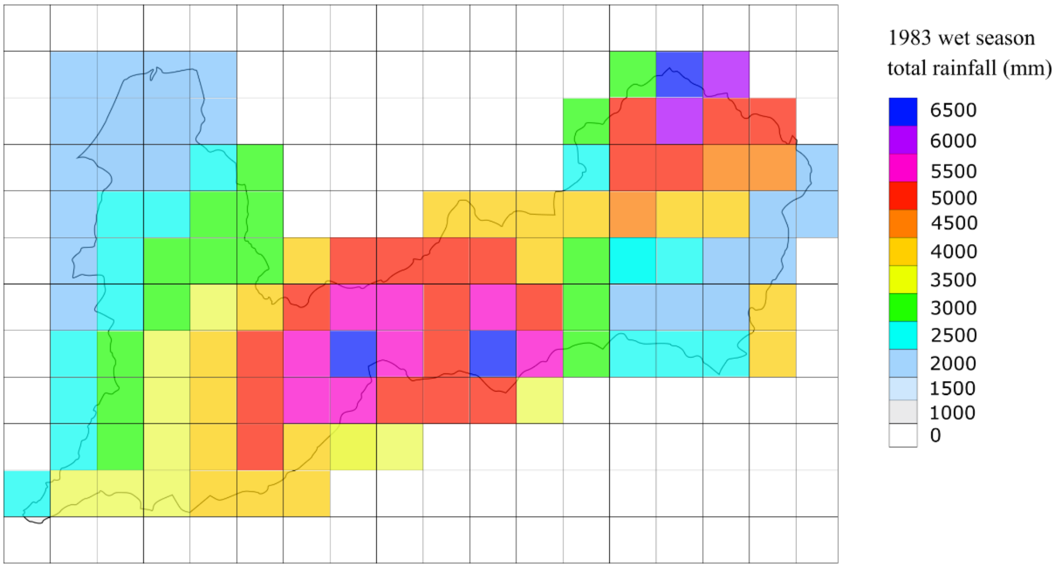

Figure 7-5 Total rainfall for year 1983, this is a schematic representation of the spatial distribution at 1 km resolution according to 1K-DHM point2dist.

The rainfall distribution depicted in **Figure 7-5** is an example of bias-corrected daily rainfall data derived from the original GSMAP database. It is possible to access and compare the accuracy of this distribution using the reports published by the meteorological agency (SENAMHI, 2021). The satellite rainfall distribution is a reliable method that can be used to include system anomalies.

After successfully generating data on the rainfall input, establishment of the rainfall-runoff parameters, and development of the sedimentation parameters based on the results for year-wise simulations are described in Chapter 6, confirming the effects of ENSO in the simulations. **Figure 7-6** is a summarized comparative illustration showing strong El Nino (SEN) for an average year (2012). The acceleration rate of sediment transport can be observed in the SEN years as compared to the conditions in 2012 in the simulation depicted in **Figure 7-7**. The fact that the sediment rating curves have been used to calibrate and verify the simulation of sediment transport warrants further consideration.

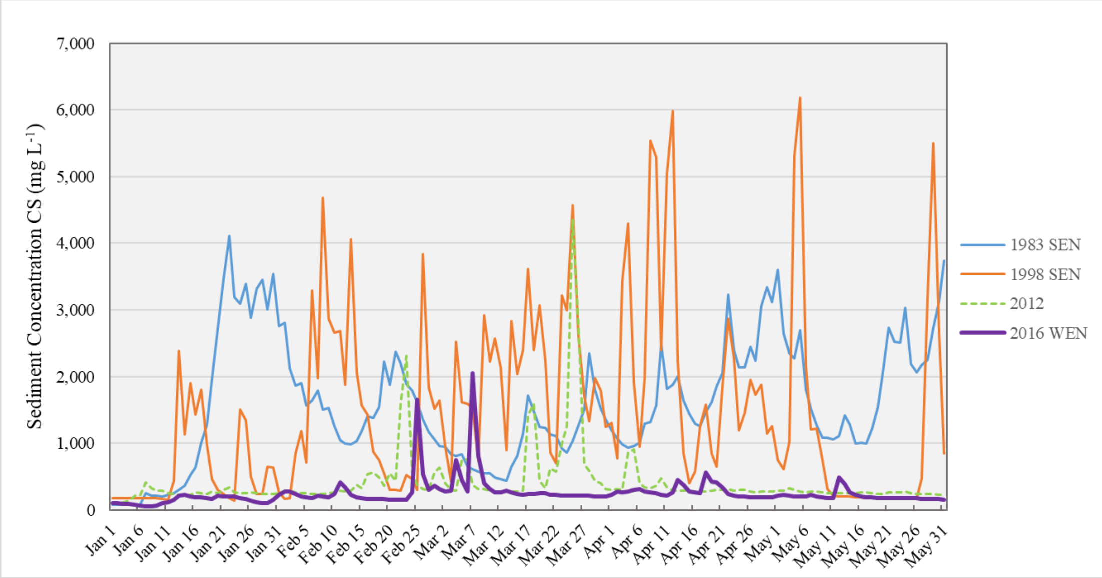

Figure 7-6 Daily average sediment concentration simulations for strong ENSO events (years 1983 and 1998), weak ENSO 2016, and 2012 defined as a regular year.

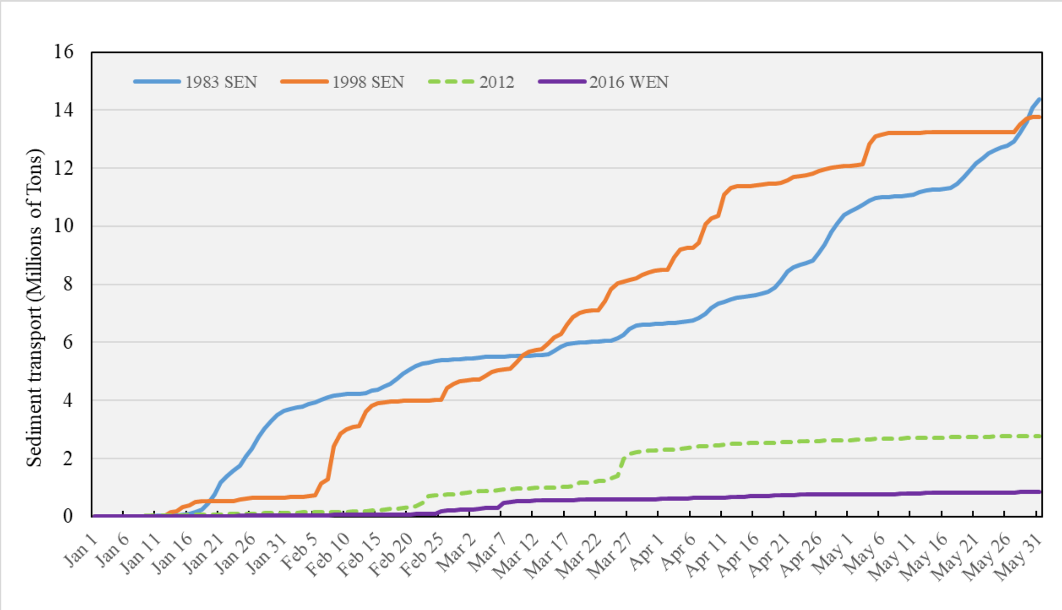

Figure 7-7 Cumulative sediment transport volume simulations (millions of tones after the outlet) for strong ENSO events (years 1983 and 1998), weak ENSO 2016, and 2012 defined as a regular year.

7.3.4 Sediment concentration maps according to ENSO events

The rainfall distribution affects the sediment concentration C_S (**Figure 7-8** to **Figure 7-11**) in channel sections, facilitates understanding of the sediment concentration in the slope section, and occurs predominantly as an instant response to rainfall intensity (the highest rainfall input). In the year 1983 (**Figure 7-8**), it could be inferred that the instant response to the highest rainfall peak occurred in 4-hour intervals. As depicted, the basin was affected by many two rainfall events occurring in a short interval and thus the channel section downstream featured a constant rate of sediment concentration downstream.

The highest rainfall peak in 1998 (**Figure 7-9**) is also appreciated. A markedly more considerable instant sediment concentration in response to the rainfall intensity is apparent.

Finally, the conclusion for the conditions prevailing in 2016 (**Figure 7-11**) is that lower rainfall intensities result in erosion and thus lead to the generation of high C_S; however, the concentration is reduced halfway to the outlet. This is an important explanation for the absence of the stationary system which prevents the sediments being flushed at the rate observed in the years 1983 and 1998. Finally, in reference to Figure 7-7, an appropriate summary that correlates the system rainfall anomaly with sediment transport rates can be proposed.

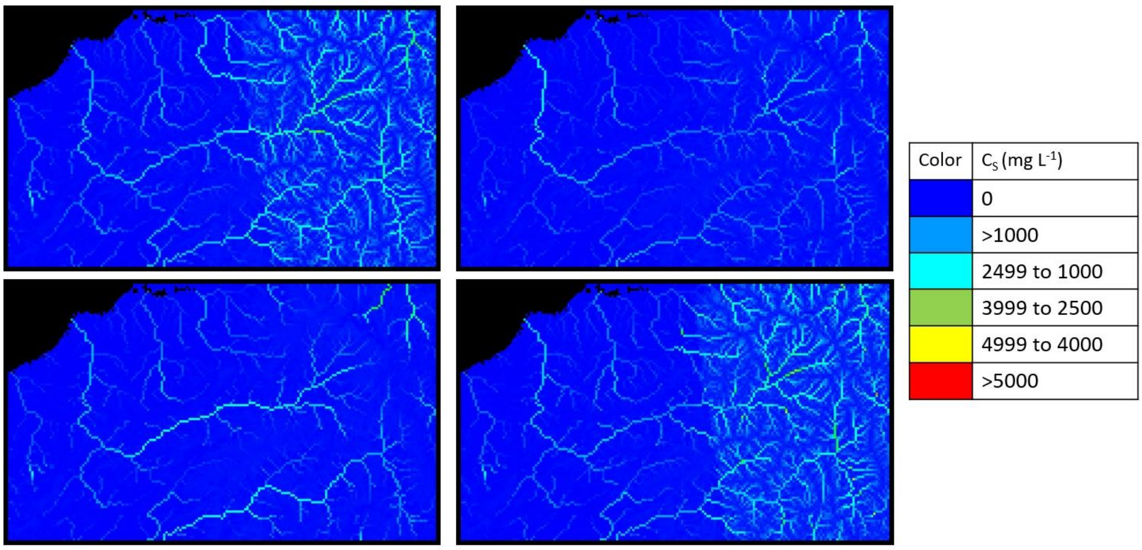

Figure 7-8 Year 1983 estimated sediment concentration (C_S) by 1KDHM simulation under the higher rainfall peak (1-hour intervals).

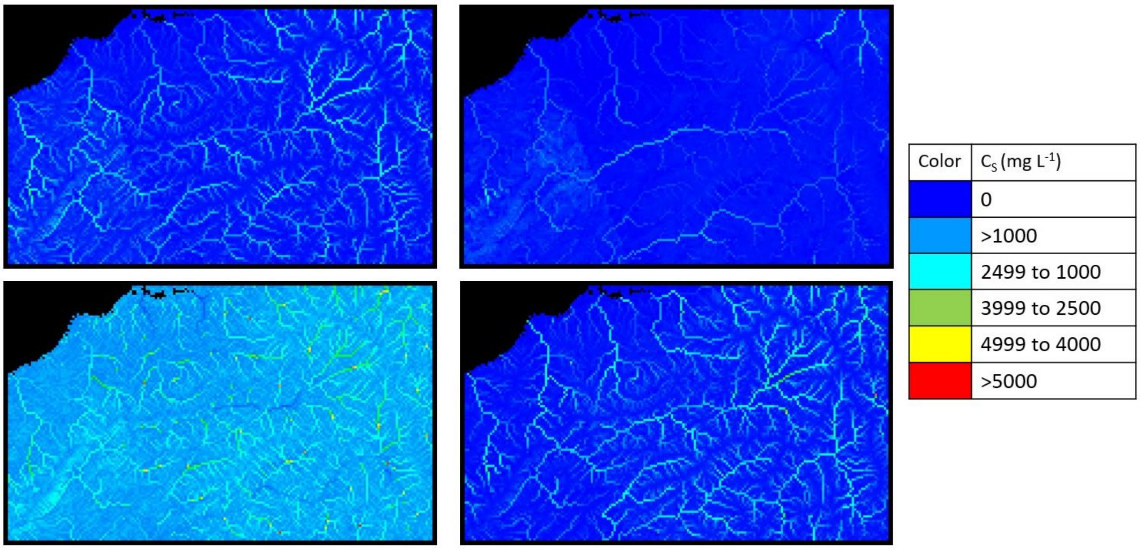

Figure 7-9 Year 1998, estimated sediment concentration (C_S) by 1KDHM simulation under the higher rainfall peak (1-hour intervals).

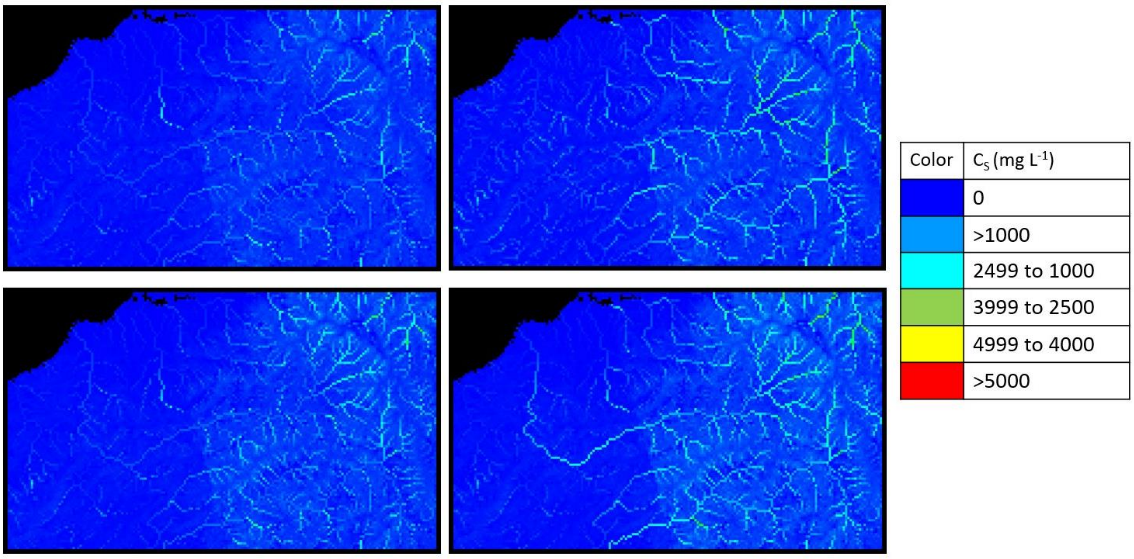

Figure 7-10 Year 2012, estimated sediment concentration (C_S) by 1KDHM simulation under the higher rainfall peak (1-hour intervals).

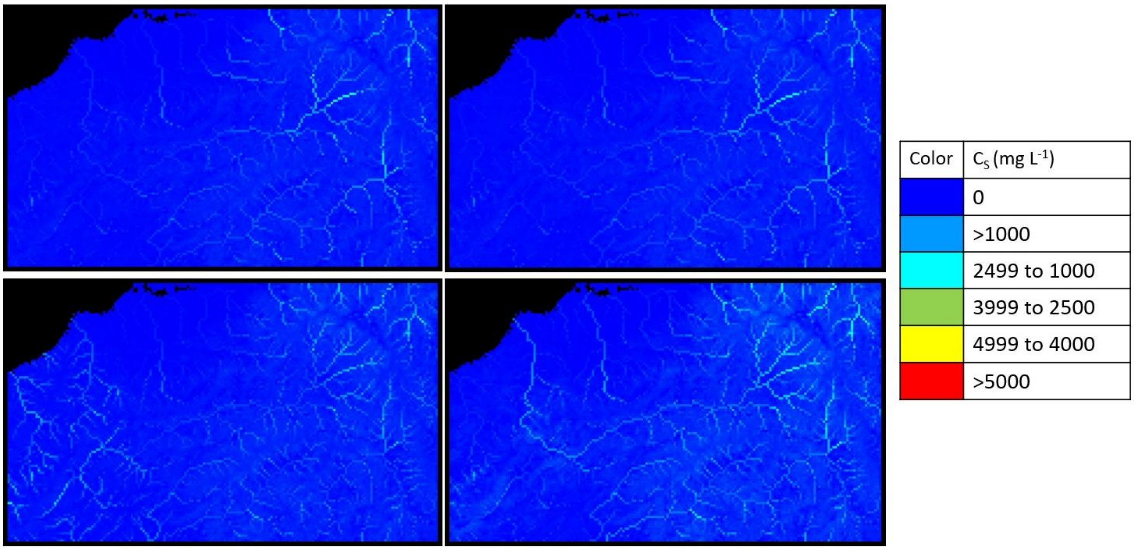

Figure 7-11 Year 2016, estimated sediment concentration (C_S) by 1KDHM simulation under the higher rainfall peak (1-hour intervals).

7.3.5 Sediment accumulation in the channel sections of the Tumbes River

Calculations of the sediment accumulation were performed by considering Exner Equations for the channel section. The method has been explained in Section 3.5c.

The change in the elevation of the riverbed is proportional to the rate at which sediment flows in every river channel cell according to the Exner relationships; **Figure 7-7** represents the total volume of sediment that is transported downstream; this sediment undergoes accretion in the river section following the outlet, as indicated by the recession in sediment flow. In this section, the final profile simulation after the rainy season completed in the selected years 1983, 1998, 2012, and 2016 are presented in **Figure 7-12** to **Figure 7-12**.

The sediment transport from upstream to the middle basin in case of a regular season (2012, **Figure 7-14**) and a weak ENSO event (2016, **Figure 7-15**) is evenly distributed throughout the channel. One interpretation is that the sediment that is subjected to erosion from the hillslope will be transported to the middle basin, while the channel discharge and the discharge persistence that results from kinematic energy is not sufficient to flush the sediments out after the outlet. The elevation results for 1983 and 1998 reveal major erosion and transport to the lower basin, with a profile accretion in the range of 2.5 to 3.5 m. Photographic evidence also confirms this scale of accretion.

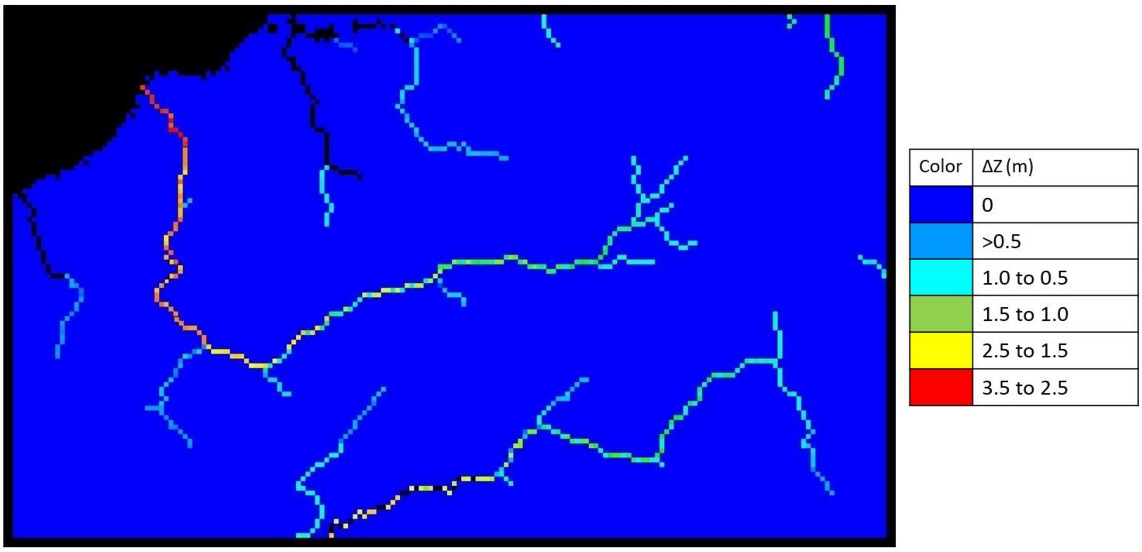

Figure 7-12 Year 1983, estimated sediment accumulation by 1KDHM in terms of bed elevation difference after the last day of the month of May.

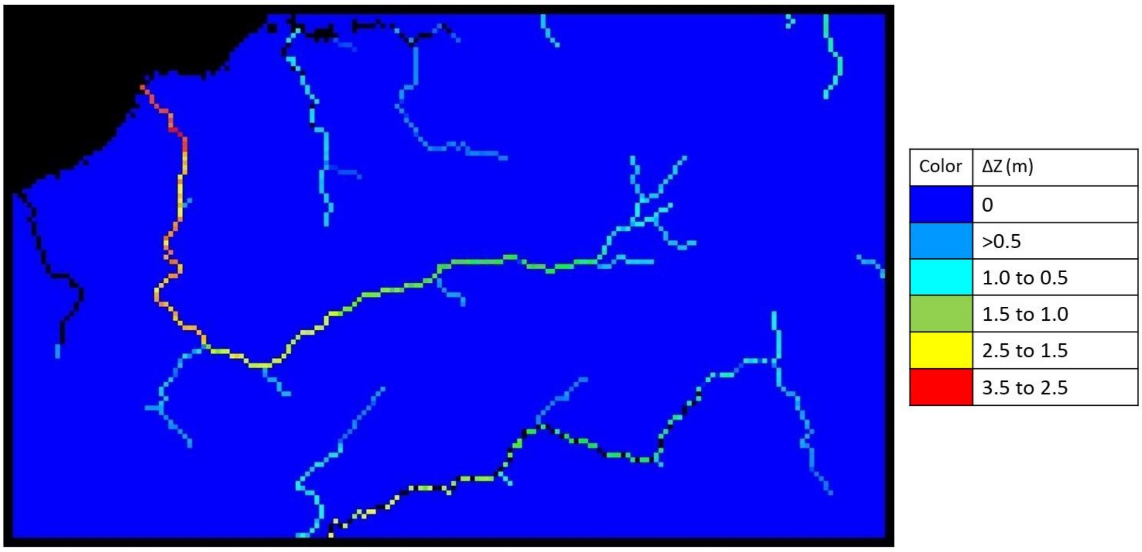

Figure 7-13 Year 1998, estimated sediment accumulation by 1KDHM in terms of bed elevation difference after the last day of the month of May

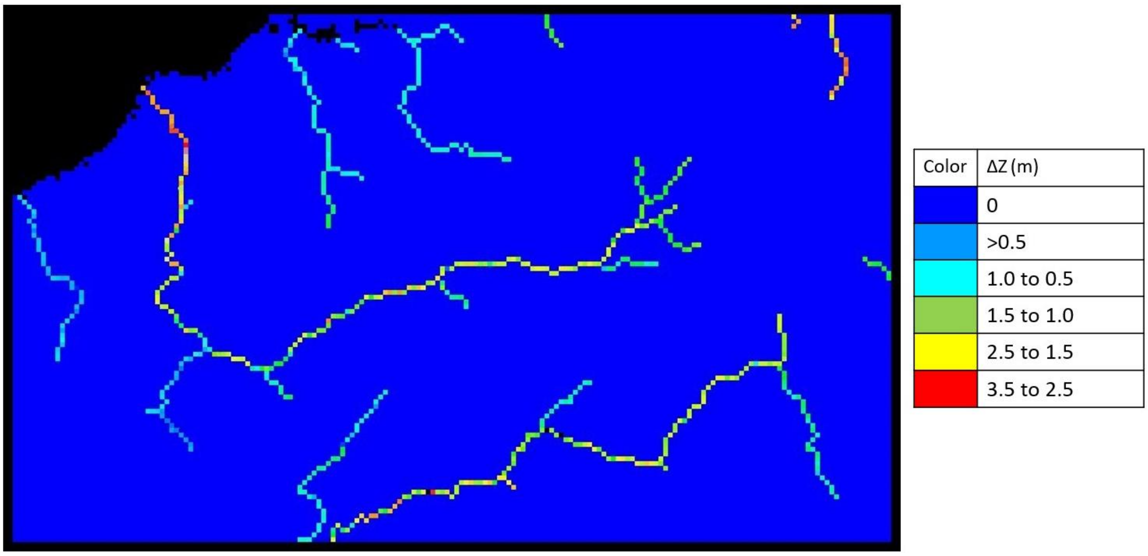

Figure 7-14 Year 2012, estimated sediment accumulation by 1KDHM in terms of bed elevation difference after the last day of the month of May.

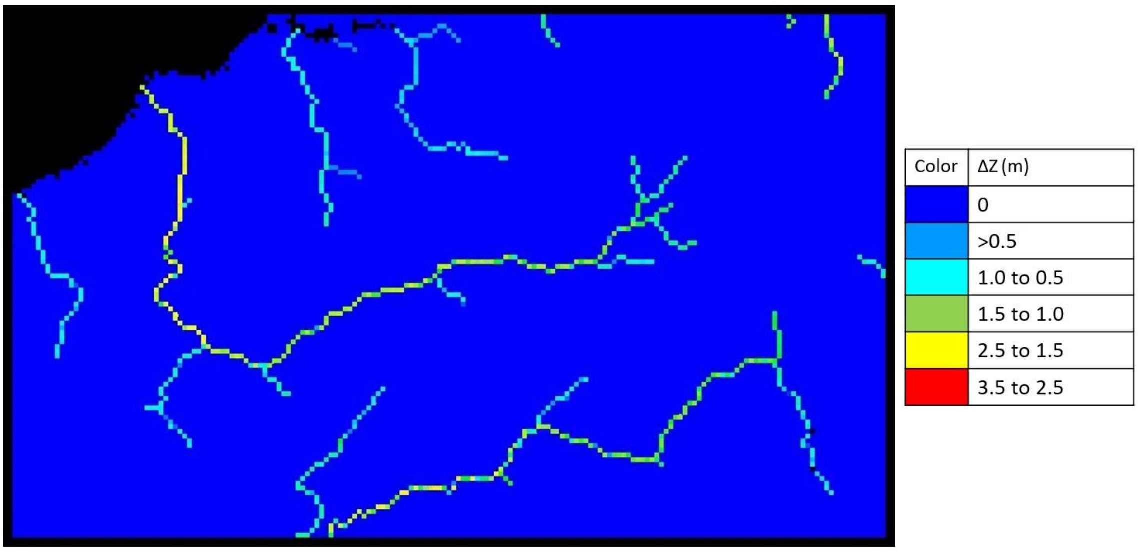

Figure 7-15 Year 2016, estimated sediment accumulation by 1KDHM in terms of bed elevation difference after the last day of the month of May.

7.4 Chapter conclusion

In Chapters 5 and 6, data collected from Peru and Ecuador were processed and compared to real hydrology processes and sediment transport. The accuracy of 1KDHM application was tested according to the reproduction of a hysteresis cycle and the sediment transport response. Additionally, in this chapter (Section 7.4.c), a graphical description has been put forth detailing the mechanism by which the sediment concentration C_S evolves in the direction of drainage and the manner in which this is featured in the model, enabling the obtainment of satisfactory simulations.

The main conclusion for this chapter is the possibility of testing the hypothesis considering appropriate rainfall distribution. The hydrological and soil appropriate parameters and the appropriate equations according to the slope or channel process could be used to reproduce the sediment rating curves. Finally, it is argued that a sequential approach to solving the sediment concentration under conditions of kinematic wave equation application can help provide acceptable results.

Chapter 8. Concluding remarks and future directions in the field

8.1 Concluding remarks

The development of a distributed sediment routing model for investigation of highly erosive basins was accomplished by combining rainfall-runoff processes with sediment generation and transport processes that suited the characteristics of the target basins.

The primary objectives of this dissertation were as follows:

- to develop an integrated rainfall-runoff and sediment routing model that could be used to simulate the dynamics of erosive basins;
- to understand and describe the sediment routing mechanics involved during ENSO events through the mathematical relationships;
- to reduce the prediction uncertainty by identifying the sensitive model parameters and the effects of extreme events in steep basins on sediment routing; and
- to generate sediment rating curves (the relationship between river flow rate and sediment concentration) applicable to forecast future ENSO events and to analyze the behavior during extreme floods.

The aforementioned objectives have been addressed in the following manner:

- By developing an appropriate model to evaluate basins with steep topography in terms of the one-dimensional limitations and considering the latest academic discussions.
- By analyzing the gauged data, by testing the theoretical assumptions, and by modeling the physical process to develop the mathematical relationships; a schematic representation of the modeling process was presented to understand the solution approach used.

- By conducting sensitivity analysis for a Japanese River using XRAIN input data and quality output data to track the relationships and to debug during the development stage of the model. The model was then applied to the selected basin in Peru, with examination of the seasonal trend anomalies and calibration of sediment model parameters. Sensitivity analysis was also performed in Peru to establish the regular season parameters that highlighted the best fit of results for Tumbes River.
- By performing regression analysis, by generating sediment accretion plots and sediment graphs, by performing assessments, and by providing conclusions consistent with the findings of previous reports and recent journal articles.

In **Chapter 2**, we have described the development of 1K-DHM and the new sediment transport component in the model. In the first stages of development, Kagetsu and Akatani River were considered for performing simulations to understand the limits of the model by using reference hydrographs.

In **Chapter 3,** the sediment model has been described based on the same time step and spatial division from the discharge solution by using the four-point scheme. The process is feasible and is functional in terms of computing memory space and processing capacity.

In **Chapter 4**, after application of the model and after conduction of a sensitivity analysis, it was determined that the sediment settling velocity should be prioritized. The results for the sediment transport balance were proven accurate given that 60,000 m^3 of sediments were deposited in the lower Akatani basin and an estimated 680,000 m^3 of sediment was subjected to erosion and flushed into the Chikugo River. This conclusion was deduced after performing the same sensitivity analysis to the Tumbes River basin described in Section 4.5.

In **Chapter 5**, following the application of two resolutions to the Tumbes River basin, it was found that particle diameter (d_{50}) and settling velocity (v_s) were the most sensitive parameters in reproducing sediment concentrations and yield outputs. These parameters must therefore be prioritized when applying a physically-based hydrological and sediment model.

In **Chapter 6**, it is concluded that the rating curves provide important insights to describe the relationship between sediment transport and discharge and to understand the manner in which rainfall intensity affects the sediment yield. For the years 1983 and 1998, during which strong ENSO events occurred, it could be interpreted that there was an instant increase in the production and transport of sediment as a result of the persistent rainfall and extreme precipitation recorded. The difference between ENSO and non-ENSO years was 10 to 100 times the average sediment transport rates.

In **Chapter 7**, the conclusion hints at the possible establishment of a model to achieve hypothesis testability considering appropriate rainfall distribution. The use of appropriate hydrological and appropriate parameters and appropriate equations according to the slope or channel process helped reproduce the sediment rating curves. Finally, it was argued that a sequential approach to solving the sediment concentration under conditions of kinematic wave equation application could be considered to obtain acceptable results.

For the specific analysis of the Peruvian Coast, it was confirmed that the application of erosion and sediment continuity relationships on a larger scale was possible. Throughout the literature review and results presented in Chapters 5 and 6, evidence was introduced regarding the manner in which a rating curve could help reproduce the effects of ENSO; the rating curves might be used in the development of a warning and river protection system, considering that the rainfall input forecast scenarios were representative in the short term; for example, 5 to 7 years could be considered an appropriate time window for investigation of the Tumbes River.

The presented thesis results support the hypothesis that the Peruvian Coast basin is subjected to a special weather system during ENSO events; hence, the first step in simulating such events is to consider the correct rainfall input, while the second step is to accurately describe the hydrological conditions existing on the hillslopes in the Andes Mountains before a hydrological model can be developed or adopted. Notably, the combination of these special conditions yields a clockwise or anticlockwise hysteresis relationship between the daily sediment transport and the daily average discharge.

8.2 Future lines of research

Extension for multi-annual sediment simulations include the simulation of considerable sand deposits. One improvement proposed is the inclusion of a cell-based storage function that may aid the release of sediments according to the velocity of the flow, and it will also be possible to activate this storage function in the scenario of landslides.

A mechanism to store sediment volumes over long periods of drought can also be included. Similar to multi-annual sediment simulations, it is possible to store sediments for longer drought periods, even spanning a full year; however, further assessment is warranted according to SENAMHI reports and journal articles on the specific basin. For example, sediment deposits that are recorded in the meandering sections of the lower basin may possibly consolidate and remain in the channel for periods as long as 18 months (in a return scenario of 100 years); however, owing to the existence of one-dimensional constraints, it is not possible to model this important process downstream.

The digital elevation model should be monitored and updated after every rainy season. After the occurrence of a major event, flood, or extreme sediment discharge, the riverbed features may change (from 1-m to 5-m resolution near Tumbes City). Thus, dredging or sediment removal is performed according to the degree of the event and the elevation near the outlet is considered to reset to 37.5 m a.s.l.

The proposal for flood risk assessment and a flood prevention system is a consequence of the forecasted river profile elevation change obtained by using hydrological models, which have been described in Section 6.3. It is feasible to include information on climate change, and forecasting of extreme events is feasible according to new tools such as GCM downscaling for rainfall, evapotranspiration, and updated DEM data obtained after certain simulation steps.

This thesis successfully presented the application of an approach to simulate sediment transport in one dimension. The possibility of the development of a 2D model that can be used to solve differential equations is a possibility that has been explored in the United States, Japan, Canada, and India. Based on the knowledge of kinematic wave equation and models that can be used by considering 2-dimensional relationships (i.e., RRI), the next step would include the implementation of soil detachment equations.

Bibliography

ANA. (2014). Tratamiento de cauce del Rio Tumbes para el control de inundacion y erosion fluvial (in Spanish). 58-71.

Arnold, J., Moriasi, D., Gassman, P., Abbaspour, K., White, M., Srinivasan, R., . . . Kannan, N. J. (2012). SWAT: Model Use, Calibration, and Validation. *Transactions of the ASABE*(55), 1491-1508. doi:10.13031/2013.42256

Barry, R. G. (2008). Regional Case Studies. In *Mountain Weather and Climate* (3rd ed., pp. 421-426). Cambridge University Press.

Bazo, J., de las Nieves, M., & Porfirio da Rocha, R. (2013). Relationship between Monthly Rainfall in NW Peru and Tropical Sea Surface Temperature. *Advances in Meteorology*(2013). doi:10.1155/2013/152875

Beven, K. (2012). Predicting Hydrographs Using Distributed Models. In *Rainfall-Runoff Modelling: The Primer* (2nd ed., pp. 181-183). Wiley.

Beven, K., & Freer, J. (2001). A dynamic TOPMODEL. *Hydrological Processes*(15), 1993-2011. doi:10.1002/hyp.252

Chero, L., & Tachikawa, Y. (2020). High-resolution distributed model to simulate erosion and sedimentation in a steep ba-sin: a case study of the Akatani River Basin, Kyushu, Japan. *Hydrological Research Letters, 14*(3), 97-103. doi:10.3178/hrl.14.97

Chero, L., Tachikawa, Y., Yorozu, K., & Ichikawa, Y. (2020). Analysis of DEM resolution dependence on a hydrological and sediment model for an ungauged basin in Peru. *Journal of Japan Society of Civil Engineers, 76*(2), I_1099-I_1104.

Dunne, T., & Aubry, B. (1986). Evaluation of Horton's Theory of sheetwash and rill erosion on the basis of field experiments. In A. D. Abrahams, *Hillslope processes* (pp. 31-53). New York.

Dunne, T., Malmon, D. V., & Mudd, S. M. (2010). A rain splash transport equation assimilating field and laboratory. *Journal of Geophysical Research: Earth Surface, 115*(F1). doi:https://doi.org/10.1029/2009JF001302

Egashira, S. (1998). Research related to Predicition of Sediment Yield and Runoff. *Symposium on Japan-Indonesia IDNDR Project*, (pp. 9-15). Bandung, Indonesia.

Egashira, S., & Matsuki, T. (2000). A method for predicting sediment runoff caused by erosion of stream channel bed. *Proceedings of Hydraulic Engineering*(44), 735-740. Retrieved In Japanese

Ferro, V., & Porto, P. (2000). Sediment Delivery Distributed (SEDD) Model. *Journal of Hydrologic Engineering, ASCE*(5), 411-422. doi:10.1061/(ASCE)1084-0699(2000)5:4(411)

Govers, G. (1990). Empirical relationships for the transport capacity of overland flow. *International Association of Hydrological Sciences*(189), 45-63.

Goyburo, A. (2017). *Monitoreo y caracterización del transporte de sedimentos durante crecidas o eventos extremos de El Niño en el río Tumbes.* Universidad Nacional Agraria La Molina, Lima, Perú.

Hajigholizadeh, M., Melesse, A., & Fuentes, H. (2018). Erosion and sediment transport modelling in shallow waters: A review on approaches, models and applications. *International Journal of Environmental Research and Public Health*(15), 518-520. doi:10.3390/ijerph15030518

Hapsari, D., Onishi, T., Imaizumi, F., Noda, K., & Senge, M. (2019). The use of sediment rating curve under its limtations to estimate the suspended load. *Reviews in Agracultural Science, 7*, 88-101. doi:10.7831/ras.7.0_88

Higgins, A., Restrepo, J., Ortiz, J., Pierini, J., & Otero, L. (2016). Suspended sediment transport in the Magdalena river (Colombia, south America): Hydrologic regime, rating Parameters and effective discharge variability. *International Journal of Sediment Research, 31*(1), 25-35. doi:http://dx.doi.org/10.1016/j.ijsrc.2015.04.003

INGEMMET. (2006). *Estudio geoambiental de la cuenca del río Puyango-Tumbes [Boletín_C-32]*. Retrieved from https://repositorio.ingemmet.gob.pe/handle/20.500.12544/264

Julien, P. (2018). River Mechanics. Cambridge, UK: Cambridge University Press. doi:10.1017/9781316107072

Kawaike, K., Yamada, Y., & Nakagawa, H. (2018). *Field survey and numerical simulation of flood and sediment inundation in Katsura river basin. 2017 Kyushu northern heavy rain disaster investigation report.* Kyoto: DPRI.

Kettner, A. J., Restrepo, J. D., & Syvitsky, J. P. (2010). A Spatial Simulation Experiment to Replicate Fluvial Sediment Fluxes within the Magdalena River Basin, Colombia. *The Journal of Geology, 118*(4), 363-379. doi:10.1086/652659

Khalil, A., Kwon, H.-H., Lall, U., Miranda, M., & Skees, J. (2007). El Nino-Southern Oscillation-based index insurance for floods: Statistical risk analyses and application to Peru. *Water Resources Research*(43), W10416. doi:10.1029/2006WR005281

Kirby, M. (1978). In M. Kirby, *Hillslope Hydrology.* Norwich, Great Britain: Wiley.

Kyoto University. (2021). *Tachikawa Laboratory 1KDHM research and Publication website*. Retrieved Apr 2021, from http://hywr.kuciv.kyoto-u.ac.jp/products/1K-DHM/1K-DHM.html

Laflen, J., Lane, L., & Foster, G. (1991). WEPP: a new generation of erosion prediction technology. *Journal of Soil and Water Conservation*(46), 34-38.

Lagos, P., Silva, Y., Nickl, E., & Mosquera, K. (2008). El Niño – related precipitation variability in Perú. *Advances in Geosciences*(14), 231-237. doi:10.5194/adgeo-14-231-2008

Lavado, W., Felipe, O., Silvestre, E., & Bourrel, L. (2013). ENSO impact on hydrology in Peru. *Advances in Geosciences, 33,* 33-39. doi:10.5194/adgeo-33-33-2013

Lavado, W., Ronchail, J., Labat, D., Espinoza, J., & Guyot, J. (2012). Basin-scale analysis of rainfall and runoff in Peru (1969–2004): Pacific, Titicaca and Amazonas drainages. *Hydrological Sciences Journal, 57*(4), 625-642. doi:10.1080/02626667.2012.672985

Lehner, B., Verdin, K., & Jarvis, A. (2006). *HydroSHEDS Technical Documentation.* Washington, DC, USA: World Wildlife Funds.

Lloyd, C., Freer, J., Johnes, P., & Collins, A. (2016). Using hysteresis analysis of high-resolution water quality monitoring data, including uncertainty, to infer controls on nutrient and sediment transfer in catchments. *Science of The Total Environment, 543*(A), 388-404. doi:10.1016/j.scitotenv.2015.11.028

MEF. (1999). Estudio hidrologico-meteorologico en la vertiente del pacifico del Peru con fines de evaluacion y pronostico del Fenomeno el Nino para prevencion y mitigacion de desastres (In Spanish)., (pp. 137-143).

Mirjam, A., Ros-Tonen, & van Boxel, J. (1999). *European Review of Latin American and Caribbean Studies, 67*, 5-20. Retrieved from http://www.jstor.org/stable/25675842

Morera, S. (2014). Erosión y transporte de sedimentos durante eventos El Niño a lo largo de los Andes Occidentales. *Generación de modelos climáticos para el pronóstico de la ocurrencia del Fenómeno El Niño, 1*(7).

Morera, S., Condom, T., Crave, A., Steer, P., & Guyot, P. (2017). The impact of extreme El Niño events on modern sediment transport along the western Peruvian Andes (1968-2012). *Scientific Reports, 7*. doi:10.1038/s41598-017-12220-x

Morgan, R., Quinton, J., Smith, R., Govers, G., Poesen, J., Auerswald, K., . . . Styczen, M. (1998). The European Soil Erosion Model (EUROSEM): a dynamic approach for predicting sediment transport from fields and small catchments. *Earth Surface Processes and Landforms, 23*(6), 527-544. doi:10.1002/(SICI)1096-9837(199806)23:6<527::AID-ESP868>3.0.CO;2-5

NOAA. (2021). *Pacific Marine Environmental Laboratory*. Retrieved from pmel.noaa.gov/elnino/what-is-el-nino

Nuñes, S., & Zegarra, J. (2006). Estudio Geoambiental de la Cuenca del Rio Puyango-Tumbes. *GEODINAMICA E INGENIERIA GEOLOGICA (In Spanish), 32*, pp. 61-64. Retrieved from https://hdl.handle.net/20.500.12544/264

Poesen, J., & Govers, G. (1986). A field-scale study of surface sealing and compaction on loam and sandy loam soils. Part II. Impact of souls surface sealing and compaction on water erosion processes. *Assessment of Soil and Surface Sealing and Crusting*, 183-193.

Quincho, J. B. (2015). *Estudio experimental del transporte de sedimentos en suspensión y fondo y comparación con fórmulas empíricas en los ríos Puyango-Tumbes y Zarumilla*. Universidad Nacional Agraria la Molina, Peru.

Renard, K. G., Foster, G. R., Weesies, G. A., McCool, D. K., & Yoder, D. C. (1997). Predicting Soil Erosion by Water: A guide to Conservation Planning with the Revised Soil Loss Equation (RUSLE). *Agriculture Handbook*(703), 1-183. Retrieved from https://www.ars.usda.gov/ARSUserFiles/64080530/RUSLE/AH_703.pdf

Roering, J., Kirchner, J., & Dietrich, W. (2001). Hillslope evolution by nonlinear, slope-dependent transport: Steady state morphology and equilibrium adjustment timescales. *Journal of Geophysical Research, 106*(B8), 16499-16513. doi:10.1029/2001JB000323

RSRTC. (2018). *River and Sabo Restoration Technology Review Comittee on the right bank of Chikugo River.* Ministry of Land, Infrastructure, Transport and Tourism - Kyushu Region Development Bureau. Retrieved from http://www.qsr.mlit.go.jp/site_files/file/bousai_joho/tecforce/H29hokubugouu_data/171122houkokusyo2.pdf

SENAMHI. (2021). Retrieved from Servicios del SENAMHI - Escenario de Lluvia: https://web2.senamhi.gob.pe/?p=escenarios-lluvia

Seong, C., Her, Y., & Benham, B. (2015). Automatic Calibration Tool for Hydrologic Simulation Program-FORTRAN Using a Shuffled Complex Evolution Algorithm. *Water, 7*, 503-527. doi:10.3390/w7020503

Syvitski, J., Morehead, M., Bahr, D., & Mulder, T. (2000). Estimating fluvial sediment transport: The rating parameters. *Water Resources Research, 36*(9), 2747-2760. doi:10.1029/2000WR900133

Takahashi, T., Inoue, M., Nakagawa, H., & Satofuka, Y. (2000). Prediction of sediment runoff from mountain watershed. *Proceedings of Hydraulic Engineering (In Japanese), 44*, 717-722.

Tanaka, T., & Tachikawa, Y. (2015). Testing the applicability of a kinematic wave-based distributed hydrological model in two climatically contrasting catchments. *Hydrological Sciences Journal*(60), 1361-1373. doi:10.1080/02626667.2014.967693

Torri, D., Sfalanga, M., & Del Sette, M. (1987). Splash detachment: Runoff depth and soil cohesion. *CATENA*(14), 149-155. doi:10.1016/S0341-8162(87)80013-9

Tote, C., Govers, G., Van Kerckhoven, S., Filiberto, I., Verstraeten, G., & Eerens, H. (2011). Effect of ENSO events on sediment production in a large coastal basin in northern Peru. *Earth Surface Processes and Landforms, 36*(13), 1776-1788. doi:10.1002/esp.2200

Wang, J., Yang, F., Qi, S., & Cheng, J. (2020). Estimating the Effect of Rain Splash on Soil Particle Transport by Using a Modified Model: Study on Short Hillslopes in Northern China. *Water, 12*(9), 2318. doi:https://doi.org/10.3390/w12092318

Wischmeier, W. H., & Smith, D. D. (1978). Predicting rainfall erosion losses-a guide to conservation planning. *Agriculture Handbook*(537). Retrieved from https://www.ars.usda.gov/ARSUserFiles/50201000/USLEDatabase/AH_537.pdf

WMO. (2017). Retrieved from https://public.wmo.int/en/media/news/heavy-rains-cause-landslides-flooding-colombia-and-peru

A) Appendix

Table A-1 2011-2012 gauging station recorded discharge (m^3 s^{-1})

YEAR	DAY	SEP	OCT	NOV	DEC	JAN	FEB	MAR	APR	MAY	JUN	JUL	AUG
2011 - 2012	1	21.319	16.842	16.020	18.366	55.358	294.732	940.121	280.853	327.230	92.924	55.490	36.853
2011 - 2012	2	20.519	17.010	15.768	17.373	63.268	453.651	793.868	259.861	288.174	92.924	54.851	36.853
2011 - 2012	3	20.519	17.667	15.360	18.748	98.674	524.088	695.498	250.378	279.211	92.367	53.361	36.136
2011 - 2012	4	20.848	18.954	15.181	18.265	113.936	379.570	502.228	262.116	194.397	89.369	52.249	35.146
2011 - 2012	5	19.926	23.513	15.450	17.815	133.054	291.783	421.728	1018.540	190.289	86.667	52.249	34.867
2011 - 2012	6	19.370	22.398	15.270	20.221	187.642	282.846	571.625	667.046	190.859	84.716	51.194	34.311
2011 - 2012	7	19.240	23.782	15.181	20.793	181.032	257.614	486.267	793.174	241.397	82.329	50.151	33.829
2011 - 2012	8	18.646	25.379	14.696	23.993	209.649	613.957	345.218	974.820	198.071	79.868	50.151	33.487
2011 - 2012	9	18.620	23.692	14.915	45.616	260.360	367.425	275.822	761.945	163.436	78.289	49.463	32.911
2011 - 2012	10	18.620	21.096	19.240	38.139	172.768	594.526	284.538	519.340	147.894	77.395	48.568	32.074
2011 - 2012	11	18.620	20.820	22.197	37.080	160.937	808.788	264.049	472.773	137.531	76.728	47.432	31.875
2011 - 2012	12	18.620	19.873	20.820	41.920	150.269	879.399	247.585	402.416	146.108	73.608	46.642	31.809
2011 - 2012	13	18.039	19.370	19.979	55.688	145.220	918.261	228.669	374.733	135.822	71.305	45.901	31.087
2011 - 2012	14	17.520	19.240	19.528	62.058	145.382	879.399	209.448	335.113	130.622	70.669	45.492	30.826
2011 - 2012	15	17.422	18.825	19.873	60.199	185.672	717.879	201.690	309.675	127.546	68.524	44.640	30.309
2011 - 2012	16	17.203	18.265	19.370	65.240	170.095	686.477	256.361	294.936	121.599	68.213	43.559	29.830
2011 - 2012	17	16.416	17.618	18.800	69.568	160.081	566.594	283.282	272.224	133.437	67.133	43.559	29.197
2011 - 2012	18	16.276	17.422	17.766	69.630	241.288	902.821	886.512	268.662	118.156	66.672	43.242	28.790
2011 - 2012	19	15.905	16.962	17.058	67.984	223.297	949.663	574.401	351.507	143.774	65.910	43.202	28.696
2011 - 2012	20	16.206	16.842	16.842	85.862	206.742	880.961	512.291	491.659	182.879	65.656	43.202	28.047
2011 - 2012	21	15.791	16.346	16.557	88.863	324.822	872.980	402.297	338.634	143.374	64.700	42.729	27.894
2011 - 2012	22	15.722	16.276	15.951	74.854	305.204	1028.602	858.927	357.331	131.001	63.851	41.947	27.316
2011 - 2012	23	15.722	16.276	15.450	67.622	290.511	1105.112	703.132	342.173	114.005	62.320	41.097	26.864
2011 - 2012	24	15.722	16.276	15.181	63.145	344.151	878.011	1339.326	286.915	107.376	61.149	40.181	26.596
2011 - 2012	25	15.722	15.836	14.849	60.590	516.027	939.427	1130.095	275.090	102.545	59.991	39.727	26.596
2011 - 2012	26	15.997	15.360	15.722	69.446	366.741	981.065	954.868	272.224	99.057	59.656	39.501	25.887
2011 - 2012	27	15.951	15.181	15.791	59.477	342.116	743.035	690.987	300.273	95.143	58.847	39.090	25.887
2011 - 2012	28	15.315	14.849	16.090	53.545	416.389	915.139	779.642	445.856	92.791	58.232	37.724	26.004
2011 - 2012	29	16.020	14.653	16.986	66.842	332.050	1176.615	604.415	451.624	89.630	56.968	37.724	28.078
2011 - 2012	30	16.842	14.653	17.716	59.256	371.706		402.297	289.225	87.303	55.490	37.943	26.745
2011 - 2012	31		14.653		55.953	312.973		317.286		82.301		37.687	25.945

Table A-2 2012-2013 gauging station recorded discharge (m^3 s^{-1})

YEAR	DAY	SEP	OCT	NOV	DEC	JAN	FEB	MAR	APR	MAY	JUN	JUL	AUG
2012 - 2013	1	23.592	18.223	18.653	29.384	46.350	92.021	171.939	213.956	75.344	88.547	39.886	25.778
2012 - 2013	2	23.951	18.223	19.126	27.477	45.121	103.699	159.555	194.496	73.912	92.519	39.565	25.170
2012 - 2013	3	23.571	18.074	19.585	26.357	41.766	105.913	161.656	235.296	72.381	79.742	38.335	25.049
2012 - 2013	4	23.445	17.779	19.585	25.195	41.188	101.297	141.839	181.780	71.739	74.150	38.335	25.049
2012 - 2013	5	23.257	17.779	19.585	24.720	40.371	132.922	135.767	168.709	69.265	70.985	38.335	24.720
2012 - 2013	6	22.676	18.559	21.113	24.036	38.532	159.887	131.216	183.439	68.019	67.626	37.399	24.334
2012 - 2013	7	22.449	21.394	29.314	23.445	36.517	266.809	198.255	181.780	69.435	65.572	37.399	23.893
2012 - 2013	8	22.449	18.223	29.198	23.445	35.572	307.389	234.965	169.175	70.985	65.352	36.860	23.631
2012 - 2013	9	22.408	18.223	30.682	23.049	33.188	292.904	173.156	156.128	65.627	65.352	37.554	23.631
2012 - 2013	10	21.959	17.926	29.478	22.945	31.772	256.747	146.526	140.594	65.352	62.965	36.631	22.941
2012 - 2013	11	21.959	17.413	24.978	22.945	32.298	316.013	127.428	138.387	65.352	60.059	35.872	22.941
2012 - 2013	12	22.285	17.341	27.184	22.593	32.546	428.132	172.713	149.162	66.900	58.921	34.864	21.683

2012 - 2013	13	21.959	17.504	29.994	27.477	37.284	334.810	172.824	159.998	68.358	56.786	34.679	21.354
2012 - 2013	14	21.736	17.413	24.741	31.473	44.428	334.921	402.922	139.179	66.788	55.340	34.202	20.949
2012 - 2013	15	21.474	17.250	23.761	28.434	43.657	351.506	539.698	124.858	65.572	54.406	32.759	20.841
2012 - 2013	16	21.293	17.214	24.441	25.828	42.307	260.507	391.422	116.713	112.191	52.662	31.702	20.521
2012 - 2013	17	20.994	17.377	26.735	24.313	47.554	236.844	291.245	109.743	99.074	50.393	31.250	20.099
2012 - 2013	18	20.994	18.353	28.182	23.656	64.369	234.080	362.895	108.683	98.009	49.420	30.803	19.942
2012 - 2013	19	20.342	19.278	25.065	23.090	58.613	222.912	309.379	131.641	86.112	48.141	30.428	19.708
2012 - 2013	20	20.108	19.643	24.057	22.945	54.064	212.298	259.954	141.483	80.053	46.927	30.428	19.553
2012 - 2013	21	20.049	19.050	23.761	26.870	51.899	176.252	256.084	118.299	80.678	46.350	29.753	19.068
2012 - 2013	22	20.049	18.503	23.445	31.449	51.662	158.007	220.038	158.450	79.183	45.295	29.253	18.740
2012 - 2013	23	19.604	18.223	24.355	31.812	55.340	189.409	197.260	116.004	77.340	45.295	28.595	18.466
2012 - 2013	24	19.585	17.596	24.591	30.231	178.844	152.589	213.514	103.772	75.764	44.817	28.042	18.466
2012 - 2013	25	19.585	18.747	23.951	29.082	217.178	140.062	275.323	96.881	73.557	43.700	28.042	18.891
2012 - 2013	26	19.336	19.069	27.251	41.435	208.529	175.699	220.259	92.997	72.850	42.223	28.042	19.068
2012 - 2013	27	19.126	17.816	34.432	68.810	169.410	262.939	324.527	92.655	68.867	41.229	27.274	18.967
2012 - 2013	28	19.126	17.761	28.989	54.161	142.823	201.683	479.879	87.621	66.788	40.331	27.274	18.466
2012 - 2013	29	18.936	16.925	29.478	43.700	128.264		346.531	81.117	67.123	39.725	26.738	17.948
2012 - 2013	30	18.672	16.907	29.900	38.690	111.576		278.308	77.951	67.626	39.285	25.839	17.416
2012 - 2013	31		16.907		40.007	98.150		241.709		72.850		25.778	17.297

Table A-3 2013-2014 gauging station recorded discharge ($m^3 s^{-1}$)

YEAR	DAY	SEP	OCT	NOV	DEC	JAN	FEB	MAR	APR	MAY	JUN	JUL	AUG
2013 - 2014	1	16.824	11.697	28.107	11.697	23.084	66.844	164.860	216.511	89.343	127.230	51.442	29.726
2013 - 2014	2	16.730	11.697	20.841	11.697	27.338	63.718	227.530	167.820	193.285	148.721	50.829	29.726
2013 - 2014	3	16.730	11.828	15.321	11.697	26.550	59.644	289.647	146.005	415.177	144.872	50.090	29.726
2013 - 2014	4	16.730	12.555	14.581	11.419	28.042	56.786	293.320	134.994	189.051	126.465	49.272	29.101
2013 - 2014	5	16.290	12.614	14.157	11.254	29.055	59.282	328.214	125.954	154.707	121.559	49.272	28.978
2013 - 2014	6	16.176	12.150	13.616	11.382	26.769	70.639	282.301	116.070	136.004	116.991	48.250	28.761
2013 - 2014	7	15.812	11.364	13.250	11.846	29.187	72.089	300.018	106.680	194.149	108.870	47.367	28.241
2013 - 2014	8	15.633	11.254	13.089	11.790	60.581	68.867	313.738	99.643	298.397	107.343	46.618	28.241
2013 - 2014	9	15.633	10.893	13.089	12.575	74.209	66.178	302.395	95.589	279.600	107.758	45.713	28.241
2013 - 2014	10	15.633	10.911	12.614	19.425	67.234	62.965	302.287	89.018	571.603	105.420	44.295	28.241
2013 - 2014	11	15.633	11.001	12.614	23.951	68.076	62.164	274.955	87.984	533.901	95.348	42.394	27.968
2013 - 2014	12	15.211	10.822	12.614	18.193	58.408	61.951	240.386	82.797	455.796	89.366	41.656	27.516
2013 - 2014	13	14.818	11.091	12.830	16.544	53.724	64.097	216.619	80.154	343.122	85.529	41.270	27.128
2013 - 2014	14	14.581	13.926	13.089	16.382	50.440	93.959	272.687	75.495	268.257	85.049	40.052	26.803
2013 - 2014	15	14.581	17.730	12.830	18.590	43.870	144.983	295.589	71.629	269.338	82.792	39.638	26.803
2013 - 2014	16	14.389	26.738	12.614	23.342	40.209	123.300	267.177	71.007	335.343	78.732	39.265	26.509
2013 - 2014	17	14.073	19.476	12.614	17.900	39.365	124.365	257.130	69.995	235.957	77.369	37.937	25.725
2013 - 2014	18	14.073	17.730	13.089	18.391	40.737	203.231	236.281	70.444	226.882	73.421	37.428	25.410
2013 - 2014	19	14.073	16.452	13.947	36.631	43.063	236.292	217.484	71.007	201.927	69.599	36.995	25.154
2013 - 2014	20	14.073	15.722	14.262	31.528	40.412	187.960	185.761	68.992	220.941	67.448	36.995	24.284
2013 - 2014	21	14.073	15.211	14.241	25.351	47.644	156.377	164.765	66.038	379.960	65.799	36.139	23.488
2013 - 2014	22	13.740	15.101	13.802	24.334	67.402	142.375	156.816	63.742	252.593	63.522	35.786	23.109
2013 - 2014	23	13.149	15.745	13.575	26.054	80.866	172.923	142.247	62.273	221.805	61.883	34.464	22.761
2013 - 2014	24	13.089	15.858	16.359	23.113	77.951	166.731	127.650	65.070	210.570	59.257	34.155	22.761
2013 - 2014	25	13.089	15.189	15.211	21.518	104.066	209.976	127.083	77.982	188.019	57.923	33.373	22.416
2013 - 2014	26	12.673	14.389	13.843	20.415	105.097	215.504	273.659	74.386	196.634	57.310	32.836	22.126
2013 - 2014	27	12.323	14.073	12.850	20.495	92.997	178.431	241.034	118.688	150.670	56.515	32.836	21.917
2013 - 2014	28	12.150	13.885	12.246	20.047	79.369	153.641	155.256	109.019	139.050	55.680	32.140	21.502
2013 - 2014	29	11.790	15.432	11.903	19.220	71.972		141.814	99.226	130.864	55.541	31.322	21.502
2013 - 2014	30	11.697	14.667	11.697	19.068	66.289		151.081	95.996	125.246	53.671	31.096	21.195
2013 - 2014	31		15.211		19.195	69.835		204.196		124.261		30.486	20.437

Table A-4 2014-2015 gauging station recorded discharge (m3 s^{-1})

YEAR	DAY	SEP	OCT	NOV	DEC	JAN	FEB	MAR	APR	MAY	JUN	JUL	AUG
2014 - 2015	1	20.090	14.651	13.444	13.628	35.540	93.490	128.270	758.206	301.144	126.588	53.260	37.932
2014 - 2015	2	19.478	14.445	13.859	13.546	31.187	81.554	135.581	670.141	205.998	114.459	52.600	37.321
2014 - 2015	3	18.854	14.445	13.859	13.284	28.832	73.250	181.622	467.103	184.368	105.752	52.600	36.574
2014 - 2015	4	18.453	13.940	13.618	12.886	25.729	65.220	160.567	380.325	223.508	102.722	52.162	36.010
2014 - 2015	5	18.406	13.840	13.336	13.526	25.334	60.262	151.583	505.985	203.423	97.894	51.553	34.900
2014 - 2015	6	17.689	13.840	13.640	14.354	23.446	59.705	160.005	402.470	164.469	132.128	50.518	33.978
2014 - 2015	7	17.439	13.569	14.485	17.192	21.188	S/D	237.909	320.456	147.086	195.826	50.134	33.305
2014 - 2015	8	20.719	13.253	14.805	31.360	20.231	287.739	161.549	275.394	138.979	114.668	48.948	33.172
2014 - 2015	9	20.041	15.068	13.401	21.952	19.557	282.545	128.270	246.425	132.888	100.516	48.487	33.506
2014 - 2015	10	19.945	15.763	13.596	24.913	19.608	227.521	116.620	234.194	125.261	96.001	48.153	33.675
2014 - 2015	11	19.723	24.199	17.709	27.107	19.608	257.139	107.701	212.821	120.397	92.159	47.490	32.939
2014 - 2015	12	19.191	23.695	17.890	22.369	19.327	186.254	100.448	201.105	115.436	86.157	47.078	32.377
2014 - 2015	13	19.191	22.611	21.774	21.188	18.998	144.845	103.813	183.466	110.190	83.304	48.445	32.311
2014 - 2015	14	19.347	19.440	22.762	21.000	18.897	127.040	135.581	411.096	111.763	79.887	47.821	31.593
2014 - 2015	15	19.945	17.273	21.189	18.203	19.737	127.980	207.589	345.820	132.432	78.600	45.734	31.109
2014 - 2015	16	19.660	16.276	21.189	15.743	23.361	129.265	188.078	775.588	123.069	76.336	44.731	30.821
2014 - 2015	17	19.037	16.081	20.415	15.125	24.224	119.872	218.819	923.006	299.985	73.467	44.057	30.060
2014 - 2015	18	18.457	16.081	15.788	15.499	149.337	115.867	268.087	690.870	215.783	71.820	43.623	30.060
2014 - 2015	19	18.457	15.577	14.040	21.161	94.276	115.320	578.017	468.004	135.952	70.455	42.998	29.590
2014 - 2015	20	18.638	15.387	13.587	24.913	138.669	117.790	692.416	471.223	121.332	69.002	42.416	29.310
2014 - 2015	21	18.216	14.943	13.104	25.790	95.553	109.676	585.316	499.419	113.072	68.334	41.763	29.310
2014 - 2015	22	18.791	17.121	12.730	25.913	168.146	100.196	506.991	686.493	109.647	65.500	41.763	28.878
2014 - 2015	23	18.730	16.227	13.064	25.425	161.409	94.943	382.346	417.920	105.818	63.273	41.191	29.465
2014 - 2015	24	23.304	14.966	13.064	24.290	124.742	144.144	501.938	336.936	125.041	61.525	40.851	29.777
2014 - 2015	25	18.883	14.530	13.304	23.910	110.938	155.092	744.351	297.410	107.018	58.302	40.624	29.310
2014 - 2015	26	20.041	17.657	13.792	21.514	126.967	129.580	923.038	272.433	108.699	58.022	39.950	28.663
2014 - 2015	27	16.789	17.324	14.651	21.514	132.212	120.711	741.544	253.120	156.135	58.022	39.913	28.572
2014 - 2015	28	15.709	15.577	14.544	20.362	269.491	128.343	1078.705	230.203	124.016	57.512	39.062	28.176
2014 - 2015	29	15.520	15.013	13.812	20.283	161.268		1159.696	211.534	122.996	55.452	38.695	27.336
2014 - 2015	30	15.068	14.372	13.730	72.763	126.175		767.231	203.938	232.778	53.837	38.185	26.862
2014 - 2015	31		13.552		45.708	106.916		956.586		142.760		38.185	25.815

Table A-5 2015-2016 gauging station recorded discharge (m^3 s^{-1})

YEAR	DAY	SEP	OCT	NOV	DEC	JAN	FEB	MAR	APR	MAY	JUN	JUL	AUG
2015 - 2016	1	25.729	16.474	16.840	22.077	13.723	71.239	312.548	275.289	150.655	60.058	39.400	27.061
2015 - 2016	2	23.524	16.254	19.591	18.587	14.696	65.432	515.313	462.683	153.295	70.356	39.400	26.366
2015 - 2016	3	23.524	17.044	16.210	17.209	15.274	65.668	738.841	367.881	138.881	67.284	37.818	25.909
2015 - 2016	4	23.378	17.996	14.835	16.493	16.398	84.318	654.091	414.067	127.456	64.886	37.284	25.569
2015 - 2016	5	22.879	17.469	14.176	16.231	19.802	112.008	771.363	498.151	122.760	62.203	36.023	25.569
2015 - 2016	6	22.259	16.766	13.284	15.620	38.707	87.576	793.293	309.984	118.169	62.928	35.300	25.966
2015 - 2016	7	21.480	16.825	13.093	15.341	66.636	82.335	476.857	243.136	115.424	58.932	35.300	26.137
2015 - 2016	8	21.188	16.313	13.093	15.481	63.128	73.458	378.653	185.761	122.035	56.856	35.300	25.569
2015 - 2016	9	21.188	16.269	12.962	15.027	72.294	82.099	477.917	167.699	190.451	56.265	35.300	25.344
2015 - 2016	10	21.188	16.781	12.742	14.765	77.991	124.085	322.400	172.110	147.475	55.183	34.788	24.898
2015 - 2016	11	21.018	17.469	12.742	20.350	85.640	90.126	273.351	459.921	128.870	54.647	34.484	24.319
2015 - 2016	12	20.616	18.215	12.581	16.004	100.779	77.850	351.745	362.025	116.335	57.958	34.484	24.237
2015 - 2016	13	20.263	19.942	12.391	15.603	105.652	72.561	351.745	285.233	110.729	54.647	34.248	23.965
2015 - 2016	14	19.971	22.532	12.098	14.940	102.474	67.415	261.274	264.903	104.827	51.797	33.679	23.587
2015 - 2016	15	19.424	19.342	12.040	19.320	82.902	63.590	196.173	252.196	99.055	50.046	33.679	23.293
2015 - 2016	16	18.876	15.215	12.040	23.351	71.570	60.379	175.689	411.636	94.405	48.955	33.281	22.475
2015 - 2016	17	18.852	16.459	12.625	18.901	68.217	61.607	159.082	364.567	91.400	47.960	32.886	22.319
2015 - 2016	18	18.742	17.264	15.742	17.104	80.683	63.779	150.327	307.774	87.208	47.263	32.886	21.957
2015 - 2016	19	18.560	16.942	15.449	16.807	75.819	59.152	162.668	247.445	82.790	46.694	32.886	21.701

2015 - 2016	20	18.560	14.308	14.071	17.523	86.632	54.477	150.573	186.413	81.310	46.008	32.461	21.471
2015 - 2016	21	18.560	15.464	15.874	16.476	89.182	56.366	134.699	166.912	84.633	45.050	31.493	21.093
2015 - 2016	22	18.450	15.918	15.596	16.301	82.335	60.899	117.179	156.382	78.067	44.615	31.143	21.093
2015 - 2016	23	18.268	15.698	15.259	15.638	77.614	73.836	109.236	175.689	74.849	44.104	30.574	21.471
2015 - 2016	24	18.268	15.903	18.464	15.795	68.265	173.452	105.025	240.153	72.766	43.441	29.826	21.093
2015 - 2016	25	18.268	17.571	23.893	15.760	64.346	249.833	99.886	165.362	71.765	42.401	29.548	20.495
2015 - 2016	26	18.268	18.815	30.786	15.219	67.320	300.577	94.467	153.046	70.252	42.248	28.998	19.981
2015 - 2016	27	18.255	15.552	27.801	14.922	61.749	204.598	91.400	317.608	67.689	41.868	29.059	19.908
2015 - 2016	28	17.975	15.654	26.440	15.586	57.027	247.291	114.239	238.164	64.787	40.701	29.089	19.908
2015 - 2016	29	17.793	15.069	24.957	14.608	62.882	162.541	244.794	170.868	62.928	39.664	28.967	19.498
2015 - 2016	30	17.416	14.849	24.992	13.632	68.359		134.469	160.698	60.958	38.789	28.363	19.331
2015 - 2016	31		14.601		13.541	79.172		114.935		62.396		27.796	19.331

Table A-6 List of gauging stations in study areas in Peru, operation by SENAMHI

Name	Type of data	Longitude	Latitude	Elevation ma.s.l.
El Tigre	Hydrological Meteorological	80°27'24.8'' W	3°46'7.32'' S	37
Rica Playa	Hydrological Meteorological	80°30'19.65'' W	3°48'42.84'' S	68
Cabo Inga	Meteorological	80°23'57.77'' W	3°58'43.44'' S	160

Table A-7 List of gauging stations in study areas in Peru, Ecuador, operation by INAMHI

Name (Code)	Type of data	Longitude	Latitude	Elevation ma.s.l.
Celica (M0148)	Meteorological	79° 57' 4'' W	4° 6' 16'' S	1,100
Zaruma (M0180)	Hydrological Meteorological	79° 36' 42'' W	3° 41' 51'' S	1,904

Table A-8 The soil parameters for Tumbes River basin in Chapter 5 were calibrated according to a range of characteristics extracted from test pits, we referred to those results to establish initial parameter values (Original source: (ANA, 2014), Table G6 and pp. 58-61)

Item	Location	Soil Mechanics Laboratory tests				Rock mechanics laboratory tests		
		Granulometric	SUCS classification	Atterberg Limits	Density (kg/cm^3)	Abrasion	Absorption	Specific weight
Test Pit 1	Huaquillas		SM-SC		1.86			
Test Pit 2	Romero Station		SM-SC		1.87			
Test Pit 3	La Noria		SP		1.79			
Test Pit 4	Cerro Blancoi		SP		1.75			
Test Pit 5	Malval Urcos		SM-SC		1.85			

Test Pit 6	Puente Franco		SM-SC		1.83			
Test Pit 7	El Oidor		SM-SC		1.65			
Test Pit 8	Prado Bajo		SM		1.89			
Test Pit 9	Rica Playa		GP		2.01			
Test Pit 10	El Sauce		SP		1.78			
Sampling	Las Animas		Not available		2.66			